

P.h.D. Thesis

Reconstruction and Modulation of Turbulent Thermal flows using Eulerian and Lagrangian Approaches

Submitted by -

Lokahith Narendra Agasthya

Matrikel Nr. 2016476

April 2022

Betrüer : Luca Biferale
Matthias Ehrhardt
Giannis Koutsou
Co-Betreuer: Andreas Bartel

Erstgutachter: Matthias Ehrhardt
Zweitgutachter: Andrea Mazzino
Drittgutachter: Prasad Perlekar



The PhD thesis can be quoted as follows:

urn:nbn:de:hbz:468-20220602-105126-0

[<http://nbn-resolving.de/urn/resolver.pl?urn=urn%3Anbn%3Ade%3A468-20220602-105126-0>]

DOI: 10.25926/wx9r-wg08

[<https://doi.org/10.25926/wx9r-wg08>]

Acknowledgments

This project has received funding from the European Union's Horizon 2020 research and innovation program under the Marie Skłodowska-Curie grant agreement No 765048.

I would like to thank my parents, Manasa Agasthya and Anantha Agasthya for their rock solid support and guidance and love throughout. My sisters Poshini and Greeshma and my brothers-in-law, Adarsh and Viveck who have been always by my side and given me support and advice whenever I needed it.

I am thankful to Prof. Luca Biferale, Dr. Patricio Clark Di Leoni and my colleagues at University of Rome "Tor Vergata" without whose efforts this thesis would not have been possible. Prof. Matthias Ehrhardt and Prof. Andreas Bartel at Wuppertal have also guided me and helped me along the way and this thesis is in no small part due to their contributions.

My friends in Rome, who made me feel like Italy is a second home country, thank you for the Italian lessons, the laughs and the companionship along the way. To Fabio, Francesca, Alfredo, Giovanni, Maddie, Dario, Guilhaerme. And also to my friend Davide, although he wasn't in Rome.

My Indian friends in Rome - Aishwarya, Ajay, Priyakshi. Every time I met you I felt slightly less homesick and less alone.

To my friends from across the Atlantic, thank you for keeping in touch. Naven, Mekhala, Khilav, Siddhartha, Shreyas, KP. Let's never stop the long phone calls.

To Bala, thanks for all the visits and the trips.

To Spandan, my forever willing travel companion. I explored Europe because of you. Let's meet in more and more cities again and again.

To Varun, may you always continue to inspire me.

To Sai Gowri, may we never run out of things we want to share with each other.

To Amma and Anna, once again. Everything I am, is because of you. I fly because you are the wind beneath my wings.

To tata! Your presence is missed everyday.

Shri Krishnarpanamastu!

Abstract

Thermally driven flows - fluid flows which are driven by temperature fluctuations - are abundant in nature and their dynamics, especially convection, plays an important role in several systems, including the atmosphere of the earth as well as other planets, oceans, the mantle and even several industrial processes. The best known and widely studied prototype thermal flow is the Rayleigh-Bénard convection. The precise nature of the correlation between the temperature and velocity fields that drives such flows is a subject of active research and is crucial to the understanding of thermal flows of all stripes. In particular, the question of whether when given a temperature field, the velocity field can be inferred and the methods to do so is of crucial importance to numerical weather prediction. In this thesis, multiple approaches to study this general theme are discussed. The method of data assimilation, which is a technique of enhancement of a numerical model using observational measurements is used to assimilate sparse temperature measurements of Rayleigh Bénard flows for varying degrees of turbulence. This proves successful in reconstructing Rayleigh-Bénard convection upto a moderate level of turbulence while for highly turbulent cases, it is found that the temperature field mainly sets the large-scale structure of the velocity field while the small-scale fluctuations are independent of the local temperature field. Thermally forcing particles in a flow system are considered to understand the small-scale as well as large-scale effects of local thermal forcing on the velocity field, with the choice of particle temperature completely left to the experimenter. The choice of a particle temperature that depends on the dynamics of the particle, with upward moving particles being hot and vice-versa, leads to either a quiescent, stable system, or a self-sustaining convective system with a sharp transition between the two. The system gives physical insight to the dynamics of convection and the non-trivial relationship between temperature fields and the injection of heat. Finally, the possibility of alternate approaches to study and recreate the correlation between the temperature and velocity fields via neural networks is discussed.

Contents

1	A Summary of the Doctoral Work	4
1.1	Outline	4
1.2	Fluids and Turbulence	5
1.3	Thermal flows	6
1.3.1	Rayleigh-Bénard Convection	6
1.4	Lattice-Boltzmann Method	8
1.5	Nudging applied to the Rayleigh-Bénard Convection	10
1.5.1	Data Assimilation and Nudging	10
1.5.2	Nudging the temperature field of Rayleigh-Bénard Convection	11
1.6	Particles in Turbulence	13
1.7	Physics-Informed Neural Networks	13
1.8	Activities during the doctoral programme	14
2	Fluid Dynamics and Turbulence	16
2.1	Introduction	16
2.2	Reynolds Number and Energy Dissipation	17
2.3	Vortex Break-up	21
2.4	Kolmogorov's 1941 Theory	24
2.5	Why Turbulence is hard to solve	27
3	Rayleigh-Bénard Convection	29
3.1	The Advection-Diffusion Equation	29
3.2	Thermal Flows	30
3.3	The Rayleigh-Bénard system	31
3.4	Nusselt Number	34
3.4.1	Exact Relations	35
3.5	Scaling in the Rayleigh-Bénard Convection	38

4	The Lattice Boltzmann Method	40
4.1	Introduction	40
4.2	Kinetic Theory	41
4.2.1	The Distribution Function	41
4.2.2	The equilibrium distribution	41
4.2.3	The Boltzmann equation	42
4.2.4	Discretisation of the Velocity	44
4.2.5	Discretisation of space and time	48
4.3	The Lattice Boltzmann Equation	49
4.3.1	Chapman-Enskog Analysis	50
4.3.2	The Lattice Boltzmann Algorithm	53
4.4	Forcing in Lattice Boltzmann	53
4.5	Two Population Lattice Boltzmann for Advected Scalar	54
5	Nudging applied to Turbulent Rayleigh-Bénard Convection	56
5.1	Introduction to Data Assimilation	56
5.2	The need for Data Assimilation	58
5.3	Nudging	58
5.4	Introduction to the study	60
5.5	Temperature-Velocity correlations in thermal flows	61
5.6	Partial Temperature Observations	62
5.7	Experimental set-up	62
5.8	Numerical Experiments	66
5.9	Error quantification	68
5.10	Results	70
5.10.1	Visualising the fields and errors	70
5.10.2	Global Errors	72
5.10.3	Scale-by-scale spectral properties and spectral errors	73
5.10.4	Inferring Nusselt Number	75
5.10.5	Varying Rayleigh Number	76
5.11	Lagrangian Nudging	78
5.12	Selection of the Parameters	79
5.13	Conclusions and Discussions	79
6	Study on Two-way thermally coupled Particles	82
6.1	Particles in Turbulence	82
6.2	Preferential Concentration	84
6.3	Non-isothermal Particles in Thermal Flows and Internal Heating	84
6.4	Study on virtual non-isothermal particles	85
6.5	Methods and Equations of Motion	86
6.5.1	Equations of Particle Motion	87

6.5.2	Particle Temperature Policy	88
6.5.3	Numerical Experiments	89
6.6	Results	90
6.6.1	Stable and Convective Configurations	90
6.6.2	Large-scale Circulation and Heat Transfer	94
6.6.3	Exact Relations	97
6.6.4	Comparison with Eulerian imposed thermal forcing	97
6.6.5	Anomalous behaviour for small T_+	99
6.6.6	Effects of varying α_0 and c	101
6.7	Conclusions and Discussion	102
7	Physics Informed Neural Networks	104
7.1	Introduction	104
7.2	Basics of Neural Networks	105
7.2.1	Training a neural network	106
7.3	Physics Informed Neural Networks	108
7.4	Applications of PINNs	109
8	Conclusions and Discussion	110

Chapter 1

A Summary of the Doctoral Work

1.1 Outline

This thesis contains an account of the work conducted by the author, Lokahith Narendra Agasthya, over the course of his doctoral work while jointly enrolled at the University of Rome “Tor Vergata” (UTOV), the University of Wuppertal (BUW) and The Cyprus Institute (CyI) starting from November 1st 2018. The work was jointly supervised by Prof. Luca Biferale, Prof. Matthias Ehrhardt and Prof. Giannis Koutsou with crucial inputs from and collaboration with Prof. Andreas Bartel, Prof. Federico Toschi and Dr. Patricio Clark Di Leoni. The PhD was a part of the STIMULATE European Joint-doctorate program (<http://www.stimulate-ejd.eu/>) under the Marie Skłodowska-Curie Actions program. All simulations were performed on the NEWTURB cluster at UTOV. Unless otherwise specified, all figures in the thesis are created by the author and data is based on the author’s own simulations.

The outline of the thesis is as follows. In the first chapter, a short summary of the main topics studied during the completion of the thesis work is provided, along with a brief description of the novel research conducted by the author. Other activities conducted during the doctorate are also mentioned, including workshops attended, conference presentations and research articles.

In the succeeding chapters, the topics are greatly expanded upon and explained in detail, in the author’s own words and to the best of his understanding. The novel investigation and research conducted is also described fully, with the results clearly specified along with the potential applications. The physical insights gained and the outlook for future investigations is also detailed. Finally, a concluding chapter is presented which brings together the various topics and ties them together to present an overall picture of the research conducted as part of the thesis work followed by a bibliography of the scientific literature consulted in preparing

the thesis.

1.2 Fluids and Turbulence

Fluid dynamics is the study of the macroscopic behaviour of gases and liquids, substances that flow. Most fluid flows are known to obey the Navier-Stokes equations, which for a fluid with fixed density ρ , having velocity field $\mathbf{u}(\mathbf{x}, t)$, is given by

$$\nabla \cdot \mathbf{u} = 0, \quad (1.1)$$

$$\frac{\partial \mathbf{u}}{\partial t} + (\mathbf{u} \cdot \nabla) \mathbf{u} = -\frac{\nabla p}{\rho} + \nu \nabla^2 \mathbf{u} \quad (1.2)$$

where p is the pressure of the fluid, and ν is the kinematic viscosity of the fluid, a measure of the internal resistance of the fluid to motion. The equations are subject to boundary conditions and initial conditions which determine the nature and geometry of the fluid domain.

Turbulence is a widely occurring feature in fluid flows. A fluid flow is generally considered turbulent when it shows some characteristics including but not limited to a high degree of chaoticity, large number of degrees of freedom, the presence of features at all scales and the phenomenon of vortex formation and break-up. *Laminar* flows are flows which lack turbulence and instead show regular flow patterns and highly predictable behaviour.

Turbulence is considered as one of the last unsolved problems of classical physics, not only because there exist very known few analytical solutions for even the simplest flows, but also because of the vast separation of scales, wherein turbulent flows show features at all scales which play an important role in the dynamics, thus making even numerical simulations of turbulence extremely expensive. The much celebrated 1941 theory of turbulence by Andrey Kolmogorov (K41 theory) is perhaps the most successful attempt at a universal description of the behaviour of turbulent flows. However, even K41 suffers from drawbacks and has shown to be invalid in experiments.

In Chapter 2, we start with a discussion on the Navier-Stokes equations and the dissipation of energy by viscosity. Following this, we discuss the phenomenology of Richardson to describe a turbulent flow, followed by a discussion of Kolmogorov's 1941 theory of turbulence and his universal similarity laws. Here we also introduce ways to characterise the small-scale structure of turbulence. Finally, we end with a short note on the difficulties of simulating turbulence and why it remains an open problem. The notes are taken mainly from the textbook by Davidson titled "Turbulence: An Introduction for Scientists and Engineers"

(see reference [1]) and the textbook by Frisch title “Turbulence: The legacy of A.N. Kolmogorov” (see reference [2]).

1.3 Thermal flows

The heating or cooling of a fluid causes the density of the fluid to vary and this subjects the fluid to buoyancy forces. Such non-isothermal fluid systems are particularly interesting as it is perhaps the most widely found and studied case of the transport of an *active scalar* in fluids which modify the underlying fluid flow in which they are being transported. Such feedback is often highly non-linear and complex leading to several phenomenon such as wind, convection, chaos, pattern formation and fully developed turbulence in the underlying fluid.

Fluid flows driven by temperature variations, known as thermal flows, are studied in various forms, very often via idealised model systems. Thermally driven flows are usually studied under the *Boussinesq approximation* [3], where the density fluctuations of the fluid are considered small enough that the fluid can still be represented by the incompressible Navier-Stokes equation. For a fluid with density ρ_0 at temperature T_0 , the density ρ at temperature T where $|T - T_0|$ is small is given by

$$\rho(T) = \rho_0\beta(T_0 - T) \quad (1.3)$$

where β is defined as the thermal expansion coefficient of the fluid at T_0 . β is assumed constant for small variations in temperature. The full equations, known as the Oberbeck-Boussinesq equations, are

$$\nabla \cdot \mathbf{u} = 0, \quad (1.4)$$

$$\frac{\partial \mathbf{u}}{\partial t} + (\mathbf{u} \cdot \nabla) \mathbf{u} = -\frac{\nabla p}{\rho_0} + \nu \nabla^2 \mathbf{u} - \beta(T - T_0) \mathbf{g}, \quad (1.5)$$

$$\frac{\partial T}{\partial t} + \mathbf{u} \cdot \nabla T = \kappa \nabla^2 T \quad (1.6)$$

where \mathbf{g} is the acceleration due to gravity and κ is the thermal diffusivity of the fluid.

1.3.1 Rayleigh-Bénard Convection

A widely studied thermal fluid system is the Rayleigh-Bénard system where a layer of fluid is kept between two plates maintained at a constant temperature, with the bottom plate having a higher temperature than the top plate. For a small

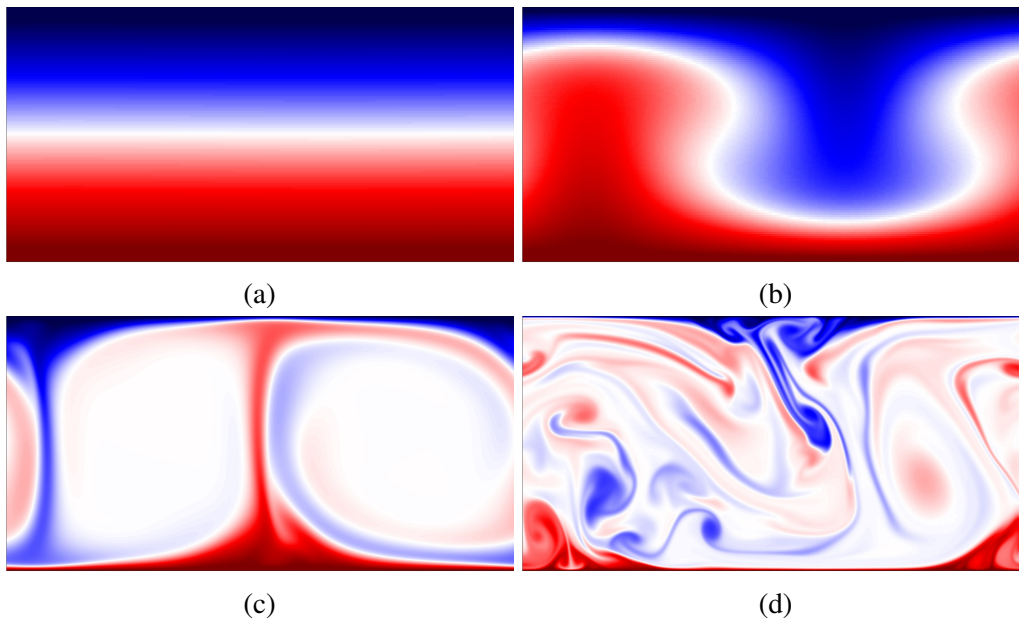


Figure 1.1: Visualisations of the temperature field of four different Rayleigh-Bénard Convection flows showing the transition from a purely conductive state with $Ra < Ra_c$ and $\mathbf{u} = 0$ everywhere in (a) to a highly turbulent state in (d) with $Ra \sim 10^8$ with an abundance of fine-scale structures and vortices. (b) visualises a flow with $Ra \gtrsim Ra_c$ which shows a convective, laminar flow. (c) visualises a flow with $Ra \sim 10^6$, which is well in the convective regime with the first signs of smaller scale structure but still not turbulent. Shown is the normalised temperature field with maximum of 1 (red) and minimum of -1 (blue).

difference in temperature ΔT between the two plates, the fluid remains at rest. On increasing ΔT beyond a threshold value however, the fluid is set into motion, first in the form of convective rolls with two, four or more convective rolls, and eventually, to more and more chaotic forms until it reaches a state of fully developed turbulence.

This phenomenon was first observed by Bénard in his experiments of 1900 [4]. Lord Rayleigh in his foundational paper [5] was the first to provide a theoretical understanding of the instability and showed that the non-dimensional number deciding the stability is the Rayleigh number Ra given by

$$Ra = \frac{g\beta\Delta T}{\nu\kappa} L_z^3 \quad (1.7)$$

where $\Delta T = T_d - T_u$ is the temperature difference maintained between the top and bottom walls and L_z is the vertical height of the domain. The Rayleigh-Bénard instability occurs when for a flow, $Ra > Ra_c$ where Ra_c is the critical Rayleigh number with a theoretical value of $Ra_c = 1708$ [6].

An important response parameter of the Rayleigh-Bénard convective system is the widely studied Nusselt number Nu given by

$$Nu(z) = \frac{\langle vT - \kappa\partial_z T \rangle_{A,t}}{\frac{\kappa\Delta T}{L_z}}, \quad (1.8)$$

where $\langle \cdot \rangle_{A,t}$ indicates the time and spatial averages at a given height z and v is the vertical component of the velocity. In Chapter 3, we introduce again and discuss the advection-diffusion equation and the heat equations in the Boussinesq approximation. Following this, we introduce in full detail the Rayleigh-Bénard system, the onset of convection on increasing Ra and the transition to turbulence, along with the various flow features observed. We also state the known exact relations which establish the fundamental importance of the Nusselt number in studying the dynamics of the system and explore in more detail the form of the instability caused by the inverted temperature configuration. The notes are taken mainly from the textbook on Hydrodynamic and Hydromagnetic Stability by Chandrashekar, the textbook on the same subject by P.G. Drazin and lastly, the monograph on Rayleigh-Bénard Convection by Emily S.C. Ching. (see References [6, 7, 8] respectively).

1.4 Lattice-Boltzmann Method

The Lattice-Boltzmann method is a mesoscale method to solve for the equations of fluid dynamics. The method is simple, easy to implement even for non-trivial geometries and highly parallelisable, leading to its recent popularity. In

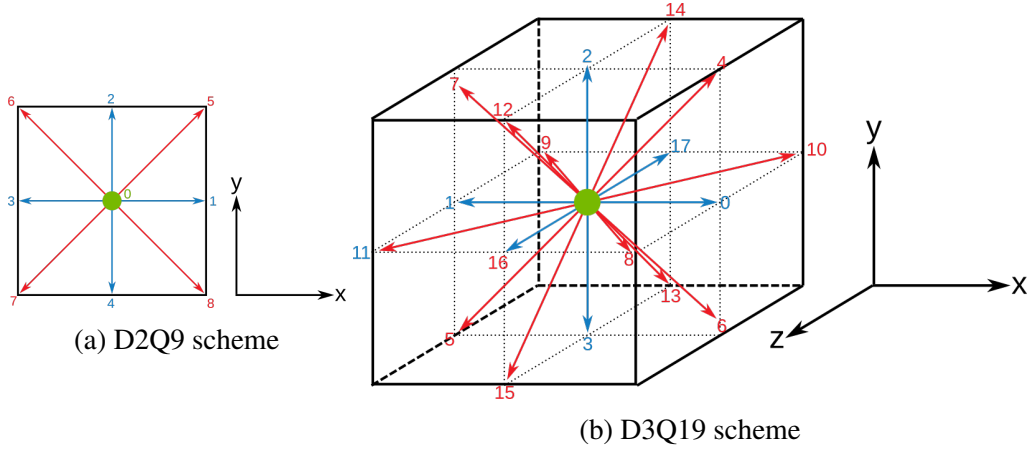


Figure 1.2: Lattice vectors for the D2Q9 and D3Q19 Lattice Boltzmann schemes. Image taken from [9] with permission of the author.

the Lattice Boltzmann method, the fluid flow is idealised as a set of populations $f_i, i = 0, 1, \dots, k$ defined at each grid point with associated Lattice vectors c_i

$$f_i(\mathbf{x} + \mathbf{c}_i \Delta t, t + \Delta t) = f_i(\mathbf{x}, t) + \frac{f_i(\mathbf{x}, t) - f_i^{\text{eq}}(\mathbf{x}, t)}{\tau_f} \Delta t, \quad (1.9)$$

where the second term on the right is the BGK collision operator with f_i^{eq} being an equilibrium population distribution and τ_f is a relaxation time that is set by the viscosity of the fluid. There exist various schemes with varying lattice vectors c_i and number of lattice vectors k for solving different kinds of fluid problems. They are generally referred to by $DnQk$, where n is the number of spatial dimensions and k is the number of Lattice vectors. For 2D and 3D fluid flows respectively, D2Q9 and D3Q27 are among the most widely used schemes. The fluid hydrodynamic quantities at each point in space and time are obtained from the various moments of the populations as

$$\rho = \sum_i f_i; \quad (1.10)$$

$$\mathbf{u} = \frac{1}{\rho} \sum_i f_i \mathbf{c}_i; \quad (1.11)$$

The specific details of setting the equilibrium population and obtaining the hydrodynamic quantities depend on the choice of Lattice-Boltzmann scheme and other considerations such as the presence of a bulk-forcing.

In Chapter 4, the basic theoretical details underlying the Lattice Boltzmann equation as well as the method of discretising it in space and time is discussed.

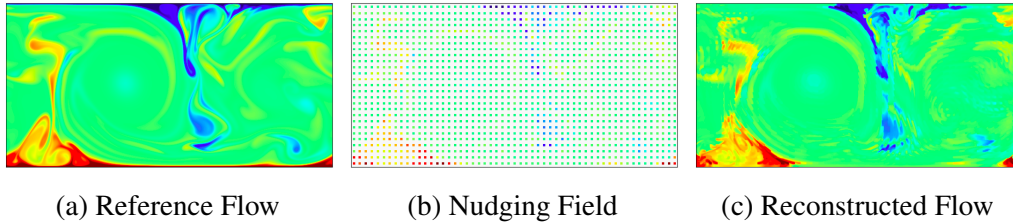


Figure 1.3: A schematic overview of nudging applied to the temperature field of Rayleigh-Bénard convection. The reference flow is a Rayleigh-Bénard convection system, from which are extracted point-wise data from temperature probes placed on a regular array. These point-wise data are then expanded to cover a small finite square to construct the nudging field T_n . T_n is only defined in the immediate vicinity of the probes. Using T_n , a new reconstructed system is nudged according to equation (??) to give a reconstructed flow.

The modification of the Lattice Boltzmann equation to incorporate body forces is also described. Further, the use of a second set of populations to simulate the diffusion of a scalar by the fluid is also detailed, including the addition of a scalar source-term and the handling of scalar boundary conditions. Finally, the specific advantages of the Lattice Boltzmann algorithm and the high degree of parallelisability are discussed, along with a few drawbacks. The foundational textbook by Krüger et. al. [10] is the main reference for this chapter.

1.5 Nudging applied to the Rayleigh-Bénard Convection

1.5.1 Data Assimilation and Nudging

Data Assimilation is a family of techniques to combine computational models along with observational data to produce an optimal *analysis*, that is, a prediction for the state of a complex system whose equations are known [11]. The main idea is to leverage as much available knowledge of the system as possible. Given accurate observational data and realistic numerical models, the use of both together should provide a superior estimate compared to the use of either method individually. Data Assimilation techniques are widely used in the study of the atmosphere and weather modelling. (see [12] and references within).

While there exist several known methods of data assimilation, in this study we use the simple technique of *nudging* [13, 14], where a *nudging term* proportional to the difference between the observational data and the obtained dynamical model output is added to the evolution equation.

1.5.2 Nudging the temperature field of Rayleigh-Bénard Convection

As introduced above, nudging is a data assimilation technique to incorporate observational data into numerical models. In this thesis, I describe a study to assess the technique of nudging applied solely to the temperature field of the Rayleigh-Bénard convection, ie., assuming availability of data on the temperature field only. The study was conducted at the University of Rome “Tor Vergata” in collaboration with Dr. Patricio Clark Di Leoni (currently at Universidad de Buenos Aires, Argentina) and Prof. Luca Biferale. Details of the study have been published under the title “Reconstructing Rayleigh-Bénard flows out of temperature-only measurements using nudging” [15].

Understanding the reconstruction of the velocity field from the temperature field serves to lend deeper physical insight into the role played by the temperature field in setting the dynamics of the Rayleigh-Bénard convection. Does the temperature field alone determine the velocity field at every point? Or does it only set some statistical quantities of the velocity field, the velocity field at a certain scale? These are fundamental questions that are answered in this study.

It is assumed that sparse spatial measurements of the temperature field at fixed intervals of time are available. These temperature measurements are interpolated and modified according to a given protocol to construct a temperature T_n , or the nudging temperature field.

In Chapter 5, we start by defining data assimilation more precisely and providing a brief overview of the basic terminology and equations of data assimilation. The nudging method is described in more detail, placing it in the context of a wider family of data assimilation techniques. The notes are taken mainly from the book “Data Assimilation - Making sense of Observations” edited by Lahoz et. al (Reference [16]) and the ECMWF lecture notes by Bouttier and Courtier (Reference [17]).

Following this brief introduction, the study applying nudging to the Rayleigh-Bénard convection is presented in complete detail in Chapter 5 with the specific results regarding the spatial as well as scale-by-scale reconstruction of the temperature and velocity fields, along with discussion on the accuracy of the method with varying Rayleigh number. The chapter is concluded with a discussion on the main findings of the study, the physical insight provided by it and lastly, ways to improve or build upon the study for future work is suggested.

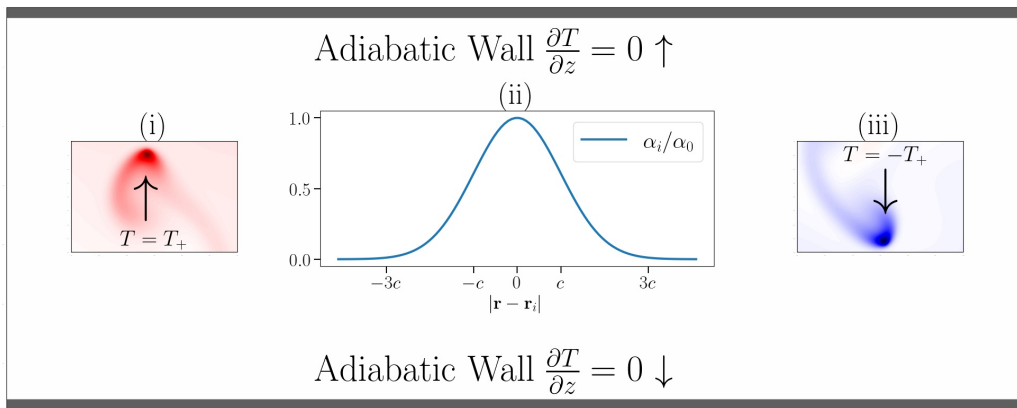


Figure 1.4: An overview of the study with virtual non-isothermal particles reported in this thesis. Upward moving particles with positive velocity are set to a positive temperature T_+ while downward moving particles are set to a negative temperature $-T_+$. The top and bottom walls of the 2D domain are adiabatic while the lateral walls are periodic. The heat injection into the fluid is directly proportional to the temperature difference between the particle and the fluid and also proportional to the coupling strength α_i which has a value α_0 at the particle location and falls off as a Gaussian with increasing distance $|\mathbf{r} - \mathbf{r}_i|$ from the particles.

1.6 Particles in Turbulence

Turbulence, as we have already seen, is a multi-scale, chaotic problem that is extremely hard to parametrize and requiring extensive computational resources to solve. When the fluid acts as a carrier for particles suspended in the fluid, it leads to several interesting phenomenon. The most significant of these is preferential concentration, or the tendency of heavy particles suspended in a turbulent fluid flow to exclusively sample the regions of the flow characterised by low vorticity or the stretching regions [18, 19]. Preferential concentration occurs due to the ejection of particles from vortical regions. Particle collisions are also enhanced due to preferential concentration and ejection from vortices, which plays an important role in initiation of warm rain in clouds [20] and in the formation of planets [21].

Particles with a temperature different from the local fluid temperature induce temperature fluctuations in the fluids. These interactions are highly non-linear and show complex dynamics [22]. In this thesis, we consider a 2D fluid domain with adiabatic top and bottom walls and periodic lateral boundaries. In this fluid, thermally interacting particles are introduced that absorb or release heat in their immediate vicinity. The particles are idealised to have infinite heat capacity and a temperature that depends on their vertical motion. An overview of this system is shown in Figure 1.4. The system thus initialised shows several interesting characteristics, with a sharp transition from a quiescent, stable flow to turbulent thermal convection.

In Chapter 6, an introduction and overview of the dynamics of particles in turbulent flows is provided. Following this, the study on thermally interacting particles introduced above is described in detail, including the results regarding the stationary end-state, the characteristics of the flows and its dependence on various input parameters. The study was conducted at the University of Rome “Tor Vergata”, Italy (UTOV) and the Bergische Universität Wuppertal, Germany (BUW) in collaboration with Prof. Luca Biferale (UTOV), Prof. Andreas Bartel, Prof. Matthias Ehrhardt and Prof. Federico Toschi (Eindhoven University of Technology) and the results are in an as yet unpublished manuscript titled “Lagrangian instabilities in turbulent convection with stable temperature profiles” which is to be submitted to a peer-reviewed scientific journal soon.

1.7 Physics-Informed Neural Networks

Neural networks, inspired by biological neurons, are a system consisting of nodes, weights and biases along with activation functions and other components [23]. Neural networks are used to train systems using *training data* and the training is

tested on *validation data*. Neural networks are a function that takes as input, the independent variables of the system and produce as output the dependent variables while the training fine-tunes the function by adjusting the weights and biases. Neural networks have emerged as a field of active research in the past decade and are being used to replace several traditional computational methods [24].

Physics-Informed Neural Networks (Or PINNs) have recently been introduced [25] as a data-driven method to solve partial differential equations such as the Navier-Stokes equations using neural networks. The method has even proved successful [26] in reconstructing flows where information on one or more state-variables is completely absent, such as reconstructing the velocity and pressure of a thermal flow given only temperature data. In PINNs, in addition to the use of training data to train a system, the system is also constrained to be consistent with the model equations of the system as an additional input. In Chapter 7, an introduction to neural networks is provided along with an introduction to and application and working of Physics Informed Neural Networks.

1.8 Activities during the doctoral programme

Scientific Publications

- **Lokahith Agasthya**, Luca Biferale, Andreas Bartel, Matthias Ehrhardt, and Federico Toschi, “Lagrangian instabilities in turbulent convection with stable temperature profiles”, *Manuscript in Preparation*
- **Lokahith Agasthya**, Patricio Clark Di Leoni and, Luca Biferale, “Reconstructing Rayleigh-Bénard flows out of temperature-only measurements using nudging”, *Physics of Fluids* 34 (1) (2022) 015128, arxiv:2201.02306

Conference Presentations

- **Lokahith Agasthya**, Patricio Clark Di Leoni and, Luca Biferale, “Data Assimilation of Rayleigh-Bénard Convection using solely thermal measurements”, *Bulletin of the American Physical Society* (2021)
- **Lokahith Agasthya**, Luca Biferale, Andreas Bartel, Matthias Ehrhardt, and Federico Toschi, “Modulation of Rayleigh-Benard Convection by Lagrangian Thermal Forcing.”, *Bulletin of the American Physical Society* (2020)
- **Lokahith Agasthya**, Patricio Clark Di Leoni and, Luca Biferale, “Lattice Boltzmann based Lagrangian Nudging in Rayleigh-Benard Convection”, *29th International Conference on Discrete Simulation of Fluid Dynamics* (2020)

Coursework Completed

- Frontiers and Methodologies in Computational Science, Spring 2021 semester, The Cyprus Institute
- Fundamentals of Data Science and Statistics, Fall 2020 semester, The Cyprus Institute

Workshops Completed

- School on **Machine and Reinforcement Learning, Rare Events and Tensor Networks** at the University of Rome “Tor Vergata” - Held Online (Sep 2020)
- Workshop on **Multiscale, multilevel algorithms and uncertainty quantification** at the University of Wuppertal (Jun - July 2019).
- School on **Mathematical Modeling and Numerical Analysis for Exascale** at the Humboldt University of Berlin (Apr 2019).
- School on **Fundamentals of Data Science** at the University of Ferrara (Feb 2019).
- Workshop on **High performance computing and simulation** at Forschungszentrum Jülich (Nov - Dec 2018).

Chapter 2

Fluid Dynamics and Turbulence

Summary The reader is introduced briefly to fluid flows and a brief qualitative description of laminar flows as well as turbulent flows. The incompressible Navier-Stokes equations are introduced in their dimensional as well as dimensionless form, the latter of which leads naturally to the definition of the important Reynolds number. The expression for the rate of dissipation of mechanical energy into heat via viscosity is derived from the Navier-Stokes equations. Following this, the phenomenology of turbulent flows as a *cascade* of energy from the larger-scales to smaller-scales via vortex break-up, also known as the Richardson energy cascade is described, and this in turn leads to a discussion of Kolmogorov's 1941 theory of turbulence (K41) and the two hypotheses of the universal similarity of turbulent flows which were proposed by him. The Kolmogorov microscales are derived, various measures to quantify the small-scale structure of a flow are defined and the specific expressions for the small-scale velocity increments in highly turbulent flows are derived for a K41 scenario. The drawbacks and experimental refutations of Kolmogorov's theory are briefly discussed and finally the chapter ends with a discussion on the intractability of the Navier-Stokes equations and turbulent flows.

2.1 Introduction

Fluid dynamics is the study of all objects that flow. However, different fluids flow differently, with some fluids showing a greater propensity to be set into motion while other fluids show a greater tendency to resist flow. For example, most gases and liquids such as oils and lubricants flow easily while thick liquids such as honey or syrups flow sluggishly. This difference is quantified by *viscosity*, which measures the resistance offered by the fluid to motion. This resistance is analogous to a frictional force between two layers of fluid moving relative to each other.

Viscosity causes the mechanical energy of the fluid motion to be dissipated in the form of heat.

Fluids with a high viscosity as well as fluids flowing with a very slow velocity generally show *laminar* flow, a state of flow which is smooth and regular. In a laminar flow, the fluid velocity at a point in space \boldsymbol{x} remains unchanged. Thus, parcels of fluids (or tracers, such as a dye injected into the fluid) follow identical, predictable trajectories from a given starting point at all times. Further, two parcels of fluid starting from two nearby points at the same time follow very similar trajectories to each other. Some examples of such a flow are specially designed water fountains, water slowly flowing from a partially open tap or the rise of smoke immediately above the source of the smoke. However, laminar flows are generally rare in nature.

In contrast, in fluids with a low viscosity or fluids flowing at high velocity, the flow ceases to be smooth and regular. The fluid velocity at a fixed point in space \boldsymbol{x} is a rapidly fluctuating function of time. Two parcels of fluid starting at the same point in space but at different times show widely different trajectories from each other. Similarly, parcels of fluid even infinitesimally close to each other at a given time separate rapidly and follow vastly different trajectories. The consequence of these properties is that turbulent flows are extremely sensitive to their initial configuration. If two identical turbulent systems are considered at a given time with initial configuration that varies infinitesimally, the realised state of the system deviates rapidly. Nearly all fluid flows found in various settings and nearly all natural settings are turbulent in nature. The best known examples of turbulent flows are the air flow in clouds, airflow over aircraft wings, solar flares. The atmosphere of all planets are turbulent, with the Giant Red Spot of Jupiter being a spectacular example of a turbulent vortex. They are all characterised by high chaoticity and are very hard to predict.

A popular story goes that the great physicist Werner Heisenberg once said that if he had the chance to ask God two questions, he would ask “Why quantum mechanics?” and “Why turbulence?”. And he was quite sure that God would be able to answer the first question [27]. While the origin of the story is uncertain, it is most certain that turbulence has befuddled scientists and philosophers alike for over a hundred years. Considered to be one of the last unsolved problems in classical physics, the phenomenon of turbulence is ubiquitous in nature - in fact the absence of turbulence, or laminarity, is very much the exception.

2.2 Reynolds Number and Energy Dissipation

While we have already seen a short description of some characteristics of a turbulent flow, we still haven't introduced a quantitative measure for understanding

when a flow remains laminar and when it can turn turbulent. We start with the incompressible Navier-Stokes equation, where the fluid velocity $\mathbf{u}(\mathbf{x}, t)$ follows

$$\nabla \cdot \mathbf{u} = 0, \quad (2.1)$$

$$\frac{\partial \mathbf{u}}{\partial t} + (\mathbf{u} \cdot \nabla) \mathbf{u} = -\frac{\nabla p}{\rho} + \nu \nabla^2 \mathbf{u}. \quad (2.2)$$

The derivation of the Navier-Stokes equation is well-known and can easily be looked up from any introductory text on fluid dynamics, such as Davidson's textbook. It involves applying Newton's Second law of Motion on a small parcel of fluid and considering the conservation of mass and momentum. To recap, $p(\mathbf{x}, t)$ is the fluid pressure, ρ is the fixed density of the fluid and ν is the kinematic viscosity of the fluid. Equation (2.1) imposes the conservation of mass while Equation (2.2) imposes the conservation of momentum. The operator $\frac{\partial}{\partial t} + (\mathbf{u} \cdot \nabla)$ is often written simply as $\frac{D}{Dt}$ and is known as the convectational derivative or the material derivative.

The behaviour of a fluid is consistent with the Navier-Stokes equations within the *continuum approximation*, wherein it is assumed that the various properties of the fluid such as density, pressure, velocity etc. are smooth and continuous functions in space, even for an infinitesimal fluid element. This approximation ignores the discrete, molecular nature of the fluid and is valid when the characteristic length scale of the fluid system is much larger compared to the inter-molecular distance between the fluid molecules or the molecular mean free path. The continuum assumption breaks down when considering fluid flows with length scale comparable to nano-scales ($\sim 10^{-9}$ m), rarefied gas flows, etc. where either the length scale of the fluid system is small or the inter-molecular distance is large, hence the system is in the regime of molecular dynamics rather than continuum mechanics.

The Navier-Stokes equations are valid for *Newtonian fluids* where the viscous stresses τ_{ij} are given by

$$\tau_{ij} = 2\rho\nu S_{ij}, \quad (2.3)$$

where

$$S_{ij} = \frac{1}{2} \left[\frac{\partial u_i}{\partial x_j} + \frac{\partial u_j}{\partial x_i} \right]. \quad (2.4)$$

The viscous stresses are defined so that the net viscous force F_i acting in the direction i per unit volume is given by

$$F_i = \frac{\partial \tau_{ij}}{\partial x_j}, \quad (2.5)$$

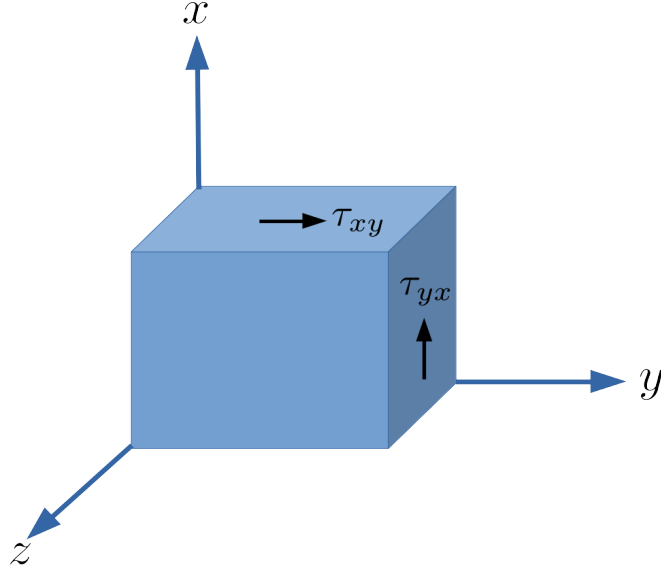


Figure 2.1: Stress Tensors.

and the Navier-Stokes equations can also be written as

$$\nabla \cdot \mathbf{u} = 0, \quad (2.6)$$

$$\rho \frac{D\mathbf{u}}{Dt} = -\nabla p + \frac{\partial \tau_{ij}}{\partial x_j}. \quad (2.7)$$

They are accompanied by appropriate boundary conditions and initial conditions and are perfectly deterministic, even if the solutions thereof are highly chaotic and possess large degrees of freedom.

Consider a typical length scale L and a velocity scale U of a fluid system under consideration. The fluid can be described in terms of a dimensionless velocity \mathbf{u}^* , non-dimensional length \mathbf{x}^* , non-dimensional pressure p^* and non-dimensional time t^* such that

$$\mathbf{u}^* = \mathbf{u}/U, \quad \mathbf{x}^* = \mathbf{x}/L, \quad t^* = t/(L/U), \quad p^* = p/(\rho U^2).$$

It can be easily verified that non-dimensionalising equation (2.2) leads to

$$\frac{\partial \mathbf{u}^*}{\partial t^*} + (\mathbf{u}^* \cdot \nabla^*) \mathbf{u}^* = -\nabla^* p^* + \frac{\nu}{UL} (\nabla^*)^2 \mathbf{u}^*. \quad (2.8)$$

where $\partial/\partial t^*$ and ∇^* are the non-dimensional time derivative and gradient respectively. The single non-dimensional parameter then that determines the system is the ratio $\nu/(UL)$, which is the inverse of the very important dimensionless number for turbulent flows, the Reynolds number, given by

$$\text{Re} = \frac{UL}{\nu}. \quad (2.9)$$

where ν as we have already seen is the kinematic viscosity of the fluid. Re is the ratio of the inertial forces to the viscous forces acting on the fluid. The greater the length scale of the system, the faster the characteristic flow velocity of the fluid or the less viscous the fluid, the more turbulent the fluid flow. At larger Re, it is the inertial forces that dominates the fluid while at lower Re, viscous dissipation is most significant.

The most suitable choice for L and U is not always immediately apparent, but it is well established for certain widely studied systems such as flow in a cylindrical pipe, where L is simply the diameter of the pipe. There exists a threshold Reynolds number Re_c below which a given system is laminar, while for greater Re, the system is unstable to infinitesimal perturbations and turns turbulent. In the experiments of Reynolds considering the flow of a fluid in a channel with an inlet at one end, he rightly concluded that the flow turns turbulent due to small perturbations at the inlet of the fluid [28]. For $\text{Re} > \text{Re}_c$, the flow is increasingly sensitive to disturbances at the inlet while for $\text{Re} < \text{Re}_c$, the flow is always laminar.

A turbulent fluid dissipates mechanical energy in the form of heat due to viscosity, which is described by the viscous term $\nu \nabla^2 \mathbf{u}$. To understand the amount of energy dissipated by the viscous forces acting on the fluid, we simply multiply equation (2.2) with \mathbf{u} and use $\nabla \cdot \mathbf{u} = 0$ giving

$$\frac{D}{Dt} \left(\frac{|\mathbf{u}|^2}{2} \right) = -\nabla \cdot \left[\frac{p}{\rho} \mathbf{u} \right] + \nu \mathbf{u} \cdot (\nabla^2 \mathbf{u}) \quad (2.10)$$

Simplifying the final term on the right as

$$\nu \mathbf{u} \cdot (\nabla^2 \mathbf{u}) = u_i \frac{\partial}{\partial x_j} [\tau_{ij}/\rho] = \frac{\partial}{\partial x_j} [u_i \tau_{ij}/\rho] - 2\nu S_{ij} S_{ij}, \quad (2.11)$$

we get

$$\frac{\partial(u^2/2)}{\partial t} = -\nabla \cdot [(|\mathbf{u}|^2/2)\mathbf{u}] - \nabla \cdot [(p/\rho)\mathbf{u}] + \frac{\partial}{\partial x_j} [u_i \tau_{ij}/\rho] - 2\nu S_{ij} S_{ij}. \quad (2.12)$$

Considering a small volume dV and integrating the above equation over this volume, the various terms are interpreted in the following way - the term on the

left hand side represents the rate of change of kinetic energy in the volume of fluid. The first, second and third terms on the right hand side respectively represent the rate of transport of kinetic energy across the boundary by convection, the rate of work done by the pressure forces on the boundary and the rate of work done by the viscous forces on the boundary. The final term $-2\nu S_{ij}S_{ij}$ thus represents the internal loss of mechanical energy in the form of heat due to viscosity. Thus, the rate of dissipation of energy by viscosity per unit volume ϵ is given by simply

$$\epsilon = 2\nu S_{ij}S_{ij}, \quad (2.13)$$

or explicitly,

$$\epsilon = \frac{1}{2}\nu \sum_{i,j} \left[\frac{\partial u_i}{\partial x_j} + \frac{\partial u_j}{\partial x_i} \right]^2. \quad (2.14)$$

2.3 Vortex Break-up

*Big whorls have little whorls
That feed on their velocity,
And little whorls have lesser whorls
And so on to viscosity.
- Lewis F. Richardson*

A commonly observed characteristic of turbulent flows is the presence of structures at all scales. These structures are usually small vortical structures, known as eddies. The characteristic length scale of the largest eddies in a turbulent flow are comparable to the length scale L of the fluid system while the size of the smallest eddies depend on the degree of turbulence of the system, with a continuous distribution of eddy sizes in between these extremes. The largest eddies of the system are created out of instabilities in the large-scale or mean flow of the system. These large eddies are in turn unstable and have very short typical lifespans - they break up into smaller eddies which further break-up into smaller vortices. It is found that most of the dissipation of kinetic energy happens via the smallest eddies, where viscous dissipation acts most strongly leading to the eddies breaking-up completely.

This cycle of creation of large eddies, break-up into smaller ones until they finally dissipate with the concurrent existence of eddies of all scales in a turbulent flow was first introduced by Richardson as the *energy cascade* [29], wherein kinetic energy is transferred by the process of vortex break-up from the largest scales, where viscosity is not significant, to the smallest scales, where viscous dissipation is dominant.

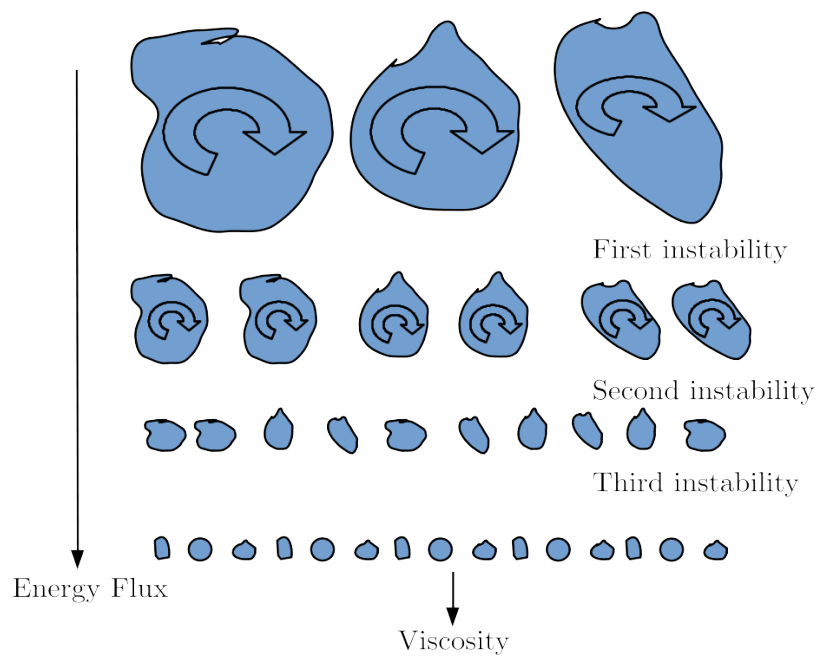


Figure 2.2: A diagram showing the break-up of eddies from the largest sized eddies in the system to the smallest due to inertial instabilities. Viscosity begins to play a more and more dominant role at smaller length scales and thus the smallest eddies dissipate rapidly. Image created by author based on Figure 1.14 in [1]

The next question that would arise naturally is - how does one estimate the size of the smallest eddies where dissipation is dominant? And how does this depend on the degree of turbulence quantified by Re ? Henceforth we denote η to be the length scale of the smallest eddy in the energy cascade. It is known experimentally that the break-up time associated with an eddy of size L and with typical velocity U is given by U/L . Thus, the rate of energy transfer to smaller scales by vortex break-up is given by

$$\Pi \sim U^2/(L/U) = U^3/L. \quad (2.15)$$

Assuming a statistically stationary situation where the rate of energy dissipation by viscosity via the smallest vortices is equal to the rate at which energy is passed to these smallest scales, we would have

$$\epsilon = U^3/L \quad (2.16)$$

where $\epsilon \sim \nu S_{ij} S_{ij}$ where S_{ij} is the strain-rate tensor already defined. Assuming all the viscous energy dissipation occurs at the smallest scales, we write

$$\epsilon \sim \nu(v^2/\eta^2), \quad (2.17)$$

where v is the velocity associated with the smallest eddies with length-scale η . Finally, this gives

$$U^3/L \sim \nu(v^2/\eta) \quad (2.18)$$

By noting that $Re = UL/\nu$ for the largest eddies, this gives

$$\eta \sim LRe^{-3/4} \quad (2.19)$$

Thus, the larger the Reynolds number and the more turbulent the flow, the smaller is η , the typical size of the smallest eddy. Thus, a more turbulent flow leads to the production of finer and finer scale structures. The length and velocity scales η and v respectively associated with the smallest eddies are known as the Kolmogorov micro-scale after the Soviet mathematician Andrey Kolmogorov.

An important note here is that the above derivation of the Kolmogorov microscales is heuristic in nature. The precise nature of the eddies and vortex break-up have not been given, nor have any of the assertions been justified, neither any way to validate this phenomenology by experiment has been provided. The microscales have been assumed to be uniform and isotropic, and is lacking a universal theoretical foundation or framework.

2.4 Kolmogorov's 1941 Theory

Thus far we have given a phenomenological description some processes such as vortex break-up and the Richardson cascade which are observed in turbulent flows. It still remains to understand the quantitative, measurable features of a turbulent flow. While the behaviour of the instantaneous velocity field of a turbulent flow is highly chaotic, its statistical properties vary smoothly and in a highly predictable manner. We have already seen that the equations describing a turbulent flow are the incompressible Navier-Stokes, which are purely deterministic in nature.

As a first step towards understanding the velocity field, for a given turbulent flow we distinguish between the *mean flow* and the fluctuations about this mean flow. For example, in a flow through a pipe as in Reynolds' experiment, the mean-flow is the steady flow along the length of the pipe while the small eddies formed in the turbulent regime represent the fluctuations. For any turbulent flow, we can express the instantaneous velocity field $\mathbf{u}(\mathbf{x}, t)$ as

$$\mathbf{u}(\mathbf{x}, t) = \bar{\mathbf{u}}(\mathbf{x}) + \mathbf{u}'(\mathbf{x}, t), \quad (2.20)$$

where $\bar{\mathbf{u}}(\mathbf{x})$ represents the time-averaged flow velocity at \mathbf{x} . Thus, \mathbf{u}' is the instantaneous deviation of the velocity from the mean flow velocity with the property $\overline{\mathbf{u}'} = 0$. The eddies of varying sizes and other flow features are contained in the term \mathbf{u}' rather than the mean flow, which is usually composed of a regular, large-scale pattern. The chaotic nature of turbulence is such that for two identical systems, minute variations in initial conditions lead to completely different realisations of the fluctuating component \mathbf{u}' while having the same mean flow $\bar{\mathbf{u}}$.

One of the most fundamental quantitative measure of a turbulent flow is the velocity correlation function Q_{ij} defined as

$$Q_{ij} = \langle u'_i(\mathbf{x})u'_j(\mathbf{x} + \mathbf{r}) \rangle \quad (2.21)$$

where u'_i are the individual components of the velocity \mathbf{u}' . $\langle \cdot \rangle$ represents the average over the entire fluid domain. The velocity correlation is a measure of how closely the fluid is related to itself in space and depends on \mathbf{x} , \mathbf{r} and t . In the statistically stationary situation that we mostly deal with, we have Q_{ij} independent of time. It is apparent that $Q \rightarrow 0$ for large \mathbf{r} , as the velocity of two points well separated from each other do not influence each other and hence we expect them to behave independently of each other for a turbulent flow. This is the case, for example, when $\mathbf{r} \gg L$ where L is the length-scale of the largest vortices in the Richardson cascade.

When $\mathbf{r} \rightarrow 0$, we get simply $Q_{ij} = \langle u'_i u'_j \rangle$. The horizontal correlation function Q_{xx} is given by $\langle u'^2 \rangle$ where u' is the horizontal component of the turbulent

fluctuations.

The case of *homogeneous* turbulence is when Q is independent of \mathbf{x} while *isotropic* turbulence is when Q does not depend on the direction of \mathbf{r} , instead depends solely on the magnitude $|\mathbf{r}|$.

While the correlation function describes the local structure of the velocity field, it does not encode information about the precise nature of the flow and does not provide precise information on the distribution of the vortices of different sizes, which is one of the defining features of a turbulent flow. Two closely related and important quantities are the *longitudinal velocity structure function* and the *kinetic energy spectrum* or simply the energy spectrum. The structure function of order p , S_p is defined as

$$S_p(r) = \langle [\delta u(r)]^p \rangle = \langle [u(\mathbf{x} + r\hat{\mathbf{e}}_x) - u(\mathbf{x})]^p \rangle. \quad (2.22)$$

Notice that $S_p \rightarrow 0$ for $r \rightarrow 0$ for all p . It is the second-order structure function $S_2(r)$ that is most widely used in the literature and is considered a measure of the energy contained in vortices with size $\leq r$.

The energy spectrum is defined as

$$E(k) = \frac{1}{2\pi} \int_{-\infty}^{\infty} R(r) e^{-ikr} dr, \quad (2.23)$$

where $R(r)$ is given by

$$R(r) = \frac{1}{2} \langle \mathbf{u}(\mathbf{x}) \cdot \mathbf{u}(\mathbf{x} + \mathbf{r}) \rangle, \quad (2.24)$$

which is closely related to the trace of Q_{ij} . Notice that for $r \rightarrow 0$, we have

$$\frac{1}{2} \langle \mathbf{u}^2 \rangle = \int_{-\infty}^{\infty} E(k) dk. \quad (2.25)$$

Here, equation (2.23) defines the Fourier Transform of $R(r)$, which is a convolution in space on \mathbf{u} . Thus, the energy spectrum captures the energy as a function of different wavenumbers. $E(k)$ is usually interpreted as the energy contained in the eddies with size corresponding to the wavenumber interval $k \rightarrow k + dk$ with $k \sim \pi/r$ and helps to understand the distribution of eddy sizes in a turbulent flow. This is also used to establish whether it is consistent with the Richardson picture of an energy cascade through vortex break-up. Crucially, the Richardson cascade relies on the existence of vortices with length-scale L where viscosity ν is not significant, as discussed above.

Andrey Kolmogorov in 1941 proposed two hypotheses to explain the small-scale structure of turbulent flows at high Re. His theory of turbulence is known

as the K41 theory of turbulence [30, 31]. Firstly, he hypothesised that the small-scale motions of a turbulent flow are isotropic in nature - that is while the largest scale eddies of the flow which are influenced by the average motion \bar{u} are not necessarily isotropic given the inherent anisotropies often present at the boundaries, the smaller scale features do not contain this directional information and hence are statistically isotropic. Given that the smallest-scales are isotropic, the Kolmogorov microscales introduced earlier by assuming a balance of the rate of energy cascading from the larger scales to the smaller scales and the viscous dissipation, must be universal in nature as the small-scales are universal in nature. That is, independent of the geometry of the flow and the boundary conditions, there exist small-scale turbulent velocity fluctuations whose structure depends solely on ν and ϵ . When the small-scales are isotropic, the balance of the rate of energy that is passed down from the larger scales to the smaller scales and the formulation of the Kolmogorov microscales, η and ν , derived above, is elevated from a heuristic exercise to a universal feature of all turbulent flows. These microscales could also have been inferred by simple dimensional analysis using Kolmogorov's similarity hypothesis as the starting point.

For a flow with high enough Re , consider eddies of length-scale r which is large enough so that $r \gg \eta$ and the viscous dissipation does not affect their dynamics, while at the same time $L \gg r$ and they remain unaffected by the anisotropy of the largest scales. The dynamics of these eddies are thus determined solely by the dissipation ϵ and are independent of ν . We can write the structure function for an eddy of scale r that takes the form

$$\langle [\delta u]^2 \rangle = \beta \epsilon^a r^b, \quad \eta \ll r \ll L, \quad (2.26)$$

where β is the Kolmogorov constant. This yields from dimensional analysis,

$$\langle [\delta u]^2 \rangle = \beta \epsilon^{\frac{2}{3}} r^{\frac{2}{3}}, \quad \eta \ll r \ll L. \quad (2.27)$$

The universal existence of this intermediate length-scale, known as the *inertial subrange*, is the third hypothesis of Kolmogorov's 1941 theory and it is known as Kolmogorov's two-thirds law. It also introduces another length-scale l , known as the inertial scale, where l is the largest length-scale that follows the above relation. Thus, $l < L$ and l must be far enough down the energy cascade that any information on the anisotropy of the largest scales is lost at length-scale l .

A necessary condition for the existence of such an intermediate length-scale is that η should be small enough compared to L . We have already seen that $\eta \sim Re^{-3/4}$. Thus, only flows with a high enough Reynolds number show the universal behaviour associated with the inertial sub-range. It is straight-forward to show that $\langle [\delta u]^2 \rangle \sim r^{\frac{2}{3}}$ corresponds to an energy spectrum with $E(k) \sim k^{-\frac{5}{3}}$. The existence of the inertial subrange can thus be inferred from experimental measurements,

either by measuring the energy spectrum or the structure function. Experimental measurements of the structure function have repeatedly validated Kolmogorov's hypothesis of universal similarity in both limits, $r \lll L$ as well as $\eta \ll r \ll L$ (see [32] and experiments cited within).

However, it is important to note that Kolmogorov's hypothesis is a general statement about the small-scale velocity increments δu - not only the *second order* structure function, but for S_p in general. In the spirit of Kolmogorov, we would have by dimensional analysis

$$\langle [\delta u]^p \rangle = \beta_p \epsilon^{\frac{p}{3}} r^{\frac{p}{3}}, \quad \eta \ll r \ll l, \quad (2.28)$$

where β_p is the p -th order Kolmogorov constant. Experimental measurements of the higher-order structure functions with $p > 3$ start to deviate from the above expression and show larger and larger discrepancy for increasing p . The first objections against the universal similarity hypothesis of Kolmogorov were raised by Landau [33], who argued insightfully that the local structure function should depend on the *local* rather than global energy dissipation, given that even the energy dissipation has a spatial structure and is not uniform. Understanding the reasons for the breakdown of Kolmogorov's similarity hypotheses for higher order structure functions and understanding the universal nature of the small-scale turbulent fluctuations, if such exists, is an area of active research. Kolmogorov himself suggested the so-called refined similarity hypothesis, with an exponent of $\frac{p}{3} + \frac{\mu}{18}(3p - p^2)$ for r . A detailed discussion on corrections to the K41 theory is beyond the scope of this thesis.

2.5 Why Turbulence is hard to solve

Thus far we have noted several features of turbulence which make it a particularly hard problem to solve. Despite arising from a deterministic equation, the velocity field of a turbulent flow is highly chaotic with rapid fluctuations with an extreme sensitivity to initial conditions. The presence of structures and vortices at all scales down to the smallest scale η coupled with the chaoticity necessitates resolving any direct numerical simulations down to the smallest scales, which get progressively smaller for increasing Re . While the instantaneous velocity field has all the above features, the statistical properties of a turbulent flow vary smoothly in space and time. However, a deterministic equation for these statistical properties is impossible to obtain without making certain assumptions or simplification which must necessarily be wholly empirical in nature.

Consider the Navier-Stokes equation of the form

$$\rho \frac{\partial u_i}{\partial t} + \rho(\mathbf{u} \cdot \nabla)u_i = -\frac{\partial p}{\partial x_i} + \frac{\partial \tau_{ij}}{\partial x_j}. \quad (2.29)$$

Time averaging the above yields

$$\rho \left[(\overline{\mathbf{u}} \cdot \nabla) \overline{u}_i + \overline{(\mathbf{u} \cdot \nabla) u_i} \right] = -\frac{\partial \overline{p}}{\partial x_i} + \frac{\partial \overline{\tau}_{ij}}{\partial x_j}, \quad (2.30)$$

which can be re-written as

$$\rho (\overline{\mathbf{u}} \cdot \nabla) \overline{u}_i = -\frac{\partial \overline{p}}{\partial x_i} + \frac{\partial}{\partial x_j} \left[\overline{\tau}_{ij} - \rho \overline{u'_i u'_j} \right]. \quad (2.31)$$

This is an equation of statistical quantities - $\overline{\mathbf{u}}$ and \overline{p} . However, as we can see, this involves a new term of the form $\overline{\rho u'_i u'_j}$ which are also statistical quantities not directly derivable from the Navier-Stokes equation. These are known as the Reynolds stresses and they represent momentum fluxes due to the turbulent fluctuations. We note that in the presence of a simple mean flow (ie., a laminar flow) where $\mathbf{u}(t) = \overline{\mathbf{u}}$ with no turbulent fluxes, the equation for the statistical averages are deterministic as well.

We could attempt to manipulate the equations to find an expression for the Reynolds stresses in terms of the other known quantities. However, this exercise is known to be futile and the Reynolds stresses can be found only in terms of terms of the form $\overline{\rho u'_i u'_j u'_k}$ which in turn depend on the fourth-order products of the velocity fluctuations and so on. This is known as the closure problem of turbulence. Thus, the only way to understand the statistical measures of a turbulent system is either by experimental measurements or by a full-scale direct numerical simulation.

Further, turbulent flows show *intermittency*, that is, the probability distribution functions (PDF) of the velocity field and the vorticity field (gradients of \mathbf{u}) show non-Gaussian statistics with a sharp peak and fatter tails. What this means is that while the magnitude of these fields is close to 0 over most of the domain, there exists intense patches of high velocity and vorticity which come alive from time to time and thus the PDFs of these variables is significant even for larger magnitudes far away from the mean. Thus, these intermittent turbulent fluctuations are not only chaotic, but their contribution to the statistical averages of the system relative to the mean-flow cannot be neglected.

Given these characteristics, the problem of turbulence is often found to be intractable, where every scale and every fluctuation playing an important role in the overall dynamics. This makes turbulent flows impossible to predict, even for simple flow systems.

Chapter 3

Rayleigh-Bénard Convection

Summary The advection-diffusion equation for the transport of a scalar in a fluid is introduced in dimensional and non-dimensional form along with the dimensionless Peclet number. Heat, or temperature, is then introduced as an active scalar and the Boussinesq approximation for small temperature fluctuations of a mildly compressible fluid is detailed, giving the Oberbeck-Boussinesq equation for thermal flows. The equations and boundary conditions describing the Rayleigh-Bénard system are introduced along with the important dimensionless quantities, the Rayleigh number, the Prandtl number and the Nusselt number. Following this, several typical qualitative features of Rayleigh-Bénard convection are explained, including the onset of convection, formation of plumes and transition to turbulence. Finally, well-known exact relations are derived which show the fundamental role of the Nusselt number and a brief account of the small-scale structure of turbulent Rayleigh-Bénard convection is given.

3.1 The Advection-Diffusion Equation

The concentration of a passive scalar C in a fluid follows the equation

$$\frac{\partial C}{\partial t} + (\mathbf{u} \cdot \nabla)C = D\nabla^2 C \quad (3.1)$$

where D with dimension [length²/time] is the diffusivity of the scalar, a measure of how the scalar diffuses through the system in the absence of a flow. The term $(\mathbf{u} \cdot \nabla)C$ is the advection term or the convection term which represents the transport of the scalar due to the motion of the fluid. Scalars generally take the form of dyes, smoke, pollutants, pollen etc. Equation (3.1) can be non-dimensionalised using the length scale L and velocity scale U similar to the Navier-Stokes equation in addition to a scalar concentration scale C_0 , giving

$$\frac{\partial C^*}{\partial t^*} + (\mathbf{u}^* \cdot \nabla^*) C^* = \frac{D}{UL} (\nabla^*)^2 C^*. \quad (3.2)$$

where $C^* = C/C_0$ is the dimensionless scalar concentration. Analogous to the Reynolds number, the *Peclet* number is defined as

$$\text{Pe} = \frac{UL}{D}, \quad (3.3)$$

and it measures the ratio of the advective scalar transport (transport due to the motion of the carrier fluid) to the diffusive scalar transport. Large Peclet number ($\text{Pe} \gg 1$) indicates that the time scale of diffusion is far slower compared to the large scale flow of the fluid. Thus, the scalar only follows the fluid trajectories and behaves similar to a marker. Diffusion becomes more significant at smaller Peclet number. Given that the length-scale of the largest eddies of the flow is similar to the length-scale of the flow L , diffusion acts only in the regime of smaller eddies which have $\text{Pe} \sim 1$. When $UL/D \gg 1$ and $UL/\nu \gg 1$, diffusion is restricted to the small-scale turbulent fluctuations of the flow alone.

3.2 Thermal Flows

A frequently encountered example of a scalar transported by turbulent fluids is heat or temperature. In a non-isothermal fluid with temperature variations, the temperature behaves like a passive scalar following equation (3.1) and D is replaced instead by κ which is the thermal diffusivity of the fluid. This is known as the heat equation. The advection of temperature by a fluid is particularly interesting to study as the temperature fluctuations in turn act on the fluid indirectly through a buoyancy force. Such thermal effects on fluids due to buoyancy are myriad and important across several natural as well as industrial systems, from ocean circulation and convection [34], to the atmosphere and clouds [35], from the mantle and core of the earth [36] and other planets and stars to the melting process of metals [37].

To be more precise, the change of temperature T of a region of fluid is accompanied by a change in density ρ . A region of lighter fluid surrounded by heavier, denser fluid is subject to a buoyancy force in the presence of gravity. This force goes as $\mathbf{f}_b \propto (\rho(T) - \rho(T_0)) \mathbf{g}$ where \mathbf{g} is the acceleration due to the gravity and $\rho(T)$ is the density of the fluid at temperature T while T_0 is the average steady fluid temperature. This modifies the Navier-Stokes equation as

$$\frac{\partial \mathbf{u}}{\partial t} + (\mathbf{u} \cdot \nabla) \mathbf{u} = -\frac{\nabla p}{\rho} + \nu \nabla^2 \mathbf{u} + \mathbf{f}_b. \quad (3.4)$$

There exists a seeming contradiction in the above statements - the buoyancy force is said to arise from fluctuations in density which arise from temperature fluctuations. However, the above is the *incompressible* Navier-Stokes equation which implies that the fluid has a fixed density ρ . This is resolved by considering the *Boussinesq approximation*. The Boussinesq approximation is a widely used approximation in the study of natural as well as industrial flows which are thermally driven. Here, the compressibility is ignored in all terms except the force term where it is multiplied by \mathbf{g} . The Boussinesq approximation is suitable for flows which show only small temperature variations or whose density varies very slowly for variations in temperature. For such systems, the density can be assumed to vary linearly with changing temperature. For a fluid with density ρ_0 at temperature T_0 , the density ρ at temperature T is given by

$$\rho(T) = \rho_0 [1 + \beta(T - T_0)] \quad (3.5)$$

where β is the coefficient of thermal expansion, which is also assumed to be constant for the small variations in temperature. Considering the Boussinesq approximation, the final fluid equations for a thermal flow are given by

$$\nabla \cdot \mathbf{u} = 0, \quad (3.6)$$

$$\frac{\partial \mathbf{u}}{\partial t} + (\mathbf{u} \cdot \nabla) \mathbf{u} = -\frac{\nabla p}{\rho} + \nu \nabla^2 \mathbf{u} - \beta(T - T_0) \mathbf{g}, \quad (3.7)$$

$$\frac{\partial T}{\partial t} + \mathbf{u} \cdot \nabla T = \kappa \nabla^2 T. \quad (3.8)$$

known as the Oberbeck-Boussinesq equations. This system of coupled equations describes the transport of heat advected by an incompressible fluid flow. The flow responds to the temperature fluctuations which locally drives hotter fluid in the vertically upward direction and colder fluid in the downward direction.

3.3 The Rayleigh-Bénard system

Thermal flows are abundant in nature, the most prominent being the atmosphere that is driven in large part by the heated land surface. The Rayleigh-Bénard convection is among the most widely studied model thermal flows. It consists of a layer of fluid held between two horizontal walls, with the lower wall at a uniform temperature T_d and the upper wall held at a uniform temperature T_u with $T_d - T_u = \Delta T > 0$. The heating of the fluid in the lower half of the domain and the accompanying cooling of the upper half of the domain leads to an unstable configuration where denser, heavier fluid lies on top of less dense, lighter fluid.

This is known as the *Rayleigh-Bénard instability*. It is a non-linear system that shows several types of pattern formation and allows researchers to study the various mechanisms of pattern formation. It has been described as the “granddaddy of canonical examples used to study pattern formation and behavior in spatially extended systems” [38]. The Rayleigh-Bénard convection is often studied as a model convective flow - A primary reason for this is that the Rayleigh-Bénard type instability leading to an overturning circulation and convective patterns is observed widely across geophysical flows. Thus, the Rayleigh-Bénard flow is considered a prototype of these geophysical flows.

The equations governing the Rayleigh-Bénard convection are the Oberbeck-Boussinesq equations (eqns. (3.6) - (3.8)) with the boundary conditions

$$T(z = 0) = T_d, \quad T(z = L_z) = T_u, \quad (3.9)$$

where L_z is the height of the fluid layer, for the temperature. The velocity is usually set to 0 at the vertical boundaries, known as the no-slip boundary condition. The main parameters of the flow are therefore the kinematic viscosity of the fluid ν , the thermal diffusivity of the fluid κ , the thermal expansion coefficient of the fluid β , the acceleration due to gravity \mathbf{g} , the applied temperature gradient ΔT and the vertical height L_z . The characteristic velocity scale of the system u_0 is defined as

$$u_0 = \sqrt{|\mathbf{g}|\beta(\Delta T)L_z}. \quad (3.10)$$

Further using L_z as the characteristic length-scale, ΔT as the characteristic temperature scale and L_z/u_0 as the characteristic time scale and using these to non-dimensionalise the equations gives

$$\nabla^* \cdot \mathbf{u}^* = 0, \quad (3.11)$$

$$\frac{\partial \mathbf{u}^*}{\partial t^*} + (\mathbf{u}^* \cdot \nabla^*) \mathbf{u}^* = -\nabla^* p^* + \sqrt{\frac{\text{Pr}}{\text{Ra}}} (\nabla^*)^2 \mathbf{u}^* + T^* \mathbf{e}_z, \quad (3.12)$$

$$\frac{\partial T^*}{\partial t^*} + \mathbf{u}^* \cdot \nabla^* T^* = \frac{1}{\sqrt{\text{PrRa}}} (\nabla^*)^2 T^*, \quad (3.13)$$

where the starred quantities represented the non-dimensional variables and derivatives as usual. Here Ra and Pr are the Rayleigh number and Prandtl number respectively, two non-dimensional numbers characterising the system, given by

$$\text{Ra} = |\mathbf{g}|\beta \frac{(\Delta T)L_z^3}{\nu\kappa}, \quad (3.14)$$

$$\text{Pr} = \frac{\nu}{\kappa}. \quad (3.15)$$

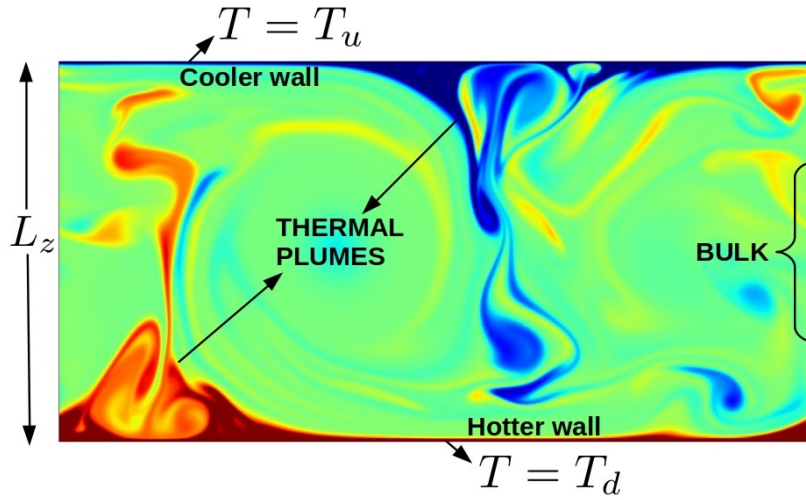


Figure 3.1: A sketch of turbulent 2D Rayleigh-Bénard convection at $Ra = 3.6 \times 10^8$ showing the hotter bottom wall, the cooler top wall, the thermal plumes which are detached from the thermal boundary layers and the well-mixed bulk layer with $T = 0$ on average.

The Rayleigh number measures the ratio of the buoyancy forces to the viscous, dissipative forces. In other words, the Rayleigh number measures the ratio of the forces which are setting the fluid into motion by increasing the degree of instability to the forces which resist the motion of the fluid. Thus, the Rayleigh number is a measure of the stability of the fluid system. The larger the Rayleigh number, the more unstable the system. The Prandtl number on the other hand measures the ratio of the viscous dissipation to the thermal dissipation.

The Rayleigh-Bénard system is stable at low Rayleigh numbers. The stable state is characterised by a linear vertical temperature profile given by

$$T(z) = T_d - \frac{\Delta T}{L_z} z. \quad (3.16)$$

The fluid remains at rest ($\mathbf{u} = 0$) and the transfer of heat from the bottom wall to the top wall occurs exclusively through conduction through the fluid. This is the simplest solution for the Rayleigh-Bénard (RB) system and is known as the conductive solution. The fluid is stable to small perturbations, ie., small fluctuations applied on the fluid dissipate away and the fluid returns to the conductive solution state.

This is the situation until a critical Rayleigh number $Ra_c = 1708$. For $Ra > Ra_c$, the fluid ceases to be at rest. The temperature profile is linear only near the vertical boundaries up to a certain distance characterising the thermal bound-

ary while the temperature is uniform in the *bulk*. An overturning circulation is established, usually characterised by several *plumes* arising from adjacent large counter-rotating vortices which occupy almost the entire domain. Plumes are of two kinds - hot and cold. Hot (cold) plumes are characterised by a large region of hot rising (cold falling) fluid, often with a characteristic mushroom cloud shape. They are formed as a detachment of the thermal boundary layer. Plumes have a large contribution in driving the flow and form a significant fraction of the heat transfer, which is dominated by convection rather than conduction for larger Ra.

On increasing Ra above Ra_c , the flow still remains smooth and laminar. At around $Ra = 10^7$, the flow starts to transition to a turbulent state, characterised by the usual features of a turbulent flow. Further, the plumes, which are well-defined and smooth for the laminar regime start to lose their mushroom like shape and become irregular shaped and harder to distinguish from the background flow. The thermal boundaries become narrower and narrower as the turbulence ensures effective mixing of the temperature field, leading to a large bulk region with a uniform temperature (on average).

An important parameter for the Rayleigh-Bénard system is the aspect ratio Γ , which is the ratio of the larger horizontal dimension to the height L_z , which plays an important role in determining the patterns formed for various ranges of Ra and Pr. The discussions of the variation in the patterns observed for varying aspect ratio is beyond the scope of this thesis.

3.4 Nusselt Number

There are still open problems in the understanding of RB convection, the chief being the scaling of the Nusselt number as a function of Ra and Pr. The Nusselt number Nu is a dimensionless response parameter of the RB system defined as

$$Nu = Nu(z) = \frac{\langle vT - \kappa\partial_z T \rangle_{A,t}}{\frac{\kappa\Delta T}{L_z}}. \quad (3.17)$$

For the RB convection, Nu does not vary with height and it has a constant value. This can be easily verified by integrating equation (3.8) over any horizontal plane and taking a time average, which leads to

$$\langle v\partial_z T - \kappa\partial_z^2 T \rangle_{A,t} = 0,$$

that is, $\partial_z(Nu) = 0$. The denominator of the Nusselt number is a non-dimensionalisation factor.

Notice that for the conductive solution, $\mathbf{u} = 0$, while $\partial_z T = -(\Delta T)/L_z$, which leads to $Nu = 1$. When $\mathbf{u} \neq 0$ and the fluid is set into motion, Nu attains a

value greater than 1. It is important to note that the vT term has a positive value since hotter regions of the fluid are associated with updrafts and vice-versa for the colder regions of the fluid. Thus, this is a heat transport term, with $-\kappa\partial_z T$ being the term that measures the conductive heat transport in the positive z direction. The Nusselt number measures how significant the convective heat transport is compared to the conductive heat transport.

The respective contribution from each term varies with height z . In the bulk region, the average vertical temperature profile is uniform. Due to the imposed no-slip boundary conditions, it is only the second term which contributes significantly to the Nusselt number and the temperature profile here is nearly linear until z approaches the bulk and T approaches $T_0 = T_d + (\Delta T)/2$. Thus we can write

$$\text{Nu} \sim \frac{\kappa(\Delta T)/\ell_{\text{TB}}}{\kappa(\Delta T)/L_z}, \quad (3.18)$$

where ℓ_{TB} is the length of the thermal boundary region where the temperature profile is nearly linear. Thus, the Nusselt is closely related to the thermal boundary thickness and $\ell_{\text{TB}} = L_z/\text{Nu}$ is often used in the literature as a characteristic length-scale of the thermal boundary. Further, when ΔT (or equivalently, Ra) is increased, the net heat transfer from the bottom wall to the top wall increases in a commensurate way, leading to an increase in Nu as well. The degree of turbulence and associated small-scale fluctuations also increase the net heat transfer.

Several theories have been suggested to account for the vast experimental and numerical data on the scaling of Nu with Ra and Pr , that is $\text{Nu}(\text{Ra}, \text{Pr}) \sim \text{Ra}^\gamma \text{Pr}^\lambda$. While a detailed account of the experimental and numerical studies trying to ascertain the exact nature of this scaling is beyond the scope of this thesis, the interested reader may refer to the work of Ahlers et. al, 2009 [39] and references therein. It is generally accepted that for a wide range of Ra , Nu scales as $\text{Nu} \sim \text{Ra}^{0.3}$. It is also theorised that there exists an *ultimate regime* of turbulent RB convection at very high Ra ($\geq 10^{14}$) where the scaling exponent is closer to $1/2$ [40, 41].

3.4.1 Exact Relations

There exist two important and fundamental exact relations (see [42, 43]) relating the viscous dissipation and the thermal dissipation to the Nusselt number and other parameters of the RB flow. We first derive the exact relation between the volume averaged viscous dissipation ϵ and the Nusselt number. Consider the fluid evolution equation

$$\partial_t \mathbf{u} + (\mathbf{u} \cdot \nabla) \mathbf{u} = -\nabla p + \nu \nabla^2 \mathbf{u} - \beta T \mathbf{g}. \quad (3.19)$$

Taking the dot product of eq. (3.19) with \mathbf{u} and averaging over the whole volume, we get

$$\begin{aligned} \frac{1}{2} \frac{d}{dt} \langle (\mathbf{u} \cdot \mathbf{u}) \rangle_{V,t} + \frac{1}{2} \langle \mathbf{u} \cdot \nabla (\mathbf{u} \cdot \mathbf{u}) \rangle_{V,t} \\ = - \langle \mathbf{u} \cdot \nabla p \rangle_{V,t} + \nu \langle \mathbf{u} \cdot \nabla^2 \mathbf{u} \rangle_{V,t} + \beta g \langle u_z T \rangle_{V,t}. \end{aligned} \quad (3.20)$$

In the stationary state, the terms of the form $\frac{d\langle \cdot \rangle_{V,t}}{dt}$ vanish. Using in addition the incompressibility condition ($\nabla \cdot \mathbf{u} = 0$), we have

$$\langle \mathbf{u} \cdot \nabla (\mathbf{u} \cdot \mathbf{u}) \rangle_V = \langle \nabla \cdot [\mathbf{u}(\mathbf{u} \cdot \mathbf{u})] \rangle_V = 0 \quad (3.21)$$

$$\langle \mathbf{u} \cdot \nabla p \rangle_V = \langle \nabla \cdot (\mathbf{u}p) \rangle_V = 0 \quad (3.22)$$

$$\begin{aligned} \langle \mathbf{u} \cdot \nabla^2 \mathbf{u} \rangle_V &= \frac{1}{2} \langle \nabla \cdot \nabla (\mathbf{u} \cdot \mathbf{u}) \rangle_V - \sum_{i,j} \left\langle \left(\frac{\partial u_j}{\partial x_i} \right)^2 \right\rangle_V \\ &= - \sum_{i,j} \left\langle \left(\frac{\partial u_j}{\partial x_i} \right)^2 \right\rangle_V \\ &= - \frac{1}{2} \sum_{i,j} \left\langle \left(\frac{\partial u_i}{\partial x_j} + \frac{\partial u_j}{\partial x_i} \right)^2 \right\rangle_V. \end{aligned} \quad (3.23)$$

So, equation (3.20) becomes

$$\frac{\nu}{2} \sum_{i,j} \left\langle \left(\frac{\partial u_i}{\partial x_j} + \frac{\partial u_j}{\partial x_i} \right)^2 \right\rangle_{V,t} = \beta g \langle u_z T \rangle_{V,t}, \quad (3.24)$$

or

$$\epsilon \equiv \frac{\nu}{2} \sum_{i,j} \left\langle \left(\frac{\partial u_i}{\partial x_j} + \frac{\partial u_j}{\partial x_i} \right)^2 \right\rangle_{V,t} = \beta g \langle u_z T \rangle_{V,t}. \quad (3.25)$$

Using

$$\text{Nu} = \frac{\langle vT \rangle_{V,t}}{\frac{\kappa \Delta T}{L_z}} + 1, \quad (3.26)$$

we get

$$\epsilon = \frac{\nu^3}{L_z^4} (\text{Nu} - 1) \text{RaPr}^{-2}. \quad (3.27)$$

For the thermal dissipation given by

$$\epsilon_\theta \equiv \kappa \langle (\partial_i T(\mathbf{x}, t))^2 \rangle_V, \quad (3.28)$$

We have the heat equation given by

$$\frac{\partial T}{\partial t} + \mathbf{u} \nabla T = \kappa \nabla^2 T. \quad (3.29)$$

Similar to above, we now take the product of T with equation (3.29) and average it over the entire domain and time to give

$$\begin{aligned} \frac{1}{2} \frac{d\langle T^2 \rangle_{V,t}}{dt} + \frac{1}{2} \langle \mathbf{u} \cdot \nabla (T^2) \rangle_{V,t} \\ = \kappa \langle T \nabla^2 T \rangle_{V,t} = \kappa \langle \nabla \cdot (T \nabla T) \rangle_{V,t} - \kappa \langle |\nabla T|^2 \rangle_{V,t}. \end{aligned} \quad (3.30)$$

Using once again the stationary condition and the incompressibility condition to give

$$\langle \mathbf{u} \cdot \nabla (T^2) \rangle_V = \langle \nabla \cdot (\mathbf{u} T^2) \rangle_V = 0. \quad (3.31)$$

Then, equation (3.30) becomes

$$\kappa \langle |\nabla T|^2 \rangle_{V,t} = \kappa \langle \nabla \cdot (T \nabla T) \rangle_{V,t}. \quad (3.32)$$

Or

$$\epsilon_\theta = \kappa \langle \nabla \cdot (T \nabla T) \rangle_{V,t}. \quad (3.33)$$

This can further be simplified using the Gauss theorem and writing it in terms of a surface integral

$$\kappa \langle \nabla \cdot (T \nabla T) \rangle_{V,t} = \frac{\kappa}{L_z} \left[\left\langle T \frac{\partial T}{\partial z} \right\rangle_{z=L_z} - \left\langle T \frac{\partial T}{\partial z} \right\rangle_{z=0} \right]. \quad (3.34)$$

Noting that at $z = 0$, $T = T_d$, at $z = L_z$, $T = T_u$ with $\Delta T = T_u - T_d$ and further for both the top and bottom boundaries $\mathbf{u} = 0$, we get

$$- \kappa \left\langle \frac{\partial T}{\partial z} \right\rangle_{z=0} = \kappa \frac{\Delta T}{L_z} \text{Nu} \quad (3.35)$$

finally leading to

$$\epsilon_\theta = \kappa \frac{(\Delta T)^2}{L_z^2} \text{Nu}. \quad (3.36)$$

These exact relations and the monotonic scaling of Nu with Ra show that the Nusselt number is an extremely crucial and important response parameter that captures several dynamical features of the flow such as the magnitude of convective heat transfer, the degree of turbulence, the degree of turbulent mixing of the temperature field. Finally, the Nusselt number is also a measure of the correlation between the vertical velocity v and the temperature field T in the bulk of the domain.

3.5 Scaling in the Rayleigh-Bénard Convection

The small scale structure of the velocity field in a turbulent Rayleigh-Bénard convective system shows scaling compatible with Kolmogorov's K41 theory, with the second order structure function S_2 , the case of $p = 2$ in equation (2.22) scaling as

$$S_2(r) \sim (\epsilon r)^{2/3} \quad (3.37)$$

in the inertial subrange. Similar to the structure function for the velocity field, a second-order structure function for the temperature field S_2^θ can also be defined as

$$S_2^\theta = \langle (\theta(\mathbf{x} + \mathbf{r}) - \theta(\mathbf{x}))^2 \rangle \quad (3.38)$$

The scaling of S_2^θ for an advected passive scalar in the inertial range of a turbulent flow was deduced by Obukhov [44] and Corrsin [45]. Generalising the arguments of Kolmogorov, they assumed that the temperature depend on the thermal dissipation ϵ_θ in addition to the viscous dissipation, giving a scaling of

$$S_2^\theta(r) \sim \epsilon_\theta \epsilon^{-1/3} r^{2/3}. \quad (3.39)$$

However, this is based on arguments for passive scalars, whereas temperature is an example of an active scalar that modifies the underlying fluid flow. Assuming that the buoyancy forcing plays an important role at all scales and the small-scale structure depends on $\beta|\mathbf{g}|$ and ϵ_θ , the form of the structure function suggested by Bolgiano and Obukhov [46, 47] is obtained, given by,

$$S_2(r) \sim \epsilon_\theta^{2/5} (\beta|\mathbf{g}|)^{4/5} r^{6/5}, \quad (3.40)$$

$$S_2^\theta(r) \sim \epsilon_\theta^{4/5} (\beta|\mathbf{g}|)^{-2/5} r^{2/5}. \quad (3.41)$$

This is known as the Bolgiano-Obukhov scaling, or BO59. Comparing equations (3.39) and (3.41) gives the so-called Bolgiano crossover length-scale L_B between the K41 scaling and BO59 scaling

$$L_B = \epsilon_u^{5/4} \epsilon_\theta^{-3/4} (\beta|\mathbf{g}|)^{-3/2}. \quad (3.42)$$

For length-scales smaller than the integral length scale L while still larger than L_B , the BO59 scaling is expected. At smaller scales so that $\eta \ll r \ll L_B$, K41 scaling is still expected. However the BO59 scaling, which implies an energy spectrum $\sim k^{-11/5}$ has not been conclusively identified in experiments or simulations. For a complete survey of the small-scale structure of the velocity and

the temperature fields in Rayleigh-Bénard convection and the experimental and numerical attempts to identify the BO59 type scaling, the reader may refer to the review of Lohse et. al [48].

Chapter 4

The Lattice Boltzmann Method

Summary An overview of the Lattice Boltzmann method is provided, first by motivating the equations of the kinetic theory of gases and the Maxwell-Boltzmann distribution. Following this, the Boltzmann equation is studied. The Boltzmann equation is discretised in velocity-space using Hermite polynomial expansions followed by the application of the Gauss-Hermite quadrature rule. Similarly, a brief account of the space-discretisation is given to finally derive the Lattice Boltzmann equation. The Chapman-Enskog analysis is reproduced to show that the moments of the discrete populations that solve the Lattice Boltzmann equation are a solution to the Navier-Stokes equation, accurate up to second order. The implementation of the Lattice Boltzmann algorithm is then described in a nutshell, along with the calculation of the hydrodynamic quantities. The modifications to the equation to include a body-force term is described followed finally by the extensions of the Lattice Boltzmann algorithm to include scalar transport by the fluid. This chapter is meant to present an overview of the mathematical background for the design of the Lattice-Boltzmann algorithm rather than a rigorous mathematical derivation of the same.

4.1 Introduction

The Lattice Boltzmann method is a *mesoscopic* method to solve the equations of fluid dynamics (Navier-Stokes equations) numerically. The mesoscopic scale is an intermediate regime where the length-scale is large enough that the dynamics of individual molecules is not significant but still small enough that the continuum approximation is invalid. In principle, every fluid system can be solved by solving the microscopic dynamics. However, that would prove to be computationally extremely expensive and with a resolution far greater than necessary. The Lattice Boltzmann approach uses the kinetic theory of gases that describes the distribu-

tion and statistics of particles in a gas with time-scales corresponding to t_{mfp} , the mean collision time between the gas particles.

4.2 Kinetic Theory

4.2.1 The Distribution Function

The basis of all kinetic theory is the distribution function $f(\mathbf{x}, \boldsymbol{\xi}, t)$ where which represents the density of particles with position \mathbf{x} and moving with velocity $\boldsymbol{\xi} = (\xi_x, \xi_y, \xi_z)$ at time t , having units of $[\text{mass}][\text{time}]^3/[\text{length}]^6$. Thus the distribution function contains all the dynamic information about the gas particles and hence, the macroscopic information on the gas as well. For example, the mass density of the gas $\rho(\mathbf{x}, t)$ can be obtained by integration over the velocity space as

$$\rho(\mathbf{x}, t) = \int f(\mathbf{x}, \boldsymbol{\xi}, t) d^3\xi. \quad (4.1)$$

Similarly, the energy density is obtained by integrating the product of $|\boldsymbol{\xi}|^2$ and f over the velocity space. This expression for energy contains both, the internal energy of the gas particles as well as the kinetic energy due to the translation of the particles with velocity \mathbf{u} . For polyatomic gases, the internal energy comprises additional motions such as rotations and vibrations. Here we define the relative velocity \mathbf{v} as

$$\mathbf{v}(\mathbf{x}, t) = \boldsymbol{\xi}(\mathbf{x}, t) - \mathbf{u}(\mathbf{x}, t), \quad (4.2)$$

where \mathbf{u} is the mean local velocity of the gas particles. While the total kinetic energy of the gas is due to \mathbf{u} , the internal energy including thermal fluctuations is due to the relative velocities \mathbf{v} .

4.2.2 The equilibrium distribution

When a gas is left alone for a long time ($t \gg t_{\text{mfp}}$), the gas is described by the **equilibrium distribution function** f^{eq} . When considered in a reference frame moving along with the gas with velocity \mathbf{u} , the equilibrium distribution function can be assumed to be isotropic in velocity space - any anisotropy in the motion of the gas particles can be assumed to have been evened out by collisions among gas particles. Thus, the equilibrium distribution function depends only on the magnitude of the relative velocity $|\mathbf{v}|$ as $f^{\text{eq}}(\mathbf{x}, |\mathbf{v}|, t)$.

One further assumption is made about the equilibrium distribution function - we assume that $f^{\text{eq}}(|\mathbf{v}|^2)$ has a separable form and the 3D equilibrium distribution is simply the product of 3 individual 1D equilibrium distributions f_{1D} , ie.,

$$f^{\text{eq}}(|\mathbf{v}|^2) = f^{\text{eq}}(v_x^2 + v_y^2 + v_z^2) = f_{1\text{D}}^{\text{eq}}(v_x^2) f_{1\text{D}}^{\text{eq}}(v_y^2) f_{1\text{D}}^{\text{eq}}(v_z^2). \quad (4.3)$$

For a given $|\mathbf{v}|^2$, we have $f^{\text{eq}}(|\mathbf{v}|^2) = \text{const}$, thus

$$\ln f_{1\text{D}}^{\text{eq}}(v_x^2) + \ln f_{1\text{D}}^{\text{eq}}(v_y^2) + \ln f_{1\text{D}}^{\text{eq}}(v_z^2) = \text{const}. \quad (4.4)$$

A (not necessarily unique) solution that satisfies this condition is of the form $\ln f_{1\text{D}}^{\text{eq}}(v_x^2) = a + bv_x^2$ where a and b are generic constants, since

$$\ln f_{1\text{D}}^{\text{eq}}(v_x^2) + \ln f_{1\text{D}}^{\text{eq}}(v_y^2) + \ln f_{1\text{D}}^{\text{eq}}(v_z^2) = 3a + b(v_x^2 + v_y^2 + v_z^2) \quad (4.5)$$

which is a constant when $|\mathbf{v}|^2 = v_x^2 + v_y^2 + v_z^2$ is a constant. Thus, we finally obtain the equilibrium distribution function of the form

$$f^{\text{eq}}(|\mathbf{v}|) = e^{3a} e^{b|\mathbf{v}|^2}. \quad (4.6)$$

For a mono-atomic gas with temperature T , the precise form of the equilibrium distribution is given by

$$f^{\text{eq}}(\mathbf{x}, |\mathbf{v}|, t) = \rho \left(\frac{1}{2\pi RT} \right)^{3/2} e^{-|\mathbf{v}|^2/(2RT)}. \quad (4.7)$$

R here is the universal gas constant. The above detailed derivation gives a possible equilibrium distribution that satisfies all the conditions placed on it and is similar to Maxwell's procedure to obtain the equilibrium distribution function. The same can also be obtained through the method of Boltzmann using arguments from statistical mechanics [49]. This form is known as the *Maxwell-Boltzmann* distribution.

4.2.3 The Boltzmann equation

Given a distribution function $f(\mathbf{x}, \boldsymbol{\xi}, t)$, we are interested in the evolution of this function, or df/dt . We can write

$$\frac{df}{dt} = \left(\frac{\partial f}{\partial t} \right) \frac{dt}{dt} + \left(\frac{\partial f}{\partial x_i} \right) \frac{dx_i}{dt} + \left(\frac{\partial f}{\partial \xi_i} \right) \frac{d\xi_i}{dt} \quad (4.8)$$

to be the total change in f . Notice that $\frac{dx_i}{dt} = \xi_i$ and $\frac{d\xi_i}{dt} = F_i/\rho$ is a force per unit mass applied on the gas. Denoting $\frac{df}{dt}$ as $\Omega(f)$, we have the **Boltzmann equation**

$$\frac{\partial f}{\partial t} + \xi_i \frac{\partial f}{\partial x_i} + \frac{F_i}{\rho} \frac{\partial f}{\partial \xi_i} = \Omega(f) \quad (4.9)$$

The form of the equation resembles an advection equation, wherein the distribution function is advected with velocity $\boldsymbol{\xi}$, with forces that modify this velocity in the form of \boldsymbol{F} . $\Omega(f)$ is analogous to a source term representing the local modification of f , due to collisions between the particles. $\Omega(f)$ is thus known as the *collision operator*.

For monoatomic gases, collisions conserve mass, momentum as well as translational energy. This can be expressed in terms of $\Omega(f)$ as

$$\int \Omega(f) d^3\xi = 0, \quad (4.10)$$

$$\int \boldsymbol{\xi} \Omega(f) d^3\xi = 0, \quad (4.11)$$

$$\int |\boldsymbol{\xi}|^2 \Omega(f) d^3\xi = 0, \quad (4.12)$$

$$\int |\boldsymbol{v}|^2 \Omega(f) d^3\xi = 0. \quad (4.13)$$

The constraints respectively represent the conservation of mass, conservation of momentum, conservation of total energy and the conservation of internal energy. Lattice Boltzmann methods generally use the collision operator of the form

$$\Omega(f) = -\frac{1}{\tau}(f - f^{\text{eq}}) \quad (4.14)$$

where τ is a relaxation time parameter. This form of the collision operator is known as the BGK collision operator after Bhatnagar, Gross and Krook and it assumes that a gas with distribution function f has a natural tendency to relax to the equilibrium distribution f^{eq} with a characteristic time scale τ . The BGK operator is particularly popular due to its simplicity and ease of implementation.

At first sight, the mesoscopic equations involving f seem more complicated than the Navier-Stokes equations - f depends on 7 quantities for a three-dimensional system viz., three components of space x_i , three components of velocity ξ_i and time t . Further, the distribution function and the Boltzmann equation describe mesoscale dynamics of a gas with no apparent connection to the flow of a fluid. As it turns out, the Navier-Stokes equation describing macroscopic fluid behaviour can be obtained directly from the Boltzmann equation. However, this first requires a way to estimate the distribution function f as well as the equilibrium distribution function f^{eq} . This will be done in the next section, where we appropriately discretise the Boltzmann equation to make it amenable to numerical implementation and finally after that we will show how the discretised Boltzmann equation, or the *Lattice Boltzmann equation* leads to the Navier-Stokes equation.

4.2.4 Discretisation of the Velocity

As noted, the Boltzmann equation is seemingly more complex than the Navier-Stokes equation. However, it is important to note here that the specific physics and details underlying the Boltzmann equation is not important to the problem at hand. Instead, we are interested in obtaining the correct macroscopic or hydrodynamic quantities, which we accomplish through a simplified equilibrium function f^{eq} and a discrete velocity space.

First, we non-dimensionalise the Boltzmann equation (equation (4.9)) by defining a characteristic length ℓ , velocity V , time $t_0 = \ell/V$ and density ρ_0 . This gives

$$\frac{\partial f^*}{\partial t^*} + \xi_\alpha^* \frac{\partial f^*}{\partial x_\alpha^*} + \frac{F_\alpha^*}{\rho^*} \frac{\partial f^*}{\partial \xi_\alpha^*} = \Omega^*(f^*), \quad (4.15)$$

where $f^* = fV^d/\rho_0$, $F_\alpha^* = F_\alpha\ell/(\rho_0V^2)$, $\rho^* = \rho/\rho_0$, $\Omega^* = \Omega\ell V^2/\rho_0$ and the derivatives are non-dimensionalised as

$$\frac{\partial}{\partial t^*} = \frac{\ell}{V} \frac{\partial}{\partial t}, \quad (4.16)$$

$$\frac{\partial}{\partial x^*} = l \frac{\partial}{\partial x}, \quad (4.17)$$

$$\frac{\partial}{\partial \xi^*} = V \frac{\partial}{\partial \xi}. \quad (4.18)$$

This gives the equilibrium function

$$f^{\text{eq}*} = \frac{\rho^*}{(2\pi\theta^*)^{d/2}} e^{-(\xi^* - \mathbf{u}^*)^2/(2\theta^*)} \quad (4.19)$$

with $\theta^* = RT/V^2$ being the non-dimensional temperature. Henceforth, the $*$ symbol will be dropped and we will continue to work only with the non-dimensional equation.

Here we will give a brief introduction to the *Hermite polynomials* along with some basic properties of these polynomials. A more substantive mathematical account of the same can be found in References [50, 51]. Hermite polynomials arise naturally in quantum mechanics as wave functions for harmonic potentials. They are generated in their 1D form via the weight function ω given by

$$\omega(x) = \frac{1}{\sqrt{2\pi}} e^{-x^2/2}. \quad (4.20)$$

The Hermite polynomial $H^{(n)}(x)$ of n -th order is given by

$$H^{(n)}(x) = (-1)^n \frac{1}{\omega(x)} \frac{d^n}{dx^n} \omega(x), \quad (4.21)$$

where n is a positive integer. In d dimensions, the corresponding Hermite polynomial $\mathbf{H}^{(n)}$ and weight function ω are

$$\mathbf{H}^{(n)}(\mathbf{x}) = (-1)^n \frac{1}{\omega(\mathbf{x})} \nabla^{(n)} \omega(\mathbf{x}), \quad \omega(\mathbf{x}) = \frac{1}{(2\pi)^{d/2}} e^{-\mathbf{x}^2/2}, \quad (4.22)$$

where both $\mathbf{H}^{(n)}$ and $\nabla^{(n)}$ are tensors of rank n . To be precise,

$$\nabla_{\alpha_1 \dots \alpha_n}^{(n)} = \frac{\partial}{\partial x_{\alpha_1}} \dots \frac{\partial}{\partial x_{\alpha_n}} \quad (4.23)$$

where the α_i run from 1 to d . For the $d = 3$ case, $\alpha_i \in \{x, y, z\}$. Hermite Polynomials in 1 dimension are orthogonal with respect to $\omega(x)$:

$$\int_{-\infty}^{\infty} \omega(x) H^{(n)}(x) H^{(m)}(x) dx = n! \delta_{nm}^{(2)} \quad (4.24)$$

where $\delta_{nm}^{(2)}$ is the Kronecker delta function which has $\delta_{nm}^{(2)} = 1$ when $n = m$ and $\delta_{nm}^{(2)} = 0$ otherwise. The orthogonality extended to d dimensions is expressed as

$$\int \omega(\mathbf{x}) \mathbf{H}_{\alpha}^{(n)} \mathbf{H}_{\beta}^{(m)}(\mathbf{x}) d^d x = \prod_{i=1}^d n_i! \delta_{nm}^{(2)} \delta_{\alpha\beta}^{(n+m)} \quad (4.25)$$

where $\delta_{\alpha\beta}^{(n+m)} = 1$ if and only if $\alpha = (\alpha_1, \dots, \alpha_n)$ is a permutation of $\beta = (\beta_1, \dots, \beta_n)$. For $d = 3$, this reads

$$\int \omega(\mathbf{x}) \mathbf{H}_{\alpha}^{(n)} \mathbf{H}_{\beta}^{(m)}(\mathbf{x}) d^3 x = n_x! n_y! n_z! \delta_{nm}^{(2)} \delta_{\alpha\beta}^{(n+m)}. \quad (4.26)$$

Further, the Hermite Polynomials form a complete basis in \mathbb{R}^d and any continuous, smooth function in d dimensions can be expressed as

$$f(\mathbf{x}) = \omega(\mathbf{x}) \sum_{n=0}^{\infty} \frac{1}{n!} \mathbf{a}^{(n)} \cdot \mathbf{H}^{(n)}(\mathbf{x}), \quad \mathbf{a}^{(n)} = \int f(\mathbf{x}) \mathbf{H}^{(n)}(\mathbf{x}) d^d x. \quad (4.27)$$

Here, the dot product $\mathbf{a}^{(n)} \cdot \mathbf{H}^{(n)}(\mathbf{x})$ is defined as the summation over all indices $a_{\alpha_1 \dots \alpha_n}^{(n)} H_{\alpha_1 \dots \alpha_n}^{(n)}$. This is known as the Hermite series expansion while the tensors $\mathbf{a}^{(n)}$ are known as the Hermite expansion coefficients.

We first note a very important point - the equilibrium distribution function has an identical form to the weight function.

$$f^{\text{eq}}(\rho, \mathbf{u}, \theta, \boldsymbol{\xi}) = \frac{\rho}{(2\pi\theta)^{d/2}} e^{-(\boldsymbol{\xi}-\mathbf{u})^2/(2\theta)} = \frac{\rho}{\theta^{d/2}} \omega\left(\frac{\boldsymbol{\xi}-\mathbf{u}}{\sqrt{\theta}}\right). \quad (4.28)$$

Now we apply the Hermite series expansions to f^{eq} in $\boldsymbol{\xi}$ -space:

$$f^{\text{eq}}(\rho, \mathbf{u}, \theta, \boldsymbol{\xi}) = \omega(\boldsymbol{\xi}) \sum_{n=0}^{\infty} \frac{1}{n!} \mathbf{a}^{(n),\text{eq}}(\rho, \mathbf{u}, \theta) \cdot \mathbf{H}^{(n)}(\boldsymbol{\xi}) \quad (4.29)$$

and

$$\mathbf{a}^{(n),\text{eq}}(\rho, \mathbf{u}, \theta) = \int f^{\text{eq}}(\rho, \mathbf{u}, \theta, \boldsymbol{\xi}) \mathbf{H}^{(n)}(\boldsymbol{\xi}) d^d \boldsymbol{\xi}. \quad (4.30)$$

Using the relation in equation (4.28), we can calculate the series coefficients for the equilibrium distribution function.

$$\mathbf{a}^{(n),\text{eq}} = \frac{\rho}{\theta^{d/2}} \int \omega\left(\frac{\boldsymbol{\xi}-\mathbf{u}}{\sqrt{\theta}}\right) \mathbf{H}^{(n)}(\boldsymbol{\xi}) d^d \boldsymbol{\xi}. \quad (4.31)$$

Substituting $\boldsymbol{\eta} = \boldsymbol{\xi} - \mathbf{u}$ gives

$$\mathbf{a}^{(n),\text{eq}} = \rho \int \omega(\boldsymbol{\eta}) \mathbf{H}^{(n)}(\sqrt{\theta}\boldsymbol{\eta} + \mathbf{u}) d^d \boldsymbol{\eta} \quad (4.32)$$

Calculating these yields

$$a^{(0),\text{eq}} = 1, \quad (4.33a)$$

$$a_{\alpha}^{(1),\text{eq}} = \rho u_{\alpha}, \quad (4.33b)$$

$$a_{\alpha\beta}^{(2),\text{eq}} = \rho(u_{\alpha}u_{\beta} + (\theta - 1)\delta_{\alpha\beta}), \quad (4.33c)$$

$$a_{\alpha\beta\gamma}^{(3),\text{eq}} = \rho[u_{\alpha}u_{\beta}u_{\gamma} + (\theta - 1)(\delta_{\alpha\beta}u_{\gamma} + \delta_{\beta\gamma}u_{\alpha} + \delta_{\gamma\alpha}u_{\beta})] \quad (4.33d)$$

It is clear that the first 3 coefficients in the Hermite series expansion of f^{eq} are related to the density, momentum and energy respectively. Further, the conserved quantities can be expressed in terms of the Hermite series coefficients of the (non-equilibrium) particle distribution function f :

$$a^{(0),\text{eq}} = \int f^{\text{eq}} d^d \boldsymbol{\xi} = \rho = \int f d^d \boldsymbol{\xi} = a^{(0)}, \quad (4.34a)$$

$$a_{\alpha}^{(1),\text{eq}} = \int f^{\text{eq}} \xi_{\alpha} d^d \boldsymbol{\xi} = \rho u_{\alpha} = \int f \xi_{\alpha} d^d \boldsymbol{\xi} = a_{\alpha}^{(1)} \quad (4.34b)$$

$$\frac{a_{\alpha\alpha}^{(2),\text{eq}} + \rho d}{2} = \int f^{\text{eq}} \frac{|\boldsymbol{\xi}|^2}{2} d^d \boldsymbol{\xi} = \rho E = \int f \frac{|\boldsymbol{\xi}|^2}{2} d^d \boldsymbol{\xi} = \frac{a_{\alpha\alpha}^{(2)} + \rho d}{2}. \quad (4.34c)$$

Thus we see that the coefficients of the Hermite series expansion of the equilibrium distribution are directly related to the macroscopic conserved quantities. Importantly, obtaining the correct macroscopic quantities of interest requires only 3 terms rather than evaluating the full function. Finally, we write

$$f^{\text{eq}}(\boldsymbol{\xi}) \approx \omega(\boldsymbol{\xi}) \sum_{i=0}^N \frac{1}{n!} \mathbf{a}^{(n),\text{eq}} \cdot \mathbf{H}^{(n)}(\boldsymbol{\xi}) \quad (4.35)$$

and

$$f(\boldsymbol{\xi}) \approx \omega(\boldsymbol{\xi}) \sum_{i=0}^N \frac{1}{n!} \mathbf{a}^{(n)} \cdot \mathbf{H}^{(n)}(\boldsymbol{\xi}) \quad (4.36)$$

where the \approx indicates that the series is truncated at N terms. Setting $N = 2$ gives for the equilibrium function

$$f^{\text{eq}}(\rho, \mathbf{u}, \theta, \boldsymbol{\xi}) \approx \omega(\boldsymbol{\xi}) \rho [1 + \xi_\alpha u_\alpha + (u_\alpha u_\beta + (\theta - 1) \delta_{\alpha\beta})(\xi_\alpha \xi_\beta - \delta_{\alpha\beta})] \quad (4.37)$$

$$= \omega(\boldsymbol{\xi}) \rho Q(\mathbf{u}, \theta, \boldsymbol{\xi}) \quad (4.38)$$

While we have obtained an appropriate series expansion for the equilibrium distribution function where the moments are related to the conserved macroscopic quantities, it is still not appropriately discretised. In this regard Hermite polynomials have a property that makes them ideal for discretisation - the existence of *abscissae*. The integral of the some polynomials can be calculated by simply calculating the integral at some discrete points x_i as

$$\int_{-\infty}^{\infty} \omega(\mathbf{x}) P^{(N)}(\mathbf{x}) d^d x = \sum_{i=1}^n w_i P^{(N)}(\mathbf{x}_i) \quad (4.39)$$

where $P^{(N)}$ is an N -th order polynomial and the n values of \mathbf{x}_i are roots of the n -th order 1D Hermite polynomial ($H^{(n)}(x_{i\alpha}) = 0$). This is called the Gauss-Hermite quadrature rule. Applying the Gauss-Hermite quadrature rule, it can be verified that after a little algebra, we obtain

$$a^{(n),\text{eq}} = \rho \int \omega(\boldsymbol{\xi}) \mathbf{R}(\boldsymbol{\xi}) d^d \boldsymbol{\xi} = \rho \sum_{i=1}^n w_i \mathbf{R}(\boldsymbol{\xi}_i) \quad (4.40)$$

where $\mathbf{R}(\boldsymbol{\xi}) = Q(\boldsymbol{\xi}) \mathbf{H}^{(n)}(\boldsymbol{\xi})$ is the polynomial to which the rule is applied. This lends a discretisation of the Hermite series expansion where n is the number of abscissae. Thus, instead of a continuous equilibrium function of the form shown in equation (4.37), we have n equilibrium functions of the form $f_i^{\text{eq}} = f^{\text{eq}}(\boldsymbol{\xi}_i)$ given by

$$f_i^{\text{eq}} = w_i \rho \left[1 + \xi_{i\alpha} u_\alpha + \frac{1}{2} (u_\alpha u_\beta + (\theta - 1) \delta_{\alpha\beta}) (\xi_{i\alpha} \xi_{i\beta} - \delta_{\alpha\beta}) \right] \quad (4.41)$$

whose first three moments satisfy the same conservation laws as the continuous equilibrium distribution function. Substituting $\mathbf{c}_i = \boldsymbol{\xi}_i / \sqrt{3}$ as the discrete velocities, the final discrete equilibrium function (see Appendix A.4. of [10] for more details) is given by

$$f_i^{\text{eq}} = w_i \rho \left(1 + \frac{c_{i\alpha} u_\alpha}{c_s^2} + \frac{u_\alpha u_\beta (c_{i\alpha} c_{i\beta} - c_s^2 \delta_{\alpha\beta})}{2c_s^4} \right) \quad (4.42)$$

where c_s is the speed of sound of the chosen velocity set which generally has the value $1/\sqrt{3}$.

Repeating the discretisation process for the distribution function f , the Hermite expansion coefficients are

$$(a)^{(n)}(\mathbf{x}, t) = \sum_{i=1}^q f_i(\mathbf{x}, t) \mathbf{H}^{(n)}(\mathbf{c}_i). \quad (4.43)$$

Finally, the (force-free) Boltzmann equation with discretised sets of velocity is given by

$$\frac{\partial f_i}{\partial t} + c_{i\alpha} \frac{\partial f_i}{\partial x_\alpha} = \Omega(f_i), \quad (4.44)$$

with the density and momentum given by

$$\rho = \sum_i f_i = \sum_i f_i^{\text{eq}}, \quad (4.45)$$

$$\rho \mathbf{u} = \sum_i f_i \mathbf{c}_i = \sum_i f_i^{\text{eq}} \mathbf{c}_i. \quad (4.46)$$

4.2.5 Discretisation of space and time

The Lattice Boltzmann algorithm involves populations of f_i at each point on a grid moving with velocity \mathbf{c}_i . After each time-step Δt , the population must reach a neighbouring grid point. Thus, the grid must be uniform with spacing Δx such that if a population starts at a grid point at \mathbf{x} , there must also be grid points at $\mathbf{x} + \mathbf{c}_i \Delta t$ for all the discrete velocities \mathbf{c}_i and any spatio-temporal discretisation of the Boltzmann equation must adhere to this constraint.

Consider the total derivation of f_i with respect to an arbitrary parameter ψ as

$$\frac{df_i}{d\psi} = \Omega_i(\mathbf{x}(\psi), t(\psi)) \frac{dt}{d\psi} = \left(\frac{\partial f_i}{\partial t} \right) \frac{dt}{d\psi} + \left(\frac{\partial f_i}{\partial x_\alpha} \right) \frac{dx_\alpha}{d\psi}. \quad (4.47)$$

Comparing with equation (4.44) imposes the condition

$$\frac{dt}{d\psi} = 1, \quad \frac{dx_\alpha}{d\psi} = c_{i\alpha}. \quad (4.48)$$

This is variable transformation $t \rightarrow \psi$ which serves the purpose of converting the Boltzmann equation, which is a partial differential equation, to an ordinary differential equation form. For a given point (\mathbf{x}_0, t_0) such that $t(\psi = 0) = t_0$ and $\mathbf{x}(\psi = 0) = \mathbf{x}_0$, integrating from $\psi = 0$ to $\psi = \Delta t$ gives

$$f_i(\mathbf{x}_0 + \mathbf{c}_i \Delta t, t_0 + \Delta t) - f_i(\mathbf{x}_0, t_0) = \int_0^{\Delta t} \Omega_i(\mathbf{x}_0 + \mathbf{c}_i \psi, t_0 + \psi) d\psi, \quad (4.49)$$

This can be generalised to any arbitrary point (\mathbf{x}, t) . The LHS is exact, but the RHS still needs to be estimated. To the first order in Δt , the simplest approximation of the integral can be made by simply considering the value of the integrand at a single point, also known as a rectangular discretisation, that is,

$$f_i(\mathbf{x} + \mathbf{c}_i \Delta t, t + \Delta t) - f_i(\mathbf{x}, t) = \Delta t \Omega_i(\mathbf{x}, t). \quad (4.50)$$

This simplest approximation is in fact the most widely used form of the **Lattice Boltzmann equation**, which forms the bedrock of the Lattice Boltzmann method to solve fluid equations. This still requires the specification of the form of the collision operator, such as the BGK collision operator already introduced.

The unique reason that the first order approximation suffices is that even a second order approximation, in the form of,

$$f_i(\mathbf{x}_0 + \mathbf{c}_i \Delta t, t_0 + \Delta t) - f_i(\mathbf{x}_0, t_0) = \Delta t \frac{\Omega_i(\mathbf{x}, t) + \Omega_i(\mathbf{x} + \mathbf{c}_i \Delta t, t + \Delta t)}{2}, \quad (4.51)$$

also returns the same expression. For example, with the BGK collision operator given by $\Omega_i = -(f_i - f_i^{\text{eq}})/\tau$, the above equation returns equation (4.49) with a redefined relaxation time $\tau \rightarrow \tau + \Delta t/2$ [52].

4.3 The Lattice Boltzmann Equation

Thus, given a form of the collision operator, we have the Lattice Boltzmann equation, given by

$$f_i(\mathbf{x} + \mathbf{c}_i \Delta t, t + \Delta t) = f_i(\mathbf{x}, t) - \frac{\Delta t}{\tau} (f_i(\mathbf{x}, t) - f_i^{\text{eq}}(\mathbf{x}, t)), \quad (4.52)$$

where the equilibrium population distribution is given by

$$f_i^{\text{eq}}(\mathbf{x}, t) = w_i \rho \left(1 + \frac{\mathbf{c}_i \cdot \mathbf{u}}{c_s^2} + \frac{(\mathbf{c}_i \cdot \mathbf{u})^2}{2c_s^4} - \frac{\mathbf{u} \cdot \mathbf{u}}{2c_s^2} \right). \quad (4.53)$$

This is a discretised version of the Boltzmann equation, with the discrete populations f_i describing the distribution function f of the kinetic theory of gases. The various moments of the populations are related to the density, momentum, energy, stress tensor, etc. The next step is to show that the Lattice Boltzmann equation solves the Navier-Stokes equation. This is shown via the Chapman-Enskog analysis, which is described in the following session.

4.3.1 Chapman-Enskog Analysis

We assume that the distribution function f_i is given by

$$f_i = f_i^{(0)} + \epsilon f_i^{(1)} + \epsilon^2 f_i^{(2)} + \dots \quad (4.54)$$

where the 0-th order term $f_i^{(0)}$ is nothing but the equilibrium distribution function f_i^{eq} . Here, ϵ is an appropriate positive scale parameter with $\epsilon \ll 1$. ϵ is usually identified to be of the same order as the Knudsen number Kn , given by

$$\text{Kn} = \frac{\ell_{\text{mfp}}}{\ell}, \quad (4.55)$$

where ℓ_{mfp} and ℓ are respectively the mean free path of the gas molecules and the characteristic length scale of the problem, already discussed in the introduction to the kinetic theory of gases. Problems in which the continuum approximation of the fluid and the Navier-Stokes equation are valid are characterised by $\text{Kn} \ll 1$.

Returning to the distribution function f , consider the Lattice Boltzmann equation

$$f_i(\mathbf{x} + \mathbf{c}_i \Delta t, t + \Delta t) - f_i(\mathbf{x}, t) = -\frac{\Delta t}{\tau} (f_i(\mathbf{x}, t) - f_i^{\text{eq}}(\mathbf{x}, t)). \quad (4.56)$$

Writing a Taylor expansion of the above leads to

$$\Delta t (\partial_t + c_{i\alpha} \partial_\alpha) f_i + \frac{(\Delta t)^2}{2} (\partial_t + c_{i\alpha} \partial_\alpha)^2 f_i + \mathcal{O}((\Delta t)^3) = -\frac{\Delta t}{\tau} f_i^{\text{neq}}, \quad (4.57)$$

with f_i^{neq} given by $f_i - f_i^{\text{eq}}$ retaining only the higher order terms of equation (4.54). Multiplying equation (4.57) with $(\delta t/2)(\partial_t + c_{i\alpha}\partial_\alpha)$ and subtracting it by itself leads to

$$\delta t(\partial_t + c_{i\alpha}\partial_\alpha)f_i = -\frac{\Delta t}{\tau}f_i^{\text{neq}} + \Delta t(\partial_t + c_{i\alpha}\partial_\alpha)\frac{\Delta t}{2\tau}f_i^{\text{neq}} \quad (4.58)$$

after neglecting the higher-order terms. Another ansatz is made where the time derivative is expanded as

$$\Delta t\partial_t f_i = \Delta t \left(\epsilon\partial_t^{(1)} f_i + \epsilon^2\partial_t^{(2)} f_i + \dots \right), \quad (4.59)$$

$$\Delta t c_{i\alpha}\partial_\alpha f_i = \Delta t \left(\epsilon c_{i\alpha}\partial_\alpha^{(1)} f_i \right). \quad (4.60)$$

Such an expansion of the time derivative is known as *multiple scale expansion*. Separating the terms of different orders, we get for terms of order $\mathcal{O}(\epsilon)$

$$\left(\partial_t^{(1)} + c_{i\alpha}\partial_\alpha^{(1)} \right) f_i^{\text{eq}} = -\frac{1}{\tau}f_i^{(1)}, \quad (4.61)$$

and for terms of order $\mathcal{O}(\epsilon^2)$ we obtain

$$\partial_t^{(2)} f_i^{\text{eq}} + \left(\partial_t^{(1)} + c_{i\alpha}\partial_\alpha^{(1)} \right) \left(1 - \frac{\Delta t}{2\tau} \right) f_i^{(1)} = -\frac{1}{\tau}f_i^{(2)}. \quad (4.62)$$

The moments of the $\mathcal{O}(\epsilon)$ equation gives

$$\partial_t^{(1)}\rho + \rho_\gamma^{(1)}(\rho u_\gamma) = 0, \quad (4.63a)$$

$$\partial_t^{(1)}(\rho u_\alpha) + \partial_\beta^{(1)}\Pi_{\alpha\beta}^{\text{eq}} = 0, \quad (4.63b)$$

$$\partial_t^{(1)}\Pi_{\alpha\beta}^{\text{eq}} + \partial_\gamma^{(1)}\Pi_{\alpha\beta\gamma}^{\text{eq}} = -\frac{1}{\tau}\Pi_{\alpha\beta}^{(1)} \quad (4.63c)$$

with the moments defined as

$$\Pi_{\alpha\beta}^{\text{eq}} = \sum_i c_{i\alpha}c_{i\beta}f_i^{\text{eq}} = \rho u_\alpha u_\beta + \rho c_s^2 \delta_{\alpha\beta}, \quad (4.64a)$$

$$\Pi_{\alpha\beta\gamma}^{\text{eq}} = \sum_i c_{i\alpha}c_{i\beta}c_{i\gamma}f_i^{\text{eq}} = \rho c_s^2 (u_\alpha \delta_{\beta\gamma} + u_\beta \delta_{\alpha\gamma} + u_\gamma \delta_{\alpha\beta}), \quad (4.64b)$$

$$\Pi_{\alpha\beta}^{(1)} = \sum_i c_{i\alpha}c_{i\beta}f_i^{(1)}. \quad (4.64c)$$

Thus, while the equilibrium moments given above are known, the third moment $\Pi_{\alpha\beta}^{(1)}$ is unknown. Now taking the moments of equation (4.60), we have

$$\partial_t^{(2)} \rho = 0, \quad (4.65a)$$

$$\partial_t^{(2)}(\rho u_\alpha) + \partial_\beta^{(1)} \left(1 - \frac{\Delta t}{2\tau} \right) \Pi_{\alpha\beta}^{(1)} = 0. \quad (4.65b)$$

Combining these equations gives finally

$$\left(\epsilon \partial_t^{(1)} + \epsilon^2 \partial_t^{(2)} \right) \rho + \epsilon \partial_\gamma^{(1)}(\rho u_\gamma) = 0, \quad (4.66a)$$

$$\left(\epsilon \partial_t^{(1)} + \epsilon^2 \partial_t^{(2)} \right) (\rho u_\alpha) + \epsilon \partial_\beta^{(1)} \Pi_{\alpha\beta}^{\text{eq}} = -\epsilon^2 \partial_\beta^{(1)} \left(1 - \frac{\Delta t}{2\tau} \right) \Pi_{\alpha\beta}^{(1)}. \quad (4.66b)$$

Using the isothermal equation of state $p = \rho c_s^2$, we obtain (see Appendix A.2.2. of [10])

$$\Pi_{\alpha\beta}^{(1)} = -\rho c_s^2 \tau \left(\partial_\beta^{(1)} u_\alpha + \partial_\alpha^{(1)} u_\beta \right) + \tau \partial_\gamma^{(1)}(\rho u_\alpha u_\beta u_\gamma). \quad (4.67)$$

Using equation (4.67) and plugging back the time derivatives into equations (4.66a) and (4.66b) and neglecting the $\mathcal{O}(u^3)$ term $\rho u_\alpha u_\beta u_\gamma$, we finally get the Navier-Stokes equations

$$\partial_t \rho + \partial_\gamma(\rho u_\gamma) = 0, \quad (4.68)$$

$$\partial_t(\rho u_\alpha) + \partial_\beta(\rho u_\alpha u_\beta) = -\partial_\alpha p + \partial_\beta [\eta(\partial_\beta u_\alpha + \partial_\alpha u_\beta)] \quad (4.69)$$

with the following relations -

$$p = \rho c_s^2, \quad \eta = \rho c_s^2 \left(\tau - \frac{\Delta t}{2} \right). \quad (4.70)$$

It is important to note that the equation of state is required to close the system of equations. While the incompressible Navier-Stokes equations are a closed system of equations, the Lattice Boltzmann equations solve the compressible Navier-Stokes equations and hence ρ is also an unknown. The Lattice Boltzmann equation is valid only in the limit of small Mach number where the Mach number Ma is given by

$$\text{Ma} = \frac{u}{c_s} \quad (4.71)$$

where u is the characteristic velocity of the system. In the limit of small Mach number $\text{Ma} \leq 0.1$, the fluid is said to be in the weakly compressible limit, where variations in ρ are small and the continuity equation can still be approximate to be of the form $\nabla \cdot \mathbf{u} = 0$. Thus, the Lattice Boltzmann equation is used to simulate incompressible fluids.

4.3.2 The Lattice Boltzmann Algorithm

We have already seen and derived from scratch the Lattice Boltzmann equation given by

$$f_i(\mathbf{x} + \mathbf{c}_i \Delta t, t + \Delta t) = f_i(\mathbf{x}, t) - \frac{\Delta t}{\tau} (f_i(\mathbf{x}, t) - f_i^{\text{eq}}(\mathbf{x}, t)). \quad (4.72)$$

This is implemented in two steps, known as *collision* and *streaming*. The collision step is a local algebraic step and is given by

$$f_i^*(\mathbf{x}, t) = f_i(\mathbf{x}, t) - \frac{\Delta t}{\tau} (f_i(\mathbf{x}, t) - f_i^{\text{eq}}(\mathbf{x}, t)). \quad (4.73)$$

Here, f_i^* is the value of the distribution function post-collision. The equilibrium distribution function can be calculated given the values of the macroscopic quantities, ρ and \mathbf{u} along with the set of velocity vectors. The next step is streaming, where the populations are transported to their respectively neighbouring lattice sets according to the lattice velocity vectors, that is,

$$f_i(\mathbf{x} + \mathbf{c}_i \Delta t, t + \Delta t) = f_i^*(\mathbf{x}, t). \quad (4.74)$$

Following the streaming step, the various moments of f are calculated to obtain the macroscopic hydrodynamic quantities. To recap, the density and the velocity are respectively calculated as

$$\rho(\mathbf{x}, t) = \sum_i f_i(\mathbf{x}, t), \quad \mathbf{u}(\mathbf{x}, t) = \frac{1}{\rho} \sum_i \mathbf{c}_i f_i(\mathbf{x}, t). \quad (4.75)$$

These are used to calculate the new equilibrium functions which in turn are used in the succeeding collision step. Note that this Lattice Boltzmann algorithm is valid only in the bulk. At the boundary, that is the edge of the lattice grid, the streaming step fails as the populations arriving from neighbouring sites in one direction are missing. Thus, appropriate boundary conditions have to be imposed which provide the missing populations to the boundary grid points.

4.4 Forcing in Lattice Boltzmann

In the presence of a force acting on a fluid, the Navier-Stokes equation is modified by adding a forcing-term \mathbf{F} to the momentum conservation equation. It can be shown by Chapman-Enskog analysis again that the Lattice Boltzmann equation is modified in turn by the addition of source-term as

$$f_i(\mathbf{x} + \mathbf{c}_i \Delta t, t + \Delta t) = f_i(\mathbf{x}, t) + (\Omega_i + S_i) \Delta t, \quad (4.76)$$

where $\Omega_i = -\frac{1}{\tau}(f_i - f_i^{\text{eq}})$ is the usual collision operator while the additional source term is given by

$$S_i = \left(1 - \frac{\Delta t}{2\tau}\right) w_i \left(\frac{c_{i\alpha}}{c_s^2} + \frac{(c_{i\alpha} c_{i\beta} - c_s^2 \delta_{\alpha\beta}) u_\beta}{c_s^4} \right) F_\alpha. \quad (4.77)$$

The form of the additional term for forcing was proposed by Guo et. al [53] and is thus known widely as the Guo-forcing scheme and it is among the most widely used forcing schemes in Lattice Boltzmann algorithms.

Defining $F_i = (1 - \frac{1}{2\tau})^{-1} S_i$, the moments are given by

$$\sum_i F_i = 0, \quad (4.78a)$$

$$\sum_i F_i c_{i\alpha} = F_\alpha, \quad (4.78b)$$

$$\sum_i F_i c_{i\alpha} c_{i\beta} = F_\alpha u_\beta + u_\alpha F_\beta. \quad (4.78c)$$

It can be shown by performing the Chapman-Enskog analysis again that the calculation of the velocity moment is modified by a correction factor given by

$$\mathbf{u} = \frac{1}{\rho} \sum_i f_i \mathbf{c}_i + \frac{\mathbf{F} \Delta t}{2\rho}. \quad (4.79)$$

The forcing term in fluids usually takes the form of a buoyancy force that is proportional to the gravitational acceleration \mathbf{g} .

4.5 Two Population Lattice Boltzmann for Advected Scalar

The advection-diffusion equation (ADE) for a scalar C has already been introduced in chapter 3.1 and is given by

$$\frac{\partial C}{\partial t} + (\mathbf{u} \cdot \nabla) C = D \nabla^2 C. \quad (4.80)$$

The ADE shares several similarities with the Navier-Stokes equation and thus the Lattice Boltzmann method can be easily adapted to solve problems of the transport of a scalar in a fluid. Introducing another set of population g_i which solve the Lattice Boltzmann equation [54]

$$g_i(\mathbf{x} + \mathbf{c}_i \Delta t, t + \Delta t) = g_i(\mathbf{x}, t) - \frac{\Delta t}{\tau_g} (g_i(\mathbf{x}, t) - g_i^{\text{eq}}(\mathbf{x}, t)), \quad (4.81)$$

solves the ADE for scalar concentration $C = \sum_i g_i$. The diffusivity D is given by

$$D = c_s^2 \left(\tau_g - \frac{\Delta t}{2} \right). \quad (4.82)$$

The equilibrium distribution g_i^{eq} is given by

$$g_i^{\text{eq}} = w_i C \left(1 + \frac{\mathbf{c}_i \cdot \mathbf{u}}{c_s^2} + \frac{(\mathbf{c}_i \cdot \mathbf{u})^2}{2c_s^4} - \frac{\mathbf{u} \cdot \mathbf{u}}{2c_s^2} \right). \quad (4.83)$$

The easy adaptability of the Lattice Boltzmann method to the ADE arises from the fact that the Navier-Stokes equation itself is of the form of an advection-diffusion equation for the momentum $\rho \mathbf{u}$. The equilibrium functions g_i^{eq} depends on the \mathbf{u} , thus the velocity is imposed externally. Once again, the link between the equation for g_i and the ADE is shown by a repeat of the Chapman-Enskog analysis

In several applications of the ADE, there is often an added *source term* Q on the RHS, which represents either release or absorption of the scalar. The form of the Lattice Boltzmann equation for the set of populations g_i is then modified as [55]

$$g_i(\mathbf{x} + \mathbf{c}_i \Delta t, t + \Delta t) = g_i(\mathbf{x}, t) - \frac{\Delta t}{\tau_g} (g_i(\mathbf{x}, t) - g_i^{\text{eq}}(\mathbf{x}, t)) + \left(1 - \frac{1}{2\tau_g} \right) w_i Q \quad (4.84)$$

The concentration of the scalar C is then obtained by the modified moment

$$C = \sum_i g_i + \left(1 - \frac{1}{2\tau_g} \right) Q. \quad (4.85)$$

Other methods to represent the scalar in the Lattice Boltzmann algorithm include using additional lattice velocities in the velocity, among others. The two-population method for simulating an advected scalar in a fluid has one crucial advantage over other methods - the choice of setting the fluid LB relaxation time τ and the advection LB relaxation time τ_g independently allows ν and D to be set independently of each other.

Chapter 5

Nudging applied to Turbulent Rayleigh-Bénard Convection

Summary First, the chapter motivates an understanding of data assimilation and in particular, the technique of nudging. Following this, the details of the study on nudging applied to Rayleigh-Bénard convection conducted as part of the thesis work are described fully. Nudging, a data assimilation technique is applied to the temperature field of Rayleigh-Bénard convection flows of varying degrees of turbulence (changing Rayleigh number). The equations of the model system are described along with an account of the various numerical experiments performed. It is assumed that partial temperature measurements from the Rayleigh-Bénard convection are available via some immersed passive probes. The quantity of information is varied by varying the number of probes and the efficacy of the nudging technique in reconstructing the flows are assessed as a function of the quantity of information. Local, global as well as scale-by-scale reconstruction errors are studied for the various cases. The results are analysed in terms of the complexity of the solution at various Rayleigh numbers. Finally, the conclusions and the physical insights gained from the study regarding the correlation between the velocity and temperature fields are listed as well as possible directions for future research to build upon the study.

5.1 Introduction to Data Assimilation

Several systems in nature can be described accurately and realistically by numerical models which can predict the behaviour of the system, provided the initial state of the system is well known. However, it is rare to obtain complete information about a given system at a given point of time. Further, both observations and models may contain errors, either due to intrinsic reasons and constraints (in case

of models) or due to disturbances and random errors (in case of observations).

Data Assimilation is a family of techniques to combine computational models along with observational data to produce an optimal *analysis*. An Analysis is a rendering or estimate of the true state of a system (usually the atmosphere) at a given time. Such an analysis is used to either study and understand the atmosphere itself, to test the accuracy of models or as an initial state to be fed into another model or system. An analysis is usually performed given only partial/sparse observational data, and data assimilation is the way to incorporate observations to improve the analysis.

It is important at this point to precisely define some terms that will be used in the rest of this chapter. The *Truth* is the true state of the system attained and consists of a set of numbers describing the system accurately. The *background* information consists of an a priori estimate of the system, usually obtained via numerical simulations using a realistic model. The background can also be a trivial state of the system or it could be the output of a previous model run. *Observations* are physical measurements of the system. These observations are often incomplete, with measurements conducted only of sparse regions in space, or only of a subset of the state variables. Often, observations of state variables are not available directly and instead must be estimated indirectly by measurements of other quantities. A prominent example of such a situation is the use of outgoing infrared radiation to measure the temperature of the atmosphere or a land surface. Thus, the directly observed quantity is the radiation, which provides an estimate of the state variable of temperature, for which the equations are known.

The concept of data assimilation is the following - for well-behaved systems with known dynamics and physical properties, the constraints imposed by the physical laws can be exploited so that observations are incorporated into the background (a priori model, usually numerical) to produce an improved, more accurate analysis. Thus, in pure modelling,

$$\text{Analysis} = \text{Background}$$

,

whereas in data assimilation,

$$\text{Analysis} = \text{Background} + \text{Observations}$$

.

Given an already existing background state vector \mathbf{x}_b which contains all the information of all the state variables such as velocity, pressure, temperature, density, humidity, etc., the problem of data assimilation is to find the right increment vector $\delta\mathbf{x}$ to obtain a more accurate analysis \mathbf{x}_a that is closer to the truth state vector \mathbf{x}_t .

$$\mathbf{x}_a = \mathbf{x}_b + \delta\mathbf{x}. \quad (5.1)$$

For this, the observations \mathbf{y} are used. To correctly estimate the errors with respect to the observations, an *observation operator* $\mathbf{H}(\mathbf{x})$ is needed which maps the model state to the observation space. That is to say, given a model state \mathbf{x} , the operator \mathbf{H} applied on this state gives the observation (or measurement) that would arise if the model state were the truth. If we assume an observation \mathbf{y} with no error, then $\mathbf{y} \neq \mathbf{H}(\mathbf{x})$ indicates that \mathbf{x} is not the true state and needs to be updated. The departure $\mathbf{y} - \mathbf{H}(\mathbf{x})$ can also be used as a measure of the efficacy of the data assimilation method.

5.2 The need for Data Assimilation

There are several reasons for observations to be incorporated into models. Most importantly, models simulating complex, chaotic systems rely on extremely accurate initial conditions. This initial condition can come from either observations or a previous model run - in which case finding an optimal way to combine the two leads to superior initial conditions for subsequent model runs. Further, as mentioned, observations tend to be sparse and they alone cannot provide a complete analysis - in this situation leveraging known physical laws to estimate the state of the system where observations are absent is crucial. If observations of all state variables are available everywhere, then analysis is reduced to mere interpolation.

Further, both models and observations are characterised by intrinsic errors. Observational errors can arise from instrumental errors or disturbances. Even if the observations are assumed to be perfect, model errors are inescapable due to the finite resolution of an numerical model of a system. These are known as *representativeness errors*.

5.3 Nudging

The simplest of the data assimilation techniques are the so-called Cressman analysis schemes [56]. Given a background state \mathbf{x}_b and a set of n finite observations $\mathbf{y}_i, i = 1 \dots n$, an update is performed at each grid point j according to

$$\mathbf{x}_a(j) = \mathbf{x}_b(j) + \frac{\sum_{i=1}^n w(i, j) [\mathbf{y}_i - \mathbf{x}_b(i)]}{\sum_{i=1}^n w(i, j)}, \quad (5.2)$$

where $w(i, j)$ is a weight function that is a decreasing function of the distance between the grid point j and the point i at which the measurement \mathbf{y}_i is made,

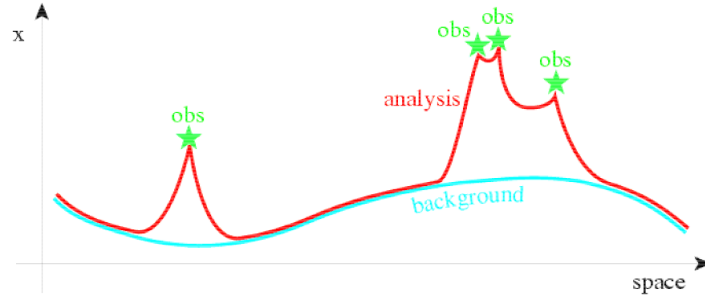


Figure 5.1: A schematic of the Cressman method applied to a state x . The light solid line represents the model output or background while the stars represent the observations. The analysis is obtained by applying a correction to the background in the vicinity of the observations. When observations are extremely sparse, the analysis deviates from the truth. Image taken from [17].

denoted $d_{i,j}$. It often also involves some cut-off distance R so that $w(i, j) = 0$ when $d_{i,j} > R$.

While the above analysis is performed at a single time step to apply one δx to the analysis, one can make use of continuous measurements which are sparse in space while working with a time evolution equation. This is a technique known as *nudging* where, in addition to the weighted data relaxation term related to the distance as above, there is also a factor $\alpha = 1/\tau$ multiplied which is a time relaxation factor. This enables to make use of a stream of data from fixed or moving points in space to be assimilated when the model equations are known.

Given a state variable a evolving according to the equation [57, 58]

$$\frac{da}{dt} = F(a; \lambda), \quad (5.3)$$

where λ are the various parameters of the system with initial condition $a(t_0) = a_0$. Given the measurements in space $y_i(t)$, first we define an *interpolation operator* $I_h(y_i(t))$ which appropriately interpolates the observational data in time and/or space. A *nudging term* is calculated similar to the term in the Cressman analysis scheme as the difference between the interpolated observational data and the dynamic model output. Thus, nudging involves applying of Cressman analysis like correction terms sequentially. For the system a , we define a new system b , called the *nudged system* or the *reconstructed system* which follows

$$\frac{db}{dt} = F(b; \lambda) - \alpha(b - I_h(y_i)), \quad (5.4)$$

with a different initial condition

$$b(t_0) = b_0. \quad (5.5)$$

Along with the initial conditions, the boundary conditions of the system a might differ from those of b as well. If one is interested solely in the bulk behaviour of a system far from the boundaries, this factor may not be important and can lead to a local synchronisation of a and b .

The weight term from equation (5.2) is absorbed in the function α , which sets the strength of the nudging, that is, the coupling between the model state variable and the observational values. α in general varies with space and time and has several features similar to the weights $w(i, j)$. It is also a decreasing function with increasing distance from the site of the observation and α too is often defined with a cut-off length to ensure that only points in the immediate vicinity of the observations are forced and $\alpha = 0$ at points far away from the points where observations are made. Setting the value and shape of α is non-trivial as when the observations are sparse and α is large, it may lead to overcorrection or force the system b to attain different values from the original system a when I_h is not designed correctly.

It is important to note the strength of the nudging method of data assimilation. It involves only the addition of a single forcing term, which can be made smooth by allowing α to be smooth. Further, at the points where observational data is not available, the reconstructed system still follows the same equations as the original system from which data is obtained. Thus, in the spirit of data assimilation, nudging leverages both, the knowledge about the physics and dynamics of the system as well as forcing the system to be as close as possible to the observational measurements wherever they are available.

The Cressman Analysis and nudging are examples of *sequential data assimilation* schemes, wherein observations are dynamically fed-back into the model wherever and whenever they are available to align the model output more closely with the observation. This does not take a global view of all the observations. Notice that if observations are not sparse and are available everywhere, the analysis reduces to merely an exercise of interpolation without any need for the background.

5.4 Introduction to the study

As we have already seen, thermal flows are of fundamental importance in several geophysical as well as industrial settings. They offer a rich variety of dynamical behaviours, pattern formation, transition to chaos and fully developed turbulence. The Rayleigh-Bénard convection is a model thermal flow already introduced and discussed in Chapter 3. In the rest of the chapter, a study is described wherein

only partial temperature measurements on turbulent Rayleigh-Bénard convection flows are used to reconstruct the original flow by the technique of nudging. Here, we directly apply the ideas of data assimilation to reconstruct a thermal flow given only sparse measurements on the most important state variable driving the flow - the temperature. The study is envisioned as a first step towards understanding the feasibility of applying data assimilation techniques on single state variables with completely missing data on other state variables, which are reconstructed indirectly via the model equations. This has already been done for the Rayleigh-Bénard convection using velocity data [59] as well as vorticity data [60], but to the best of our knowledge, nudging has not been applied only to the temperature field for a turbulent Rayleigh-Bénard convection.

5.5 Temperature-Velocity correlations in thermal flows

Despite their omnipresence, several facts about convective flows remain unsettled and continue to be areas of active research. For example, in the Rayleigh-Bénard convection, there is still considerable debate whether the turbulent flow shows the Bolgiano-Obukhov (BO59) scaling or shows only scaling compatible with the K41 theory. In the BO59 case, temperature is strongly active at all scales and kinetic energy cascades to the small scales via interactions with the thermal component, while in K41, kinetic energy is mainly injected by buoyancy in the bulk and transferred to high wavenumbers via the nonlinear Navier-Stokes terms. The interaction between large-scale thermal plumes and small-scale, intermittent turbulent fluctuations is also not entirely understood [2].

The Charney conjecture, first introduced by Charney in 1969 [58], states that temperature information alone is sufficient to know the entire state of the atmosphere. The conjecture was shown to be true in some simple systems, but has been found to be invalid for more complex, turbulent flows [61, 62]. In turbulent scenarios, correlations between temperature and velocity at the smaller scales are often not strong enough for the temperature to fully enslave the evolution of the velocity field. In recent years with greater and greater computational resources available to weather forecasters, with centres able to fully resolve the scales of three dimensional turbulence, this conjecture has started to gain more prominence. The general question of how much information on which fields or components allow reconstruction of the entire state of a system is central to Data Assimilation algorithms.

5.6 Partial Temperature Observations

The focus in this study is on turbulent 2D Rayleigh Bénard Convection where simulations are performed to understand the *quantity* of information as well as the *quality* of information on the temperature field that needs to be provided for an accurate reconstruction of the temperature field. Further, given a reconstruction of the temperature field, we also study the accuracy of the resulting reconstruction of the velocity field, which is reconstructed indirectly via the interaction and correlation between the temperature field and velocity field. We further study how this varies for varying Rayleigh number, that is, varying degrees of turbulence.

The study is thus a step towards understanding the feasibility of data assimilation techniques on real-world observational data when information on one or more state variables are missing. Our main result concerns the limit up to which the velocity field can be inferred from the temperature field. In particular, we show that there exist a *transition* for some characteristic Rayleigh number, $Ra \sim 10^7$ where the capability to construct the whole velocity configuration deteriorates suddenly.

5.7 Experimental set-up

We start with a two-dimensional Rayleigh-Bénard convection system under the Boussinesq approximation with velocity $\mathbf{u} = (u, v)$, temperature T , and pressure p with the equations taking the well-known form

$$\partial_t \mathbf{u} + (\mathbf{u} \cdot \nabla) \mathbf{u} = -\nabla p + \nu \nabla^2 \mathbf{u} - \beta T \mathbf{g}, \quad (5.6)$$

$$\frac{\partial T}{\partial t} + \mathbf{u} \cdot \nabla T = \kappa \nabla^2 T, \quad (5.7)$$

$$\nabla \cdot \mathbf{u} = 0, \quad (5.8)$$

where the average temperature of the fluid is set to zero and the density to unity. As usual, β is the thermal expansion coefficient of the fluid at temperature $T_0 = 0$, ν is the kinematic viscosity of the fluid, κ is the thermal conductivity of the fluid and \mathbf{g} is the acceleration due to gravity. The domain is a rectangle with horizontal and vertical length L_x and L_z , respectively, and is periodic in the horizontal x direction. The vertical temperature and velocity boundary conditions are given, respectively, by

$$\begin{aligned} T(z=0) &= T_d, & T(z=L_z) &= -T_d, \\ \mathbf{u}(z=0) &= \mathbf{u}(z=L_z) = 0. \end{aligned} \quad (5.9)$$

where T_d is positive. We also define the usual velocity scale $u_0 = \sqrt{|\mathbf{g}| L_z \beta \Delta T}$, where $\Delta T = 2T_d$ is the temperature difference between the top and bottom walls,

and a turnover time scale $\tau_0 = 2L_z/u_0$. Non-dimensionalising the equations with these scales yields the Rayleigh number Ra and the Prandtl number Pr as the two dimensionless numbers characterising the system and the Nusselt number defined in the usual way.

We also define the Kolmogorov length scale as $\eta_\kappa = (\nu^3/\epsilon)^{\frac{1}{4}}$, where $\epsilon = (\nu\kappa^2/L_z^4)\text{Ra}(\langle\text{Nu}\rangle - 1)$ is the average rate of energy dissipation already derived in Chapter 3.

We assume to have a set of passive probes at positions $\mathbf{X}^i(t)$, with $i = 1, \dots, N_p$, suspended in a *reference* Rayleigh-Bénard flow. The probes make periodic measurements of the fluid temperature $T^i(t) = T(\mathbf{X}^i(t), t)$ with constant sampling frequency $f = 1/\tau$ where τ is the time difference between two successive temperature measurements by the probes. We set f high enough so that a simple linear interpolation in time results in negligible errors and f is chosen as the smallest value so the sampling was smooth and faster than the fastest time scale of the system. This way additional complexities of errors arising from temporal interpolation are avoided and we can assume to know $T^i(t)$ associated with each particle at every time-step. The probes considered are of two types. Eulerian probes have their locations $\mathbf{X}^i(t)$ kept fixed in the laboratory reference frame. Lagrangian probes do not remain fixed in time but follow trajectories of tracer particles in the reference flow instead.

As already detailed above, the idea behind nudging is to run a new system where the evolution of the flow is steered onto the path set by the data. This new flow is known as the *nudged* or the *reconstructed* flow. A *nudging field* $T_n(\mathbf{r}, t)$ is constructed using the measurements $T^i(t)$ and another Rayleigh-Bénard system is run, denoted by velocity $\mathbf{U} = (U, V)$ and temperature \mathcal{T} , where an extra *heat source* term $-\alpha(\mathcal{T} - T_n)$ is added to the evolution equation for \mathcal{T} . This term penalizes the nudged temperature when it deviates from the reference values - if the temperature is higher (lower) than the nudging field, you locally absorb (release) heat. For each probe, a nudging square S_i is defined with centre at \mathbf{X}^i and fixed side length χ typically chosen of the same order as η_κ , (see also Table 5.2) and we nudge only in regions belonging to the sub-domain $\mathcal{S} := \cup_{i=1}^{N_p} S_i$, thus ensuring that nudging is applied only locally near the measurement probes while the regions in between the probes are left to simply evolve according to the dynamic equations. We do this by defining α as

$$\alpha(\mathbf{r}, t) = \begin{cases} \alpha_0, & \text{for } \mathbf{r} \in \mathcal{S}, \\ 0, & \text{otherwise,} \end{cases} \quad (5.10)$$

and the nudging field is defined as

$$T_n(\mathbf{r}, t) = T^i(t), \quad \text{for } \mathbf{r} \in S_i, \quad (5.11)$$

that is, the measured temperature $T^i(t) = T(\mathbf{X}^i(t), t)$ is set as the nudging temperature uniformly in a square of length χ centred at the probe-location.

The full equations for the nudged fields read

$$\nabla \cdot \mathbf{u} = 0, \quad (5.12)$$

$$\partial_t \mathbf{u} + (\mathbf{u} \cdot \nabla) \mathbf{u} = -\nabla \mathcal{P} + \nu \nabla^2 \mathbf{u} - \beta \mathcal{T} \mathbf{g}, \quad (5.13)$$

$$\frac{\partial \mathcal{T}}{\partial t} + \mathbf{u} \cdot \nabla \mathcal{T} = \kappa \nabla^2 \mathcal{T} - \alpha (\mathcal{T} - T_n), \quad (5.14)$$

where $\alpha(\mathbf{r}, t)$ sets the strength of the coupling between the reconstructed flow and the nudging field and has dimension $1/t$. It is very important to stress that the only energy input into the nudged system is via the nudging field, i.e. we impose adiabatic boundary conditions at the top and bottom walls.

$$\partial_z \mathcal{T}|_{z=0} = \partial_z \mathcal{T}|_{z=L_z} = 0. \quad (5.15)$$

In other words, the basic line for the reconstruction has no prior - if $T_n = 0$, the flow is zero everywhere. Since the Rayleigh number of the Rayleigh-Bénard convection is set by the temperature boundaries, it is likely that sampling preferentially from near the walls near the thermal boundary would result in the most accurate reconstruction. However, in the interest of a fair assessment of the nudging protocol, we consider only temperature probes on a uniform array without supposing we know anything about the nature of the thermal boundary. As a result the only information about the Ra available is that which is encoded in the probe measurements.

The spatial density of the probes is quantified by a characteristic wavenumber k_l given by

$$k_l = \frac{\Delta r}{l}, \quad (5.16)$$

where $\Delta r = 1$ is the grid-spacing in the Lattice Boltzmann algorithm to evolve the flow and l is the typical distance between the nearest probes. As the number of probes increases, l decreases and k_l increases as $k_l \sim \sqrt{N_p}$. The case of $k_l = 1$ corresponds to the situation where we have complete information, since there are probes located at every grid-point.

Fig. 5.2 shows the temperature snapshot of a temperature field as well as the nudging fields $T_n(\mathbf{r}, t)$ constructed from this field for three different values of k_l . From the figures, it is clear that for $k_l \gtrsim 0.1$ the density of point measurements should be enough to be able to accurately interpolate the temperature field while for $k_l \lesssim 0.03$ or smaller, the input information is rather limited. The problem then is two-fold — to understand how much information about the temperature field is needed to reconstruct it to a given degree of accuracy and to investigate the extent up to which the velocity field can be reconstructed from temperature data.

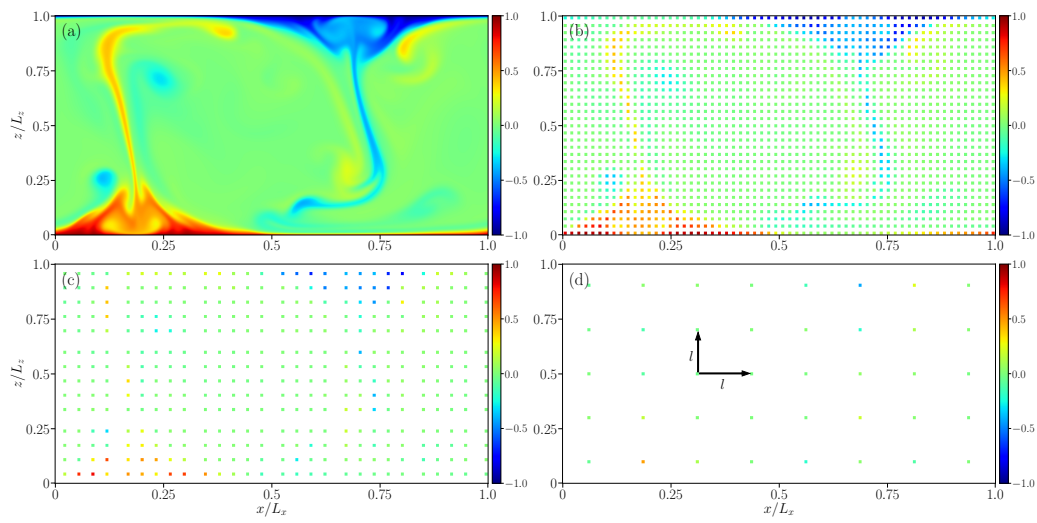


Figure 5.2: Snapshots of the temperature fields for the reconstruction experiments for flow with $\text{Ra} = 7.2 \times 10^7$. Panel (a) shows the ground-truth while (b), (c), and (d) show the constructed nudging field $T_n(\mathbf{r}, t)$ with $k_l = 1/14$, $k_l = 1/31$ and $1/97$, respectively. The temperatures are normalised to range between -1 (blue) and $+1$ (red) by dividing by T_d . The individual squares here correspond to the nudging squares S_i with side length $\chi = 6$. The typical length l between the probes is shown in panel (d).

Reference Flows		
Ra	7.206×10^7	36.27×10^7
Pr	1.0	1.0
Grid	864×432	1200×600
ν	6.67×10^{-4}	6.67×10^{-4}
Re	2091	6092
$\langle \text{Nu} \rangle$	24.835	38.802
η_κ	2.12	1.75
T_d	0.025	0.015
f	164	1130

Table 5.1: The parameters used for the reference flows. Frequency of sampling f is in units of probes measurements per turnover time τ_0 while all other parameters are in simulation units. Re is defined as $\text{Re} = u_{\text{rms}} L_z / \nu$ where u_{rms} is the root mean square velocity of the flow.

5.8 Numerical Experiments

Equations (5.6) - (5.8) are evolved using the Lattice-Boltzmann method until the average kinetic energy of the flow becomes statistically stationary. Once this stationary state is reached, the N_p passive probes are initialised in the domain on a uniform and equally spaced grid and the data from the probes, that is the fluid temperatures $T^i(t)$ at $\mathbf{X}^i(t)$, is obtained for ~ 250 turn-over times τ_0 . We consider the results first for the Eulerian probes. The results from the Lagrangian probes do not vary greatly from the Eulerian case and a brief overview is provided later.

This measured data by the probes is used to construct the nudging field T_n as detailed earlier. The flows studied have $\text{Pr} = 1$ and Ra between 10^7 - 10^9 , which is the well-known transition to turbulence regime in Rayleigh-Bénard convection. Two flows in particular, one with a moderate value of $\text{Ra} = 7.2 \times 10^7$ and a second one with a higher value of $\text{Ra} = 36.3 \times 10^7$ (see Table. 5.1) are studied and presented in more detail.

We define two important spectral quantities to understand the small-scale structure of the flow better. First, the time-averaged spectrum (all spectra in this study are measured only in the horizontal direction in a narrow band about the line $z = z_0 = L_z/2$) of the velocity field \mathbf{u} , or the kinetic energy spectrum, given by

$$E_{\mathbf{u}}(k_x) = \frac{1}{2} \langle |\hat{\mathbf{u}}(k_x, z_0, t)|^2 \rangle_t, \quad (5.17)$$

where $\hat{\mathbf{u}}(k_x, z_0, t)$ are the Fourier coefficients of the field \mathbf{u} and $\langle \cdot \rangle_t$ denotes the

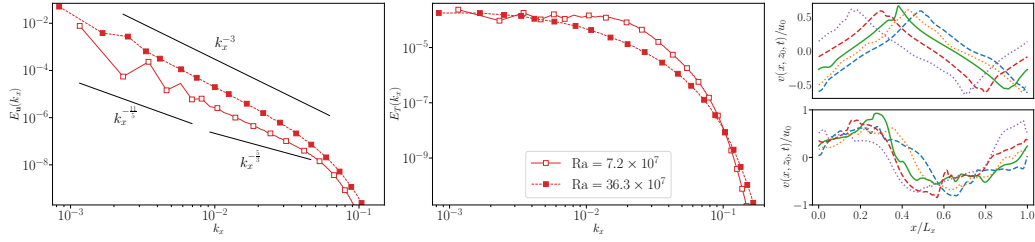


Figure 5.3: (a) E_u and (b) E_T for the two reference flows. Panel (c) shows $v(x, z_0, t)$ at various times during the run for the lower Ra reference flow with $\text{Ra} = 7.2 \times 10^7$ where each curve represents a particular instant of time. Panel (d) shows the same for the higher Ra reference flow with $\text{Ra} = 36.3 \times 10^7$.

time averaging. Similarly, the spectrum of the temperature field is defined as

$$E_T(k_x) = \left\langle |\hat{T}(k_x, z_0, t)|^2 \right\rangle_t, \quad (5.18)$$

where $\hat{T}(k_x, z_0, t)$ are the Fourier coefficients of the field T .

The magnitude of the problem is made clear by looking at the reference flow characteristics shown in Figure 5.3 E_u , E_T and instantaneous horizontal cuts of the vertical velocity at $z = z_0$, that is, $v(x, z_0, t)$, are shown for both reference flows. Panel (b) shows the spectrum of the temperature field becomes steeper when increasing Rayleigh number, indicating the presence of less well defined temperature plumes when turbulence increases. The slope of the temperature spectrum for the moderate Ra case shows that the temperature field is better correlated over a broader range of scales compared to the higher Ra flow. The energy spectra for both flows are close to a power law as shown in panel (a). On closer inspection, one can see that the spectrum for the lower Ra flow is indeed flatter much like the temperature spectrum. A large contrast can also be seen in the energy contained in the first few Fourier modes, where for the lower Ra flow, the first mode contains far greater energy compared to the successive modes. In the higher Ra flow, the first mode is still the most energetic, but the successive modes still contain a significant amount of energy. This contrast is borne out more clearly in the horizontal cuts of the vertical velocity for both the flow. In the lower Ra flow (panel (c)), even the instantaneous velocity field is smooth and highly structured with a regular, large-scale pattern with only small fluctuations whereas for the higher Ra flow (panel (d)), the velocity field in the bulk is far more chaotic and rugged, with a large-scale flow pattern not immediately discernible.

Once T_n is obtained, another flow is initialised with velocity $\mathbf{u}(\mathbf{r}, t) = 0$ and temperature $\mathcal{T}(\mathbf{r}, t) = 0$ everywhere and evolved according to equations (5.12) – (5.14). As already described, the thermal boundary conditions at the top and bottom walls are set to a no-thermal flux boundary condition so that the only

Reconstructions							
$\text{Ra} = 7.206 \times 10^7$				$\text{Ra} = 36.27 \times 10^7$			
N_p	k_l	χ	α_0	N_p	k_l	χ	α_0
3.7×10^5	1	-	0.01	7.2×10^5	1	-	0.01
7688	1/7	6	0.01	14792	1/7	6	0.08
3872	1/10	6	0.01	7442	1/10	6	0.08
1922	1/14	6	0.01	3698	1/14	6	0.08
800	1/22	6	0.01	1485	1/22	6	0.08
392	1/31	6	0.01	735	1/31	6	0.08
162	1/48	6	0.01	300	1/49	6	0.08
81	1/68	6	0.01	150	1/69	6	0.08
40	1/97	6	0.01	72	1/100	6	0.08
-	-	-	-	36	1/141	6	0.08

Table 5.2: The parameters used for the reconstructed (nudged) flows in simulation units.

energy inputs into the nudged system arise from the nudging term. The case of $k_l = 1$ is a special case scenario where it is assumed that the temperature data is available on every point at every time-step. In this case we use the fixed temperature boundary conditions of the Rayleigh-Bénard equations and we set $T_n(\mathbf{r}, t) = T(\mathbf{r}, t)$ everywhere.

The nudged simulations are evolved until they attain a statistically stationary kinetic energy. All measurements and further analysis are made in this stationary state. Identically to the spectra already defined for the reference flows (eqns. (5.17) - (5.18)), we define the kinetic energy spectra $E_{\mathcal{U}}$ and the thermal energy spectra $E_{\mathcal{T}}$ for the nudged simulations as well.

Corresponding to each reference flow, several nudging experiments are performed by varying k_l , α_0 and χ (see Table 5.1). Henceforth, we focus only on the effects of varying k_l and how these are affected by varying the Rayleigh number of the reference flow. The effects of varying χ and α_0 are discussed later.

5.9 Error quantification

To compare the reconstructed configurations from the nudging experiments with the ground-truth, we use various measures to quantify the efficacy of the nudging technique applied here. First, we define a point-wise error for temperature and

vertical velocity given by

$$T_\Delta(\mathbf{r}, t) = \mathcal{T}(\mathbf{r}, t) - T(\mathbf{r}, t), \quad (5.19)$$

and

$$v_\Delta(\mathbf{r}, t) = \mathcal{V}(\mathbf{r}, t) - v(\mathbf{r}, t). \quad (5.20)$$

Next, we define the global L2-error on the temperature and vertical velocity respectively given by

$$\Delta_T = \frac{\langle T_\Delta^2(\mathbf{r}, t) \rangle}{\langle T^2(\mathbf{r}, t) \rangle}, \quad (5.21)$$

and

$$\Delta_v = \frac{\langle v_\Delta^2(\mathbf{r}, t) \rangle}{\langle v^2(\mathbf{r}, t) \rangle}, \quad (5.22)$$

where $\langle \cdot \rangle$ indicates the average over the entire domain and the entire (stationary) run-time. We note that perfect synchronisation would lead to a value of $\Delta \sim 0$ while if the reconstructed flow is statistically correct but uncorrelated with the ground truth, we would have $\Delta \sim 2$. Δ_T for the reconstructed flows is compared with a ‘‘Baseline Reconstruction’’ where we calculate Δ_T by assuming $\mathcal{T}(\mathbf{r}, t) = T_n(\mathbf{r}, t)$ for $\mathbf{r} \in S$, and setting uniformly $\Delta_T = 1$ otherwise - that is setting the temperature uniformly identical to the nudged field where the flow is nudged and equal to the mean temperature, $\mathcal{T}(\mathbf{r}, t) = 0$, every where else.

To visualise the local errors at each instant, we also define an instantaneous L2-error on the temperature and vertical velocity given by

$$\delta_T(\mathbf{r}, t) = \frac{T_\Delta^2(\mathbf{r}, t)}{\langle T^2(\mathbf{r}, t) \rangle_{x,t}}, \quad (5.23)$$

$$\delta_v(\mathbf{r}, t) = \frac{v_\Delta^2(\mathbf{r}, t)}{\langle v^2(\mathbf{r}, t) \rangle_{x,t}} \quad (5.24)$$

respectively where $\langle \cdot \rangle_{x,t}$ indicates the time and spatial averages at a given height z .

For a comparison of the scale-by-scale reconstruction, we also define the spectrum of the errors of temperature and vertical velocity respectively given by

$$E_T^\Delta(k_x) = \left\langle |\hat{T}_\Delta(k_x, z_0, t)|^2 \right\rangle_t, \quad (5.25)$$

and

$$E_v^\Delta(k_x) = \left\langle |\hat{v}_\Delta(k_x, z_0, t)|^2 \right\rangle_t, \quad (5.26)$$

where $\hat{T}_\Delta(k, t)$ and $\hat{v}_\Delta(k, t)$ are respectively the fourier coefficients of the fields T_Δ and v_Δ .

5.10 Results

5.10.1 Visualising the fields and errors

We start by showing visualizations of the reference temperature field T , the nudged temperature field \mathcal{T} and the temperature error field δ_T at one given instant for both the flows in Fig. 5.4 and likewise for v , \mathcal{V} and δ_v in Fig. 5.5. Further, the vertical time-averaged profile of the errors, that is $\langle \delta_T \rangle_{x,t}$ and $\langle \delta_v \rangle_{x,t}$ are also overlaid on the snapshots of the instantaneous errors (right-most panels, solid yellow line). The nudged fields correspond to a case with $k_l = 1/14$, i.e., a high density of probes as seen in Fig. 5.2(b). Both reference flows are characterised by a rising hot plume and a falling cold plume and two large-scale counter-rotating vortices. The visualisations show clearly that the higher Ra flow (bottom row) shows an abundance of fine-scale structure and further, the plumes are poorly-defined, in contrast to the moderate Ra flow, where while the flow is not completely laminar, the plumes are clearly demarcated. The nudging protocol is able to accurately reconstruct the temperature field, even at higher Rayleigh number. In this case the maximum error is of the order of 10% and is concentrated on the plume and vortex structures while the thermal boundary layers show larger errors as clear from the average profile. This profile for the moderate Ra case is smooth and the value of the error doesn't change very sharply depending on whether the particular region is nudged or not (that is, whether $r \in S$ or not). In contrast, in the reconstruction of the higher Ra flow, the profile of the error shows highly oscillatory behaviour, indicating that while errors are lower in the nudged regions, they are relatively higher even in adjoining regions which are not nudged. This is a manifestation of the ruggedness of the temperature field when the flow is more turbulent. This is an indication that the low magnitude of error is solely due to the high density of probes in the system and not due to a complete synchronization of the reconstruction with the reference flows. Closer inspection of this averaged profile (yellow curves) near the top and bottom walls for both the flows shows that the error reaches the highest value close to the thermal boundaries. The large error near the thermal boundary is due to the relatively small thickness of the thermal boundary layer and the steep temperature gradient away from the wall. It is clear that to capture the precise behaviour of the temperature near the boundary walls needs a higher density of probes immersed near the walls.

The situation is different for the velocity field, which is reconstructed indirectly through the thermal forcing and depends on the response of the velocity field to the temperature field. It is seen from the reference velocity fields (Panels (a) and (d) in Fig. 5.5), the regions with rising fluid (red) and falling fluid (blue) are more clearly delineated in the lower Ra flow unlike in the higher Ra flow. The nudged field is in good agreement with the truth for the lower Rayleigh number

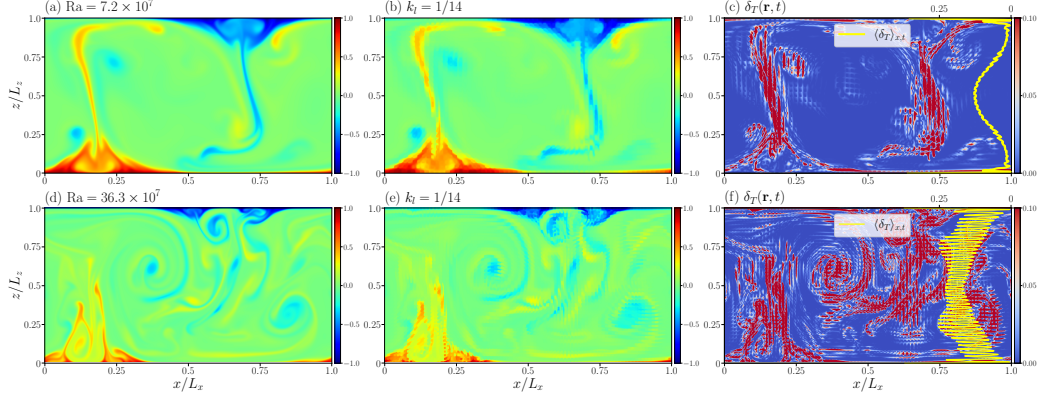


Figure 5.4: Snapshots of the (a) normalised ground truth field T/T_d for $Ra = 7.2 \times 10^7$, (b) the normalised reconstructed temperature field, \mathcal{T}/T_d for $k_l = 1/14$ corresponding to a distance between probes $l \sim 7\eta_\kappa$ and (c) the error, $\delta_T(\mathbf{r}, t)$ at a given instant of time. The yellow curve in panel (c) shows the time-averaged vertical profile of δ_T with the scale shown on the top right. The lower panels show the same quantities for the higher Ra flow with $Ra = 36.3 \times 10^7$.

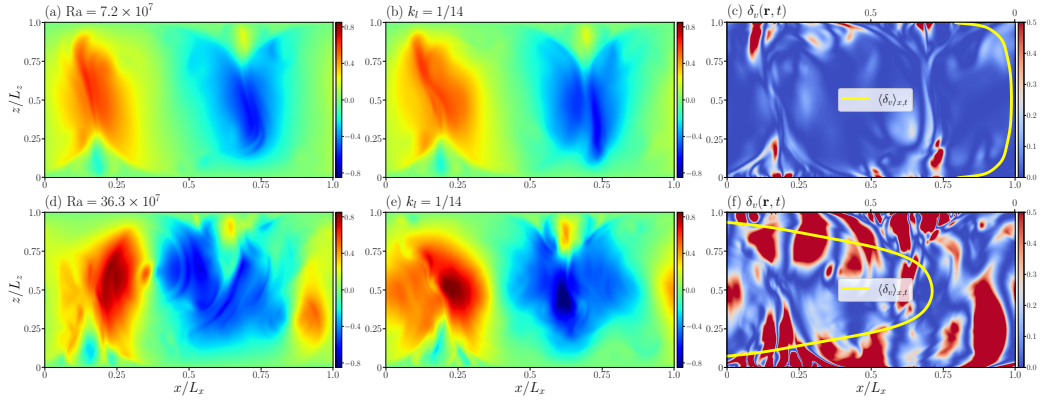


Figure 5.5: Snapshots of the (a) normalised ground truth field v/u_0 for $Ra = 7.2 \times 10^7$, (b) the normalised reconstructed field, \mathcal{V}/u_0 for $k_l = 1/14$ and (c) the error, $\delta_v(\mathbf{r}, t)$ at a given instant of time. The yellow curve in panel (c) shows the time-averaged vertical profile of δ_v with scale shown on the top right. The lower panels show the same quantities for the higher Ra flow with $Ra = 36.3 \times 10^7$.

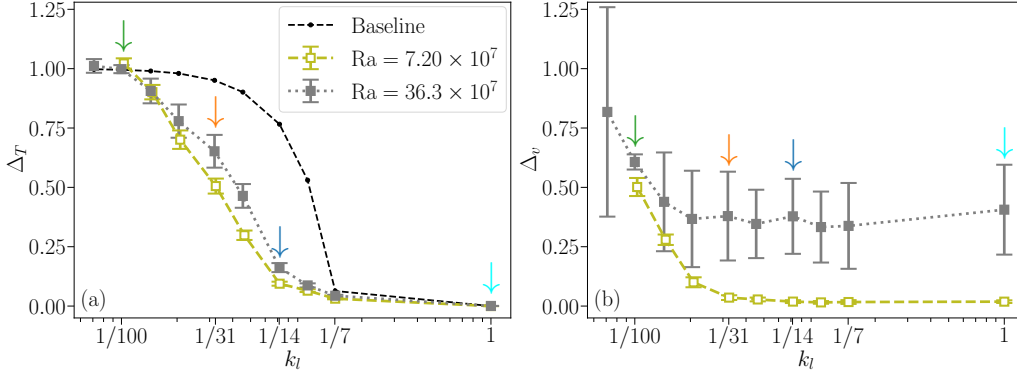


Figure 5.6: The global reconstruction errors (a) Δ_T , and (b) Δ_v for reconstructions of the two reference flows are varying k_l . Also shown is the baseline reconstruction error (black) for the higher Ra flow. The arrows indicate the value of k_l presented in detail in this study and whose corresponding nudging fields T_n for the moderate Ra case are shown in Figure 5.2.

case (top row) while large systematic errors on the whole volume develop for the higher Ra flow (bottom row) where the reconstructed velocity fails to capture the precise instantaneous shape of the reference while still broadly capturing the regions of rising and falling fluid accurately. The average profile of the errors for both cases are smooth. The invisibility of the nudging squares to the velocity field is a clear indication that the velocity field is not set locally by the local temperature but rather by the large-scale interplay between the temperature and velocity field. The reconstruction of the vertical velocity is most accurate in the bulk. Notice that due to the no-slip boundary condition ($\mathbf{u} = 0$) imposed at the top and bottom walls for the reference as well as reconstructed flows, the particular form of L2-error chosen here ceases to be well-defined at the vertical boundaries.

5.10.2 Global Errors

In Fig. 5.6 is shown the main quantitative summary of the study, where Δ_T and Δ_v are plotted as a function of k_l for the reconstructions of both flows. As seen in panel (a), the reconstruction error for temperature decreases when increasing the number of probes. A transition to synchronization-to-data can be seen at $k_l \sim 1/14$, corresponding to a typical wavenumber $k_x \sim 0.036$ or $1/28$ in Fig. 5.3. Equivalently, this corresponds to providing information at a separation of $\sim 7\eta_\kappa$ for the moderate Ra flow and $\sim 8\eta_\kappa$ for the higher Ra flow. The transition to *perfect* synchronization of the temperature fields occurs at similar scales in the two flows studied, and is similar to that observed in homogeneous and isotropic flows [63, 64]. The baseline reconstruction error approaches 0 for $k_l = 1/7$, the

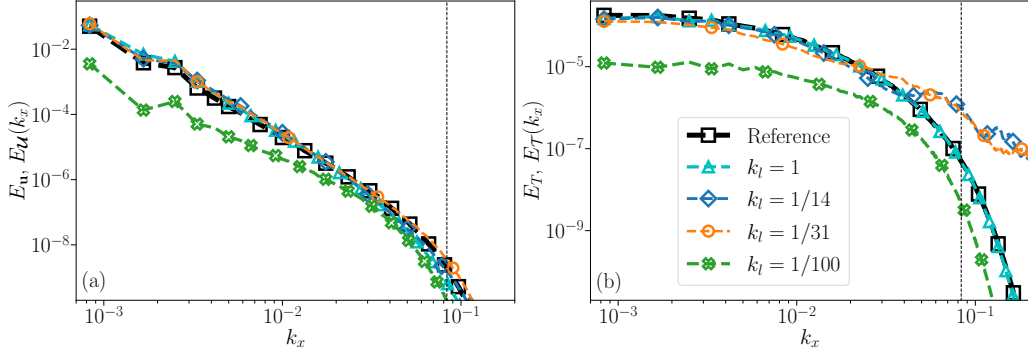


Figure 5.7: Energy and temperature spectra for the higher Ra reference flow with $Ra = 36.3 \times 10^7$ and the reconstructions at various k_l - (a) $E_u(k_x)$ (black) and $E_U(k_x)$. (b) $E_T(k_x)$ (black) and $E_T(k_x)$. The dotted vertical line shows the wavenumber corresponding to the length χ of the nudging squares.

scale at which for the chosen χ , the nudging squares cover the entire domain and thus, the baseline error includes only the small-scale temperature errors introduced by the application of a constant nudging temperature within each nudging square. Setting χ to be larger would cause these small-scale errors to be far larger while setting χ too small would lead to a reconstructed flow with significantly smaller kinetic energy and increase the effective distance between the probes, thus leading to larger global errors.

As for the reconstruction of the velocity field shown in panel (b), while the velocity field can be accurately reconstructed in the lower Rayleigh number case, the higher Rayleigh number case does not synchronize even for full information on the temperature ($k_l = 1$), showing a plateau at close to 40% for the average minimum error committed, the plateau being reached already at $k_l = 1/48$. The result is not completely surprising, indicating that for high Rayleigh number the *slaving* of the velocity field is less and less effective, and the imposition of more and more information on the forcing field (here the temperature) is not sufficient to recover full synchronization when turbulence is intense enough.

5.10.3 Scale-by-scale spectral properties and spectral errors

Figure 5.7 shows the statistical reconstruction of the flow properties by plotting the spectra for the reconstructed higher Ra flows - E_U and E_T - the same quantities as shown in the first two panels of Fig. (5.3) - for various k_l along with the ground truth in black. Panel (a) shows that the nudging experiments retrieve a flow with a velocity field with similar dynamic properties as the reference at all scales. In panel (b) showing the spectrum of the thermal energy, as expected the case with

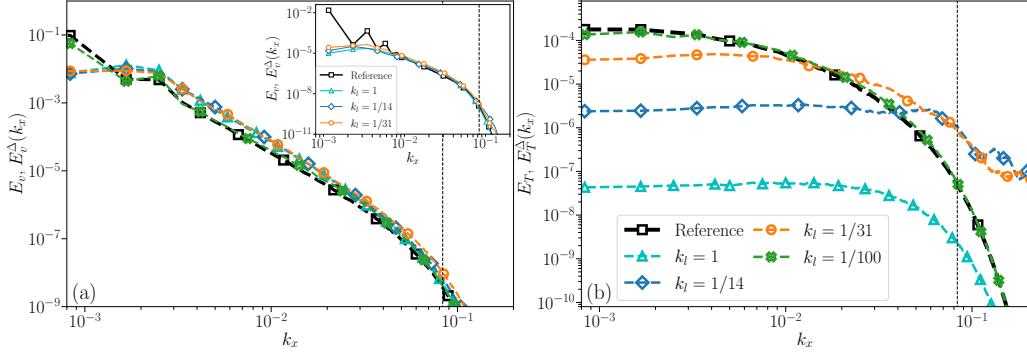


Figure 5.8: The spectra of the errors (a) E_v^Δ and (b) E_T^Δ for various k_l for reconstructions of the higher Ra flow with $Ra = 36.3 \times 10^7$. For comparison, the reference spectra (a) E_v and (b) E_T are also shown (black squares). The inset in panel (a) shows E_v for the moderate Ra reference flow with $Ra = 7.2 \times 10^7$ and E_v^Δ for the corresponding nudging experiments. The dotted vertical line shows the wavenumber corresponding to the length χ of the nudging squares.

$k_l = 1$ follows the ground truth exactly while the case with $k_l = 1/14$ captures the correct large-scale dynamics and at the same time introduces spurious correlations at smaller scales. This is due to the finite sizes of the nudging squares within which the nudging temperature is imposed uniformly, leading to systematic errors of small magnitudes for points close to X^i .

Further insight into the scale-wise behaviour is provided in Fig. 5.8, which shows the error spectra E_v^Δ and E_T^Δ and the corresponding reference spectra E_T and E_v . The scale-wise relative error can be gauged by the vertical displacement between the reference spectrum (black) and the reconstructed spectra. In panel (b) the error spectrum is nearly flat at large-scales with a value strongly dependent on k_l while E_T falls off gradually, indicating an increasing relative error for increasing k_x with the lowest relative errors at the largest scales. For larger k_x (smaller length-scales) we see a clear manifestation of the errors introduced by the finite nudging squares for $k_l = 1/14$ and $k_l = 1/31$. The error-spectrum for $k_l = 1/100$ is identical to the temperature spectrum of the ground truth, a result of the fact that the probes are extremely sparse and hence the reconstructed temperature field is nearly 0 everywhere. The black curve in panel (a) is the spectrum of the vertical velocity $E_v(k_x)$. The relative error is smallest at the largest scale and at smaller scales (larger k_x), we see that the error spectra and reference spectrum decay almost identically and hence shows a nearly constant relative error. It is in this aspect that we see the greatest contrast between the two Ra flows. The inset shows that reconstructions of the moderate Ra flow has far smaller relative error at the largest scales and this even persists for larger values of k_x . The small-scale

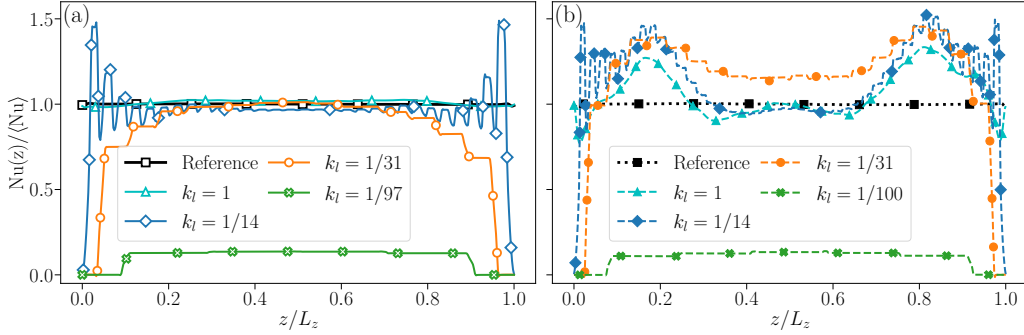


Figure 5.9: Profile of the Nusselt number for the ground truth and the reconstructions of the reference flow for (a) moderate Ra flow with $Ra = 7.2 \times 10^7$ and (b) higher Ra flow with $Ra = 36.3 \times 10^7$. The reference Nusselt number $Nu(z)$ and the reconstructed Nusselt number $Nu(z)$ are divided by the corresponding reference Nusselt number $\langle Nu \rangle$ with magnitude (a) $\langle Nu \rangle = 24.835$ and (b) $\langle Nu \rangle = 38.802$ respectively.

behaviour is similar to what is observed for the higher Ra case in the main panel.

Another important point to note is that the value of the error spectrum E_v^Δ shows little dependence on k_l and that the only scales of the velocity field that truly synchronize are the largest ones. The largest scale structure present are the hot and cold thermal plumes, which are captured correctly by the reconstruction. When the degree of turbulence is lower, there is a relative absence of fine-scale structures in the flow and most of the energy is contained in the large-scale alone - this large-scale synchronisation persists at some mid-range and smaller scales as well. For more turbulent flows where the plumes are less well-defined and the velocity field is more rugged, the synchronisation at the largest scales exists but to a smaller degree and it does not persist at smaller scales. This leads eventually to a much larger global error. These observations are explored in further detail below.

5.10.4 Inferring Nusselt Number

The Nusselt number defined in equation (1.8) measures the heat transfer due to convection relative to that due to conduction in the Rayleigh-Bénard system. Similarly, for the reconstructed flows we define the Nusselt number as

$$Nu(z) = \frac{\mathcal{V}\mathcal{T} - \kappa\partial_z\mathcal{T}}{\frac{\kappa\Delta T}{L_z}}, \quad (5.27)$$

where ΔT is the temperature difference between the horizontal walls for the corresponding reference flow. As already noticed, given only a set of temperature

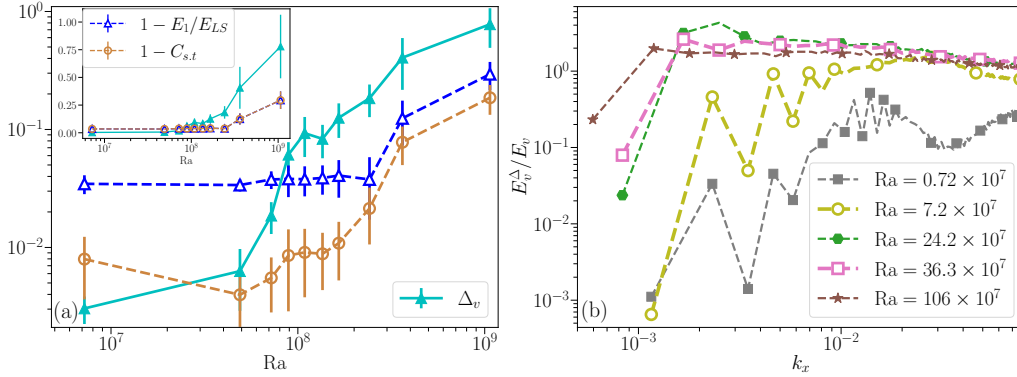


Figure 5.10: (a) Δ_v for the reconstructed flows with $k_l = 1$ as a function of Ra of the reference flows (cyan, filled triangles) along with $1 - E_1/E_{tot}$ and $1 - C_{s,t}$ for the reference flows. Inset shows the same plot without the log-scale on the y-axis (b) Relative scale-wise error E_v^Δ/E_v for the reconstructed flows.

measurements it would be impossible to infer neither the Rayleigh number nor the Nusselt number. In Fig. 5.9 we show the average profile of the Nusselt number as a function of the distance from the wall for the reference as well as the reconstructed flows for the moderate Ra flow and the higher Ra flow in panels (a) and (b) respectively for different k_l . As expected, for the moderate Rayleigh number flow, the Nusselt number is perfectly reconstructed as soon as we are close to the transition to perfect synchronization, except at the walls where we force $Nu \rightarrow 0$ by setting an adiabatic boundary condition. In the $k_l = 1$ case where the walls have fixed temperature identical to the reference, the Nusselt profile is reconstructed perfectly. In the higher Ra case on the other hand, even when the temperature field is perfectly synchronised, there is a large discrepancy between the reconstructed and the reference values. It is interesting to notice that the main source of errors comes from the region just after the thermal boundary layer, where the correlation between plumes and vertical velocity drafts are particularly important. In the bulk the reconstruction is accurate when the probes reach a high enough density ($k_l \geq 1/14$).

5.10.5 Varying Rayleigh Number

To further corroborate our findings reported thus far regarding the large-scale synchronization of the reconstructed flows with the reference flows, we conduct another series of nudging experiments for varying values of Ra with $k_l = 1$, that is, complete information on temperature. For all the flows, we have $\Delta_T \lesssim 10^{-3}$. We show the corresponding values of Δ_v as a function Ra in Fig. 5.10(a). The inset of the Figure shows the same but in the semilog scale. In Fig. 5.10(b) we show

the spectra of the errors E_v^Δ compensated by the spectra of the reference E_v for a selection of cases. At $Ra \sim 10^7$ the velocity field is reconstructed correctly by the nudging protocol, but at around $Ra \sim 10^8$ a transition occurs, and the nudged flow is not able to synchronize to the reference flow anymore.

In order to get a better understanding of this phenomenon, we calculate the strength of the Large Scale Circulation (LSC) by looking at the ratio of the energy in the lowest wavenumber (first Fourier mode) E_1 and the energy E_{LS} contained in the first four Fourier modes [65] given by

$$E_{LS} = E_1 + E_2 + E_3 + E_4, \quad (5.28)$$

where E_i is the average energy contained in the i -th Fourier mode. In Fig. 5.10(a), we plot (blue triangles) the deviations from the LSC strength for the various reference flows, i.e. $1 - E_1/E_{LS}$. At low Ra most of the energy is contained in the largest mode, something that is suggested by Fig. 5.3(c), while when Ra is increased, the flow becomes more turbulent and disordered, as seen in Figs. 5.3(a) and (d) and the energy contained in the smaller scales is more and more significant. We see that the deviations from the LSC scale similarly as Δ_v . The results are qualitatively the same even if we consider E_{LS} as the sum of all Fourier modes of the energy instead of just the first four, with the mean of $1 - E_1/E_{LS}$ merely shifted upward.

Further, we consider a continuous saw-tooth function λ with period L_x and translated by a distance a given by

$$\lambda(x, a) = \begin{cases} \frac{4}{L_x}(x - a), & 0 \leq x \leq \frac{L_x}{4} + a \\ -\frac{4}{L_x}(x - a) + 2, & \frac{L_x}{4} + a < x \leq \frac{3L_x}{4} - a \\ \frac{4}{L_x}(x - a) - 4, & \frac{3L_x}{4} - a < x \leq L_x \end{cases} \quad (5.29)$$

with a chosen at each instant such that

$$\int_{x=0}^{x=L_x} v(x, L_z/2, t) \cdot \lambda(x, a) dx$$

is maximum. The similarity between the saw-tooth function and the vertical velocity signal is then calculated as the time-averaged Pearson Correlation Coefficient, denoted $C_{s,t}$. In Fig. 5.10(a) we also show the value $1 - C_{s,t}$ which quantifies the deviations from the saw-tooth mode for the vertical velocity. We see again that Δ_v scales similar to the deviations from the saw-tooth function.

This picture indicates that at low Ra supplying the location of the hot and cold plumes is enough to reconstruct the flow accurately, as the plumes set the structure of the largest scales with a single dominant mode that can be approximated as a cosine or a saw-tooth. When the flow becomes more turbulent the

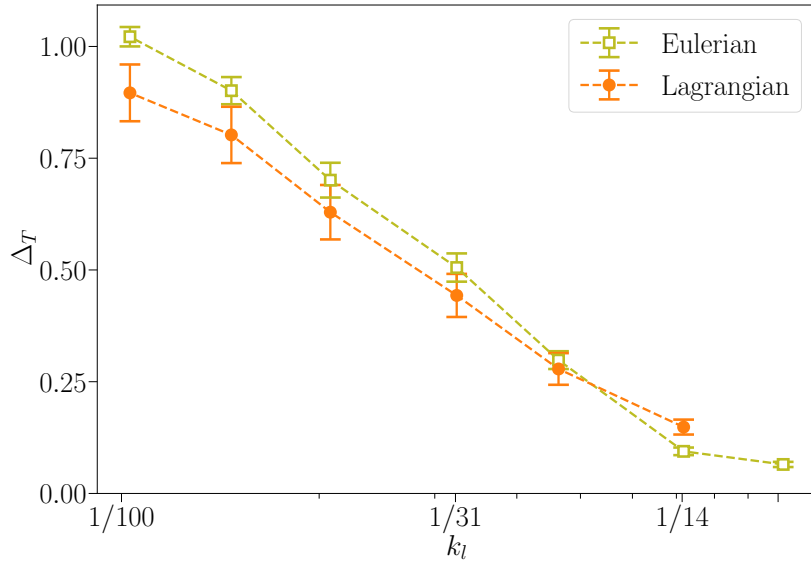


Figure 5.11: The global reconstruction error Δ_T as a function of k_l with Eulerian and Lagrangian nudging for reconstructions of the lower Ra flow with $Ra = 7.2 \times 10^7$

number of structures that can exist in the flow increases and, thus, information on the plumes positions alone cannot uniquely determine the proper solution. This, further coupled with the fact that there exist several features of the flow at smaller scales leads to a poor reconstruction of the Rayleigh-Bénard Convection at larger Rayleigh numbers.

5.11 Lagrangian Nudging

Apart from nudging using fixed temperature probes on a uniform grid as shown in figure 5.2, another novel approach to nudging is to nudge along the trajectories of tracer particles as in [66], which in our case is the same as having probes as passive tracer particles. Thus, the probe locations $\mathbf{X}^i(t)$ for $i = 1, 2, \dots, N_p$ satisfy

$$\frac{d\mathbf{X}^i(t)}{dt} = \mathbf{u}(\mathbf{X}^i(t), t) \quad (5.30)$$

Consecutive measurements of temperature and position are made with the same frequency f as the Eulerian case and both quantities are again interpolated linearly to obtain a reading at each time-step. Off-grid temperatures are obtained using a bi-linear interpolation. The nudging-squares for each probe is constructed with the nearest grid point to the interpolated probe location as the centre. In the regions

where the nudging squares of multiple probes intersect, $T_n(\mathbf{r}, t)$ is set as the mean of the $T^i(t)$ of the intersecting probes while $\alpha(\mathbf{r}, t)$ is set to be $n\alpha_0$, where n is the number of probes whose nudging squares intersect at \mathbf{r} .

As shown in Figure. 5.11, the Lagrangian approach to nudging shows only a marginal improvement in reconstruction of the temperature field for smaller k_l when compared to the Eulerian approach while the reconstruction of the velocity field remains unchanged and identical to the Eulerian case for the corresponding k_l .

5.12 Selection of the Parameters

The results presented in the main text have fixed $\chi = 6$ and $\alpha_0\tau = 4$. These results are representative of results for a larger family of parameters. The main quantitative result of the study - once Δ_T reaches a low enough value for a given flow, Δ_v reaches a saturation value - still holds true. Here we report the effect of changing the two parameters, namely the value of α and the size of the nudging squares χ . The results are summarized in Figure 5.12. In panel (a) we see that Δ_T is far larger for smaller values of α_0 with a transition to a saturation value of $\Delta_T \sim 0.1$ at $\alpha_0\tau \sim 0.4$. In panel (b) we see the variation of Δ_T for changing size of the nudging squares χ . Additionally, the ‘‘Gaussian’’ case refers a nudging experiment where we set

$$\alpha(\mathbf{r}, t) = \alpha_0 \exp\left(-\frac{|\mathbf{r} - \mathbf{X}^i(t)|^2}{2}\right), \quad \text{for } \mathbf{r} \in S_i \quad (5.31)$$

to examine whether the discontinuity of the forcing term has a significant impact on the reconstruction of the temperature field. There exists an optimum value of χ for the given flow, but the change in Δ_T is not very significant. On one hand, increasing the size of nudging squares introduces more temperature errors at the smallest scale while on the other hand, very small nudging squares lead to large regions between probes which aren’t nudged and hence decorrelate from the known temperature of the probe location. The reconstruction error in velocity for changing α_0 as well as changing χ behaves as anticipated already in figure 5.6 - Δ_v decreases with decrease in Δ_T up to a certain point and then saturates. This behaviour is qualitatively similar for the higher Ra flow as well.

5.13 Conclusions and Discussions

A study of nudging applied to a thermally driven fluid in the presence of a bulk external forcing (gravity), where the only control variable is the temperature was

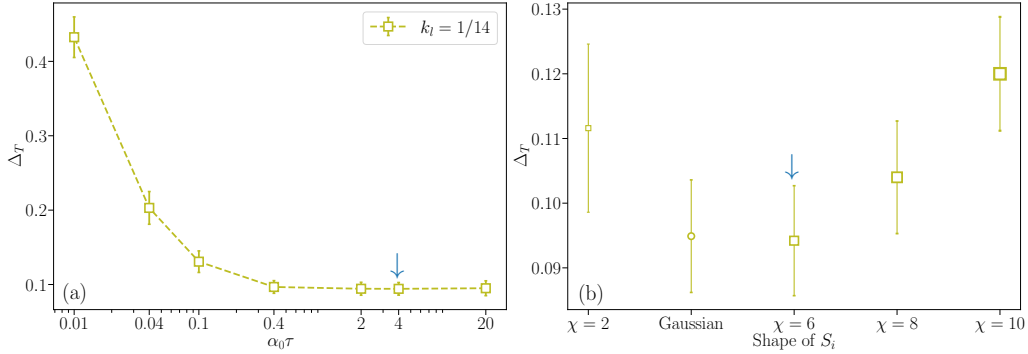


Figure 5.12: (a) Δ_T for reconstructions of the lower Ra flow with $Ra = 7.2 \times 10^7$ for $k_l = 1/14$ as a function of $\alpha_0\tau$, where only α_0 is varied. (b) Δ_T for reconstructions of the lower Ra flow for different configurations of the nudging squares for $k_l = 1/14$. The blue arrows in both panels indicate the value chosen for more detailed analysis for this study.

presented. The quantity of information as well as the quality of information to be used was varied and it has been shown that given a greater quantity of information on the temperature, the nudging method used here yields a superior reconstruction of the temperature field, with a transition to full-synchronisation around $k_l \sim 0.07$ corresponding to a distance between probes of around $7\eta_\kappa$ for both flows. The reconstruction of the velocity field on the other hand saturates from a relatively lower k_l and supplying more information, even the full temperature field with near-perfect reconstruction of temperature fails to further improve the velocity reconstruction. The degree of synchronisation between the reconstructed and the reference velocity fields depend on the Rayleigh number and the degree of turbulence in the reference flow, with the largest scales of the flow synchronising the most effectively while at smaller scales, the velocity fields remain largely asynchronous.

The quality of information was varied by following a Lagrangian approach as well as an Eulerian approach and in the construction of the nudging field T_n given the information on the temperature. While the different approaches yielded slightly different reconstructions of the temperature field, the accuracy of the reconstruction of the velocity field remains nearly the same.

Rayleigh Bénard convection is driven by the response of the vertical velocity to the local temperature. The correlation between these two fields however manifests first at the largest scales in the velocity and local temperature measurements alone fails to predict the local velocity. Providing sufficient information on the temperature provides information of these largest scale features - the plumes - and hence the large-scale flow. This study thus helps to understand the fundamental

role played by the temperature field alone in the Rayleigh-Bénard convection and answers the question – how much does the velocity field depend on the quantity and quality of information available on the temperature field? The accurate reconstruction of the velocity field at lower Rayleigh numbers is a result of the relative absence of smaller and fine scale structure in such flows. At higher Ra, when the thermal flow is more turbulent, richer in small-scale structures, with thermal plumes less well-defined and rapidly fluctuating velocity field, the indirect reconstruction of the velocity field reproduces the correct flow dynamics and synchronises relatively poorly even at the largest scale, though the relative error on the first Fourier mode is still of the order $\sim 10^{-1}$ for the flow with $Ra \sim 10^9$ and highly turbulent. To accurately reconstruct the smaller and smaller scales would require additional inputs into the system - it is conceivable, for example, that even a small amount of data on the velocity field could drastically improve the accuracy of the reconstructed velocity field and that there exists an optimum way to supply a combination of temperature and velocity data. In this study the focus was exclusively on the reconstructions using the temperature field alone and the possibility of using a combination of temperature and velocity fields has been left for future work.

Chapter 6

Study on Two-way thermally coupled Particles

Summary The chapter briefly introduces the reader to the dynamics of particles suspended in turbulent flows and the phenomenon of preferential concentration. Studies on non-isothermal particles which interact thermally with the fluid are introduced, along with a motivation to study internally heated system. Following this, details of the study conducted as part of the thesis work on thermally interacting particles suspended in a fluid are described. The equations describing the dynamics of the fluid and the response of the particles to fluid are given and the numerical set-up along with the various parameters of the system are described. Virtual tracer particles are considered whose temperature depends on their vertical velocity and an interesting effect is reported - when the particle temperature depends on the direction of the vertical motion, a stable temperature gradient is obtained and two clearly divergent end-states (stable configuration vs. convective motion) are observed and a sharp transition occurs. The results from the novel system for varying parameters are presented, including the magnitude of the turbulent kinetic energy, the nature of the energy spectra and the temperature profiles as well as the heat transfer across the domain. The particle system is also compared with a Eulerian system where an identical thermal forcing is applied. The chapter is concluded with a section summarising the results and a discussion on the key physical insights gained from the study as well as the possibility for future work building on it.

6.1 Particles in Turbulence

Particles suspended in turbulent flows show highly complex, non-linear interactions with the carrier phase. The trajectories of the particles are determined by the

local flow velocity at the particle location and the mass, or *inertia* of the particle. When the volume fraction of the domain occupied by the particles is negligible (dilute suspension) and the particle sizes are small, the particles can be assumed to have no feedback on the fluid flow and the fluid flow can be assumed to remain unchanged by the presence of the particles. When the volume fraction of particles is significant or the particle sizes are comparable to or larger than the smallest flow features of the fluid (of order η), then particle effects on the fluid cannot be ignored and a two-way coupled system has to be considered where the flow acts on the particles to determine their trajectory while the particles in return affect the flow.

Examples of systems with particles suspended in turbulent flows are extremely common. The dispersal of aerosols in the atmosphere, which includes smoke, dust, pollen, pollutants, etc is one such example. Aerosols of appropriate chemical composition may also act as condensation centres for water vapour and thus become nuclei for cloud droplets in the atmosphere. The response of cloud droplets to the turbulence present in clouds is known to have a significant impact in the initiation of rain, where the collisions of millions of cloud droplets eventually leads to their aggregation and formation of rain droplets. The rapidity of this process in natural settings is explained by intense turbulence of cloud flows. The formation of planets by the aggregation of planetesimals is also an example of a turbulent flow with particles suspended - a special case where the turbulent flow itself is significantly affected by the feedback from the suspended planetesimals.

Tracer particles are particles which follow the local flow exactly - ie., the particle velocity \mathbf{u}_i of the i -th particle is given by

$$\mathbf{u}_i(t) = \mathbf{u}(\mathbf{x}_i(t), t) \quad (6.1)$$

where \mathbf{x}_i is the location of the particle and $\mathbf{u}(\mathbf{x}, t)$ is the fluid velocity field. Tracer particles are of two kinds - either they are particles which are extremely light and small, and hence relax to the local fluid velocity instantaneously. Or, they are particles whose density is identical to the fluid density. Tracer particles, such as dyes injected into the fluid, help experimenters to visualise flow trajectories and indirectly measure flow statistics as well. This is also exploited in *Particle tracking velocimetry*, where the particles are often fluorescent under illumination by certain types of light, allowing clear visualisation of the flow by tracking these injected particles.

Heavier particles which do not exactly follow the flow trajectory are known as inertial particles. The simplest dynamics for heavy inertial particles, in the limit of dilute suspensions and small particle size, is given by the simplified Maxey-Riley equation [67] -

$$\mathbf{u}_i(t) = -\frac{1}{\tau_p} [\mathbf{u}_i(t) - \mathbf{u}(\mathbf{x}_i(t), t)], \quad (6.2)$$

that is, the particle velocity relaxes to the local fluid velocity with a time-lag of order τ_p , where τ_p depends on the particle size, the fluid viscosity ν and the relative density of the particle with respect to the fluid. An important dimensionless parameter is the Stokes number St , given by

$$St = \frac{\tau_p}{\tau_\eta}, \quad (6.3)$$

which is a ratio of the timescale of the particle reponse to the flows to the fastest intrinsic timescale of the flow, the Kolmogorov time-scale. When $St \ll 1$, the particle behaves like a tracer, while when $St \gg 1$, the particle is extremely heavy and remains nearly unaffected by the flow.

6.2 Preferential Concentration

An important and widely studied dynamic effect of inertial particles is *preferential concentration*, the tendency of particles to aggregate outside the vortical regions of the flow, which correspond to regions with relatively higher shear. This occurs due to the ejection of inertial particles from vortical regions. The Stokes number captures the average response of the particle to the flow - however, in rapidly rotating, highly dissipative vortical regions of the flow, the effective time-scale of the fluctuations of the velocity field of the fluid is far smaller (quicker) than on average, and thus if we consider an effective, local St , then the particle behaves like a heavy particle and rather than being entrained in the vortical region, it is ejected so that on average, particles spend less time in these regions of high vorticity. Thus, preferential concentration is a direct result of the finite response time of the particle to the flow.

While very light particles ($St \lll 1$) or very heavy particles ($St \ggg 1$) do not show preferential concentration, the concentration of particles outside the vortical regions is most enhanced for particles with $St \sim 1$.

6.3 Non-isothermal Particles in Thermal Flows and Internal Heating

Suspended particles which are non-isothermal and thermally coupled to the flow, that is, there is exchange of heat between the particle and the flow, create local temperature fluctuations in the fluid, which in turn can further modify a turbulent,

thermal flow. The modification can be due to the thermal action alone or due to a combination of thermal coupling and two-way momentum coupling [22]. Even in case of thermally uncoupled particles, the modification of the flow by two-way momentum coupling with the particles can alter the heat-transfer dynamics of a thermal flow [68].

Thermally coupled particles suspended in a flow are a form of *internal heating*, wherein the flow is driven by heat injected into the bulk of the system rather than via boundary conditions, as in the Rayleigh-Bénard convection and several atmospheric flows. The convection and dynamics arising from internal heating is relevant to specific natural settings as well, such as the driving of convection in the earth's mantle [69]. The thick atmosphere of Venus rich in sulphurous gases directly absorbs heat from the sun through radiation and this is the dominant mode of heat input into the system, in contrast with the earth's atmosphere where radiative heating of the ground which in turn acts as a hot boundary layer for the atmosphere is the dominant mode of heating [70]. Internal heating is also seen in industrial applications such as in liquid-metal batteries [71]. Thus, the convection and flows induced by internal heating mechanisms have a wide range of applications. An idealised system of internal heating was studied by Wang et. al [72] to formulate a unifying theory of internal heating under idealised conditions (constant bulk heating with fixed temperature boundary conditions) and establish a theoretical foundation for future studies on internally heated flows.

Concerning thermally interacting particles, individual heated particles is isolation merely form small localised plumes or temperature fluctuations which are dissipated away in short times. When particles are inertial, their concentration away from vortical regions (preferential concentration) causes an aggregate effect with significant alteration to the large-scale flow. This has been observed in Rayleigh-Bénard convection [73], where the enhancement of heat transfer by the seeding of hot particles has been found to be maximum for particles with St of order 1, or the particles with the greatest tendency towards preferential concentration. In studies with no large-scale driving thermal boundary [74, 75], particles constantly heated uniformly by incident radiation were found to activate the flow and even induce a self-sustaining turbulent thermal convection, which again showed the highest degree of turbulence for particles with $St = 1$.

6.4 Study on virtual non-isothermal particles

The above described numerical experiments all make several idealisations and assumptions, in the interest of first understanding the dynamics of model systems before proceeding to natural systems. A common feature of these systems is that the temperature is constantly increasing on average. In the idealised bulk internal

heating study, it is ensured the temperature doesn't rise by imposing fixed temperature boundaries. However, this ceases to be a purely internally heated system.

To further understand the dynamics of an internally heated, convective system, we perform a numerical study of an idealised system with a fixed average temperature. In this study, we envisage as a first step a system with suspended “virtual” tracer particles in a fluid which interact only thermally with the fluid, i.e., they do not affect the local momentum of the fluid. In this proposed idealisation, the particles are either hot (release heat) or cold (absorb heat) and the temperature of these particles is set by an internal mechanism rather than any uniform external heating. In such a scenario, the system is internally heated as well as cooled by these virtual particles so that the average heating term Φ is statistically zero and hence the average attained by the fluid is thus zero as well. The heat injection by the particles are the only energy source for the 2D system, since the horizontal boundary walls are periodic and the top and bottom walls are adiabatic. In this phenomenological study, we investigate the attained stationary end-states when such a system is initialised and allowed to evolve according to the above properties, finding a protocol that can induce and sustain large-scale thermal convection under the right conditions while also leading to a quiescent stationary state without convection otherwise. The method serves to add a novel possibility of conditioning the specific particle coupling on the dynamics of the particles and understanding ways to achieve control or modulation through Lagrangian approaches.

6.5 Methods and Equations of Motion

The particle forcing protocol in this study is as follows - virtual tracer particles are initially seeded randomly in a 2D domain of length L_x and height L_z with a fluid at rest. The initial temperature of the fluid is set to an unstable configuration with hotter temperatures at the bottom of the domain and colder temperature at the top of the domain. The particles are idealised to have infinite heat capacity and a temperature determined by an imposed temperature protocol where rising, vertically upward moving particles are warm with a positive temperature T_+ while the temperature of falling particles ($v < 0$) is set to $-T_+$. The temperature of the fluid in the vicinity of the particle relaxes to the temperature of the particle at a rate proportional to the difference between the local fluid temperature T and the particle temperature T with a relaxation time $\tau = 1/\alpha$, where the value of $\alpha(\mathbf{r}, t)$ depends on the distance of the point \mathbf{r} from the locations of the particles.

The fluid velocity $\mathbf{u} = (u, v)$ and temperature T follow the equations

$$\nabla \cdot \mathbf{u} = 0, \quad (6.4)$$

$$\partial_t \mathbf{u} + (\mathbf{u} \cdot \nabla) \mathbf{u} = -\nabla p + \nu \nabla^2 \mathbf{u} - \beta T \mathbf{g}, \quad (6.5)$$

$$\frac{\partial T}{\partial t} + \mathbf{u} \nabla T = \kappa \nabla^2 T - \alpha(T - T_p), \quad (6.6)$$

where equations (6.4) and (6.5) are the incompressible Navier-Stokes equations for a fluid of unit density and average temperature $T = 0$ with a buoyancy-force term following the Boussinesq approximation, where density variations are small and enter the equations only through the gravity-force term. Here, p is the fluid pressure, ν is the kinematic viscosity of the fluid, β is the thermal expansion coefficient of the fluid. Equation (6.6) is the advection-diffusion equation for the heat with κ the thermal conductivity and $\Phi = -\alpha(T - T_p)$ is a heat-source term (i.e., a thermal forcing term) that depends on the virtual thermal particles, with T_p being the effective particle temperature defined later.

The domain is periodic in the horizontal x direction while the top and bottom walls at $z = 0$ and $z = L_z$ are adiabatic with $\mathbf{u} = 0$, that is

$$\left. \frac{\partial T}{\partial z} \right|_{z=0} = \left. \frac{\partial T}{\partial z} \right|_{z=L_z} = 0, \quad (6.7)$$

$$\mathbf{u}(z = 0) = \mathbf{u}(z = L_z) = 0. \quad (6.8)$$

Note that the only source of energy injection into the system is via the particle heat injection.

6.5.1 Equations of Particle Motion

The N_p tracer particles with positions $\mathbf{R} = \{\mathbf{r}_1, \mathbf{r}_2, \dots, \mathbf{r}_{N_p}\}$ and temperatures $\mathbf{T} = \{T_1, T_2, \dots, T_{N_p}\}$ are initially seeded randomly. The particles have the same velocity as the fluid at the particle location, that is

$$\mathbf{u}_i(t) = \mathbf{u}(\mathbf{r}_i(t), t), \quad (6.9)$$

where \mathbf{u}_i is the velocity of the i -th particle and \mathbf{u} is the fluid velocity.

Each particle exerts a thermal forcing on the fluid in its immediate vicinity up to a distance η . The feedback of the particle is defined as a local heat injection term that is proportional to the difference between the underlying fluid temperature at the location of the particle and the set temperature of the particle. The strength of the coupling α between the i -th particle and the fluid (with dimension $1/t$) at time t has the form of a Gaussian with a peak at $\mathbf{r}_i(t)$, given by

$$\alpha_i(\mathbf{r}, t) = \begin{cases} \alpha_0 \exp\left(-\frac{|\mathbf{r} - \mathbf{r}_i(t)|^2}{2c^2}\right), & \text{if } |\mathbf{r} - \mathbf{r}_i| \leq \eta, \\ 0, & \text{if } |\mathbf{r} - \mathbf{r}_i| > \eta, \end{cases} \quad (6.10)$$

where α_0 is the coupling strength at the particle location and c is the size of the virtual particle and defines the sharpness of the peak for the function α_i . The thermal forcing due to the i -th particle at \mathbf{r} is thus

$$\Phi_i(\mathbf{r}, t) = -\alpha_i(\mathbf{r}, t)[T(\mathbf{r}, t) - T_i(t)], \quad (6.11)$$

and so the total thermal forcing at a given location \mathbf{r} is

$$\Phi(\mathbf{r}, t) = -\sum_{i=1}^{i=N_p} \left(\alpha_i(\mathbf{r}, t)[T(\mathbf{r}, t) - T_i(t)] \right). \quad (6.12)$$

This can be rewritten as

$$\Phi(\mathbf{r}, t) = -\alpha(\mathbf{r}, t)[T(\mathbf{r}, t) - T_p(\mathbf{r}, t)], \quad (6.13)$$

where

$$\alpha(\mathbf{r}, t) = \sum_{i=1}^{i=N_p} \alpha_i(\mathbf{r}, t) \quad (6.14)$$

is the effective coupling strength and

$$T_p(\mathbf{r}, t) = \frac{\sum_{i=1}^{i=N_p} \alpha_i(\mathbf{r}, t) T_i(t)}{\sum_{i=1}^{i=N_p} \alpha_i(\mathbf{r}, t)} \quad (6.15)$$

is the effective particle temperature at \mathbf{r} . Each particle influences a fixed region surrounding it and when two particles are within distance 2η , their effects are additive.

6.5.2 Particle Temperature Policy

The temperatures of the particles $\mathbf{T}(t) = \{T_1(t), T_2(t), \dots, T_{N_p}(t)\}$ is set by a policy wherein the i -th particle either has a positive value T_+ or a negative value $-T_+$ depending on the sign of the fluid vertical velocity $v(\mathbf{r}, t)$. Since the particle is a tracer, we have

$$T_i = \begin{cases} T_+, & \text{if } v_i > 0 \\ -T_+, & \text{if } v_i < 0 \end{cases}, \quad (6.16)$$

where v_i is the vertical velocity of the i -th particle. T_+ is a parameter that sets the temperature scale of the system. By heating the regions of fluid moving upward and vice-versa for the downward moving regions, this policy would be expected to enhance thermal convection by strengthening any updrafts or downdrafts, if such exist. The particles and the fluid are coupled to each other since the particles follow the fluid velocity as tracers, which is in turn affected by the temperature field.

6.5.3 Numerical Experiments

With an initial unstable vertical temperature profile of

$$T(z) = \tanh\left(\frac{L_z}{2} - z\right)T_+, \quad (6.17)$$

the fluid equations (6.4) - (1.6) are solved by the Lattice-Boltzmann method along with the particle evolution as tracers given by equation (6.9). The two-way coupled particle-fluid system is evolved until the flow attains a statistically stationary kinetic energy. All measurements and analysis are performed in this stationary state for various sets of parameters, varying T_+, N_p, α_0 and c . The radius of the particle η is kept fixed throughout this study.

We define an important quantity, namely the *typical vertical velocity* of each particle u_0 given by

$$u_0 = \sqrt{cg\beta \frac{\alpha_0}{\alpha_0 + \frac{\kappa}{2c^2}} T_+} \quad (6.18)$$

where c is the size of the particle as defined in equation (6.10) and κ is the thermal conductivity of the fluid. The fluid in the vicinity of the particle relaxes to the temperature of the particle, and this relatively hotter (or cooler) fluid rises (or falls). The tracer particle in turn responds to the fluid and the accelerates at a rate depending on the temperature anomaly, thus depending on g and β , similar to other thermal flows such as the Rayleigh-Bénard convection. The local heating is greater for greater c as a larger area surrounding each particle is thermally forced. The quantity

$$T_a = \frac{\alpha_0}{\alpha_0 + \frac{\kappa}{2c^2}} T_+ \quad (6.19)$$

is an *effective temperature* attained in the vicinity of each particle. The pre-factor multiplying T_+ is a constant quantifying the rate of relaxation of the fluid temperature to the particle temperature α_0 relative to the rate at which heat is diffused away from the particle by conduction proportional to $\kappa/(2c^2)$. We see that when $\alpha_0 \rightarrow 0$, $T_a \rightarrow 0$, as the system is no longer forced thermally and there is no energy input into the system. When $\alpha_0 \rightarrow \infty$, $T_a \rightarrow T_+$, ie., the fluid immediately relaxes to the particle temperature. For large κ , the heat is conducted away from the particle rapidly and thus the effective temperature of the particle is lower while the case of small κ is similar to having large α_0 . The particular form of the expression of the typical velocity is verified by considering an ensemble of systems with $N_p = 1$ and varying α_0 and c . The r.m.s mean of the particle vertical velocity v_i is found to scale as equation 6.18. In particular, it is verified that the particle velocity statistics remain independent of domain height L_z , thus justifying the choice of c as the length scale of the system. Further, the normalised *turbulent kinetic energy*

$E_k(t)$ of the system is defined as

$$E_k(t) = \frac{1}{2} \frac{\langle |\mathbf{u}(t)|^2 \rangle_V}{u_0^2 N_p}, \quad (6.20)$$

where $\langle \cdot \rangle_V$ represents the average over the whole domain at a given instant of time. We also define with an over-line \overline{E}_k as the average normalised turbulent kinetic energy (TKE), that is

$$\overline{E}_k = \langle E_k(t) \rangle_t, \quad (6.21)$$

where $\langle \cdot \rangle_t$ denotes the time average after the flow has attained a statistically stationary kinetic energy. When the particles are sparse and their motion is independent of each other, the kinetic energy of the system would simply be a sum of the motion of the individual particles and we expect E_k to remain constant. If however the motion of the particles are not merely additive but they induce a larger-scale flow in the system, we would expect E_k to increase as a function of N_p .

6.6 Results

6.6.1 Stable and Convective Configurations

We start by showing in Figure 6.1 for a given rising particle temperature T_+ , particle-fluid coupling strength α_0 and particle size c , visualisations of the temperature fields for varying the number of virtual particles N_p . The visualisations show a snapshot of the flows after they have attained a statistically stationary kinetic energy. The figure indicates that there are two distinct stationary end-states for the system. The first end-state, which we term *Stable* and show in the top panels of the figure, is a low kinetic energy, quiescent state where a large scale circulation is absent. Particles are either nearly still and close to the top and bottom walls or they execute a slow vertical motion, propelled by their higher or lower temperature compared to the bulk. When the particle concentration reaches beyond a certain threshold, which in the case of the Figure 6.1 lies between $N_p = 140$ and $N_p = 160$, the individual thermal effect of the particles aggregates and triggers a transition to a second end-state, which we term *Convective* and show in the bottom panels of the figure. The Convective state shows large scale circulation, the clear presence of a rising plume and a falling plume and particles themselves following trajectories along the large counter-rotating vortices.

While the transition from the Stable state to Convective state is shown qualitatively in the snapshots of Figure 6.1, Figure 6.2 shows the magnitude of increase in

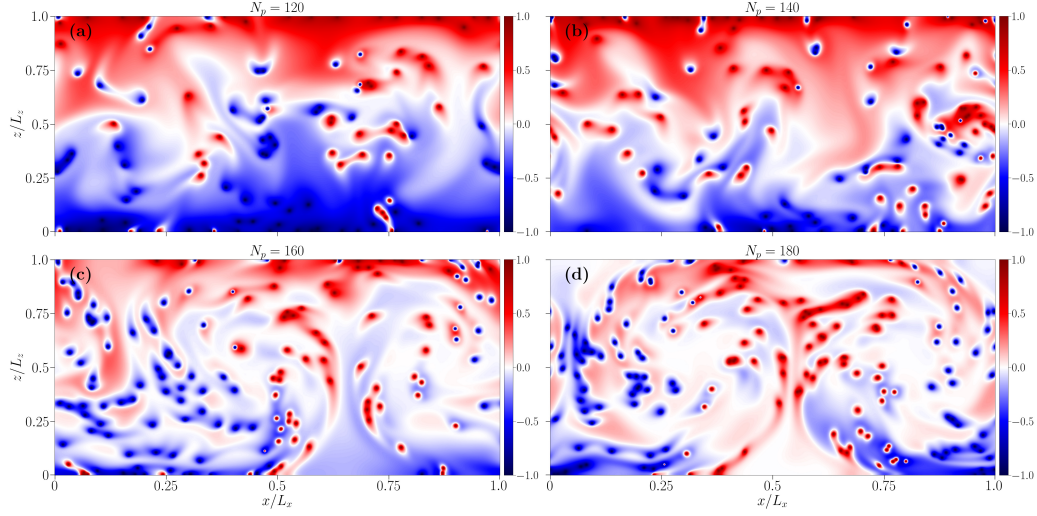


Figure 6.1: Snapshots of the temperature field $T(\mathbf{r}, t)/T_+$ at a given instant of time for $T_+ = 0.1$, $\alpha_0 = 0.005$ and varying N_p where red indicates $T = T_+$ and blue indicates $T = -T_+$. The top panels show a Stable end-state configuration while the bottom panels show a Convective end-state configuration. The transition is triggered by increasing N_p .

the turbulent kinetic energy (TKE) of the flow at the transition. The figure shows in panels (a), (b) and (c) respectively the evolution of the normalised TKE defined in equation (6.20) for flows with $T_+ = 0.02$, $T_+ = 0.1$ and $T_+ = 1.0$ respectively for a fixed α_0 and c . The blue curves represent Stable configurations while the red curves represent Convective configurations. The kinetic energy first increases due to the unstable temperature gradient imposed on the flow initially with the vertical temperature profile given by equation (6.17). At larger times, the effect of the virtual particles is dominant and the flows attains a statistically stationary kinetic energy, where the $E_k(t)$ either shows a value $> 10^{-1}$ (red curves), corresponding to the Convective flows seen qualitatively in Figure 6.1 or $E_k(t) < 10^{-1}$ (blue) corresponding to the Stable flows.

Two further points are note-worthy about the transition from Figure 6.2. Firstly, the sharpness of the transition, where for adding very few particles, the normalised kinetic energy increases by a factor of $\gtrsim 5$. It should be noted that the expression of $E_k(t)$ has N_p in the denominator, so the absolute increase in kinetic energy is even greater. Secondly, the N_p of transition depends on T_+ , where for larger T_+ , the transition occurs at a slightly larger N_p . We see that in panel (a) with $T_+ = 0.02$, the transition lies between $N_p = 120$ and $N_p = 140$ while in panel (c) with $T_+ = 1.0$, the transition lies between $N_p = 160$ and $N_p = 180$, with the case of $T_+ = 0.1$ in panel (b) showing an intermediate behaviour. This is a weak

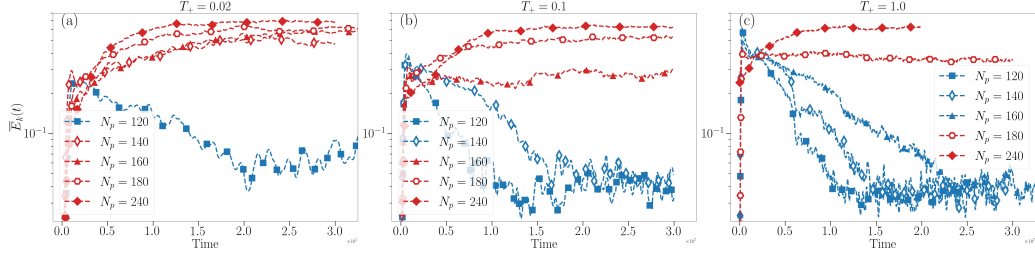


Figure 6.2: Time evolution of $E_k(t)$ for flows with $T_+ =$ (a) 0.02, (b) 0.1 and (c) 1.0. Stable end-state configurations are plotted in blue while Convective end-state configurations are plotted in red. The time is in simulation time units.

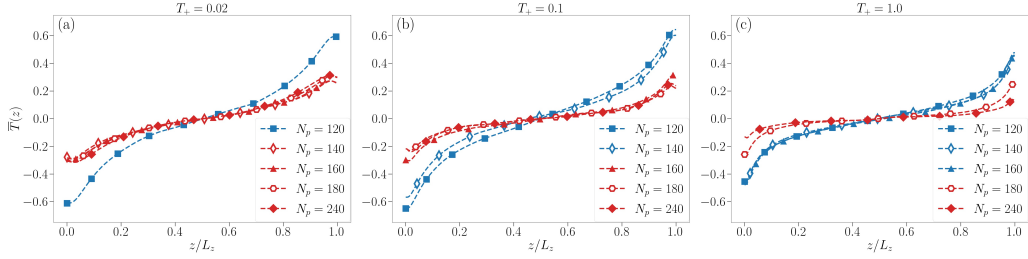


Figure 6.3: Time-averaged vertical temperature profile divided by T_+ plotted against the vertical height for various N_p close to the transition N_p for (a) $T_+ = 0.02$, (b) $T_+ = 0.1$ and (c) $T_+ = 1.0$. Stable configurations are plotted in blue while Convective configurations are shown in red.

dependence on T_+ .

In Figure 6.3, we show a comparison of the normalised time-averaged vertical temperature profiles $\bar{T}(z)$ for the same set of flows given by

$$\bar{T}(z) = \frac{\langle T(\mathbf{r}, t) \rangle_{x,t}}{T_+} \quad (6.22)$$

where $\langle \cdot \rangle_{x,t}$ represents the time-average at a given height z . Notice that the temperature gradients for the Stable flows (blue) show a strongly stable profile ($\partial_z T > 0$) while the Convective flows still show a stable temperature profile but with weaker gradients so that the temperature difference between the top and the bottom adiabatic walls are much smaller. The reason for this is that in the presence of a large-scale circulation, the temperature field is more effectively transported and mixed throughout the domain. We also see that with increase in T_+ , the Stable configurations show a flatter temperature profile for the corresponding N_p of lower T_+ flows, i.e., for example, the red curves in panel (c) are much flatter than those in panel (a). The dual-nature of the effect of the virtual particles is observed here - the particles tend to make the flow more stable by carrying heat

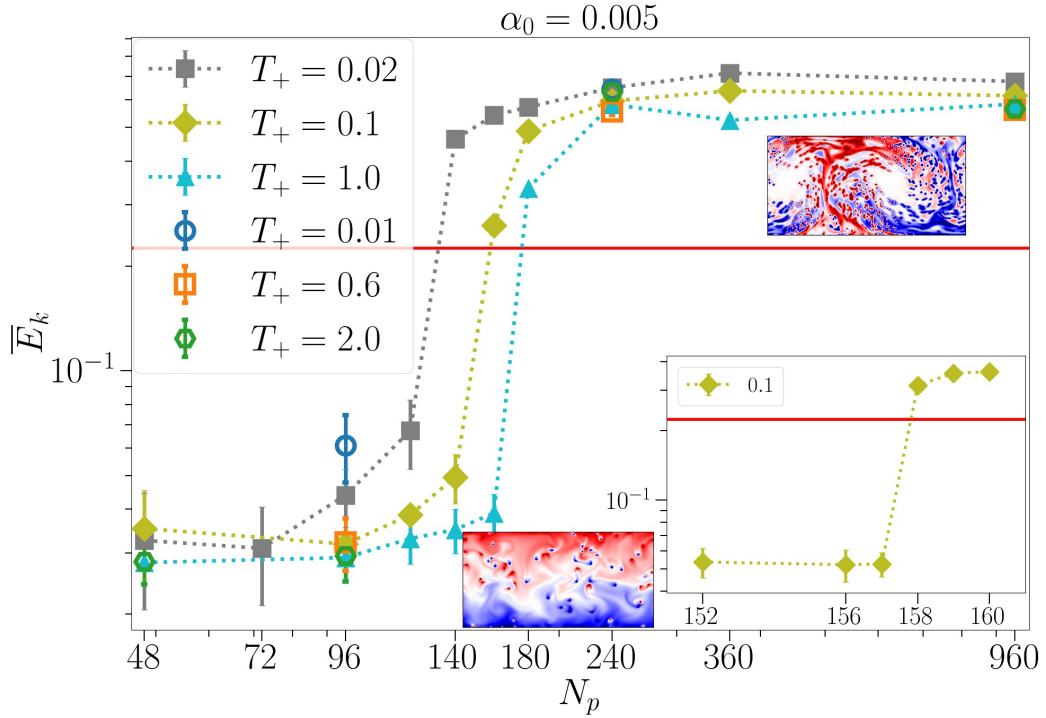


Figure 6.4: Time averaged normalized TKE as a function of N_p for various T_+ (shown in legend). Inset shows behaviour of flows with $T_+ = 0.1$ very close to the transition N_p . Also shown are instantaneous snapshots of the temperature field for a Stable configuration (bottom left) and a Convective configuration (top right).

away from the lower half of the domain while carrying heat towards the upper half of the domain. Thus, the larger T_+ is, the more stable the system. However, when a certain threshold of particles is reached, the situation changes - the virtual particles together create a persistent large-scale flow and now the convection is strong enough to overcome the stable temperature gradient.

In Figure 6.4 we take a closer look at the transition by plotting the average normalised TKE of the flows as defined in equation (6.21) against N_p for the same α_0 as above for various T_+ . The sharp increase of TKE at a transition N_p is once again clearly visible. We empirically define a value of $E_k^0 = 0.225$ indicated by the horizontal red line as the transition point where for Stable end-states, $\overline{E}_k < E_k^0$ and vice-versa for the Convection end-state. The sharpness of the transition is examined more closely in the inset of the figure for a given T_+ . It is seen that the transition occurs for an increase of just a single virtual particle. The dependence on T_+ is weak as evidenced by the fact that for T_+ varying over 2 orders of magnitude ($10^{-2} - 10^0$), the transition occurs at nearly the same N_p .

6.6.2 Large-scale Circulation and Heat Transfer

While the existence of the large-scale circulation is apparent from the visualisations of the temperature field, it is possible to infer its presence quantitatively from the fluid energy spectrum. In particular, we consider the spectrum in the horizontal direction taken at the mid-plane $z = L_z/2$, given by

$$E_{\mathbf{u}}(k_x) = \frac{1}{2} \langle |\hat{\mathbf{u}}(k_x, z_0, t)|^2 \rangle_t, \quad (6.23)$$

where $z_0 = L_z/2$ and $\hat{\mathbf{u}}(k_x, z_0, t)$ are the Fourier coefficients of the field \mathbf{u} and $\langle \cdot \rangle_t$ denotes the time averaging. We denote E_1 to be the energy contained in the first Fourier mode, E_2 for the second mode, and so on and define

$$E_{tot} = \sum_{i=1}^{\infty} E_i. \quad (6.24)$$

The strength of the large-scale circulation with a rising plume and a falling plume can be measured by the value E_1/E_{tot} [65], which measures the fraction of energy contained in the first mode, that is the smallest wavenumber. This corresponds to a cosine mode for the velocity field in the bulk, which is a close approximation of the form of the velocity field when there exist two plumes and the bulk of the kinetic energy is contained in the large-scale flow of two counter-rotating vortices. When such a large-scale flow is present, we would have $E_1/E_{tot} \gg 0$, while if the flow lacks large-scale convection, we would have a flatter energy spectrum with $E_1/E_{tot} \rightarrow 0$ and $E_1 \sim E_2$.

In Figure 6.5(a), we plot the strength of the large-scale circulation E_1/E_{tot} for varying N_p . We see clearly here that corresponding to a jump in the magnitude of the TKE seen in Figure 6.4, there is also a similar large increase in the ratio of kinetic energy contained in the largest-scale. This is a clear demonstration that the main difference between the Stable and the Convective states is the existence of the large scale flow. Given that the kinetic energy shown is normalised by the typical velocity of a single particle and the number of particles, the excess kinetic energy comes from the large-scale circulation that arises after the transition, a cumulative particle effect.

Panel (b) of the same figure shows the dimensionless Nusselt number, defined as

$$Nu = \frac{\langle vT - \kappa \frac{\partial T}{\partial z} \rangle_{V,t}}{\frac{\kappa \overline{\Delta T}}{L_z}} \quad (6.25)$$

where $\langle \cdot \rangle_{V,t}$ represents average over the entire domain and time and $\overline{\Delta T}$ is the

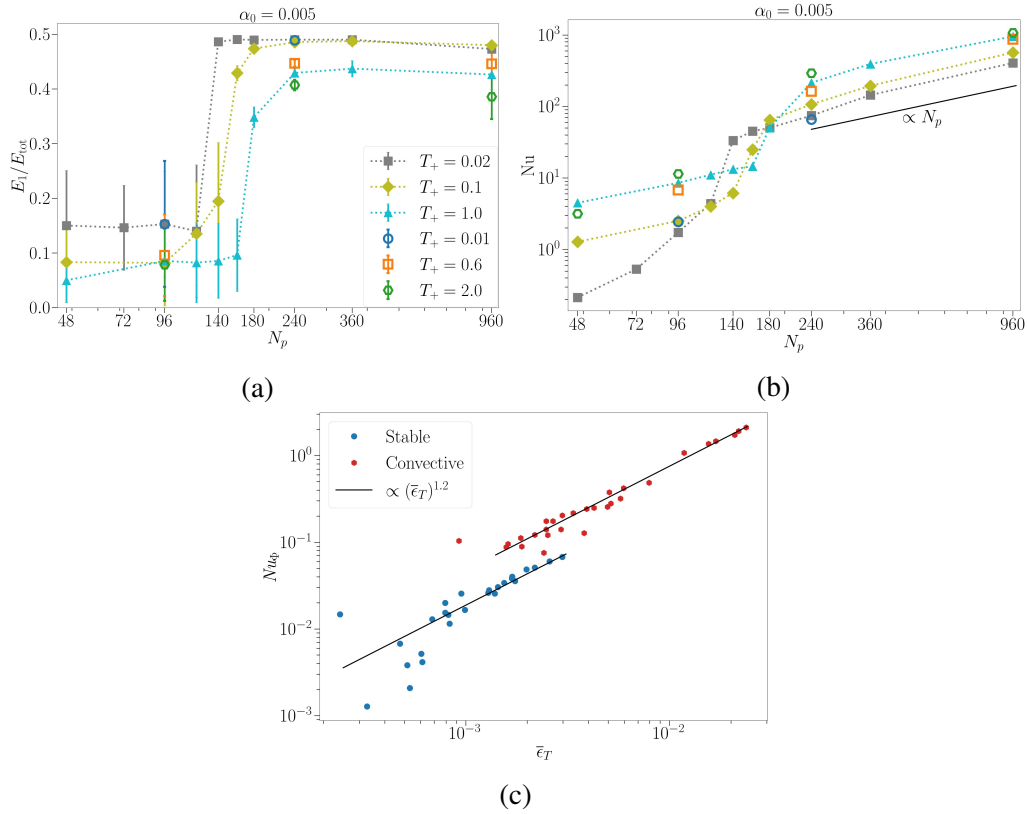


Figure 6.5: (a) E_1/E_{tot} for varying N_p for various values of T_+ . (b) Nu for varying N_p for various values of T_+ . The black solid line shows a linear scaling with N_p . (c) Plot of the average normalised Nusselt number Nu_ϕ against the average normalised thermal energy injection $\bar{\epsilon}_T$ for flows with varying parameters. Stable flows are marked with blue filled circles, Convective with red filled triangles and the two black lines scale as $(\bar{\epsilon}_T)^{1.2}$

average temperature difference between the top and bottom walls given by

$$\overline{\Delta T} = \overline{T}(L_z) - \overline{T}(0). \quad (6.26)$$

The Nusselt number is defined here analogous to the definition for the Rayleigh-Bénard convection and is the ratio of heat transfer due to convection to the heat transfer by conduction. We see that the increase in Nu increases with increase in N_p followed by a large increase around the transition N_p and then settling to a roughly linear increase with N_p in the Convective regime.

The effective temperature T_a defined in equation (6.19) was introduced as a typical value of the temperature attained by the fluid in the vicinity of the particle with an associated length-scale c for each particle. In a similar vein, $\alpha_0(T_+ - T_a)$ is the typical thermal forcing acting on the fluid. We can thus define two important dimensionless response parameters of the system. First, we define the normalised Nusselt number Nu_Φ given by

$$Nu_\Phi = \frac{\langle vT - \kappa \frac{\partial T}{\partial z} \rangle_{V,t}}{c\alpha_0(T_+ - T_a)}. \quad (6.27)$$

Nu_Φ measures the heat transfer by convection relative to the input typical thermal forcing multiplied by the length scale of the system, similar to the Nusselt number defined by [76].

The thermal energy injection ϵ_T given by $\langle \Phi T \rangle_{V,t}$ is normalised as

$$\bar{\epsilon}_T = \frac{\langle \Phi T \rangle_{V,t}}{\alpha_0(T_+ - T_a)T_+}. \quad (6.28)$$

In panel (c) we plot the normalised Nusselt number Nu_Φ against the normalised heat injection $\bar{\epsilon}_T$, quantifying the measured convective response of the fluid to the measured input thermal forcing for varying T_+ , c , α_0 and N_p . It is seen that there exists a global scaling of these two quantities for both the flow regimes, Stable and Convective with a rough scaling of $Nu_\Phi \propto (\bar{\epsilon}_T)^{1.2}$. However, the higher magnitude of the normalised Nusselt number in the Convective case differentiates it from the Stable flows.

The above findings are consistent with a situation that can be described as such - individual particles thermally coupled to the fluid have a small zone of influence and release or absorb heat in their immediate vicinity. Thus, each particle contributes to the thermal injection into the domain as well as the vertical heat transfer across the domain. The heat injection as well as vertical heat transfer increase with the increase in number of particles. In the Stable regime, the main effect of the particles is to maintain the strongly stable temperature gradient. At the transition to the Convective regime, the development of the large-scale convective flow patterns and more turbulent flow leads to a large increase in the heat

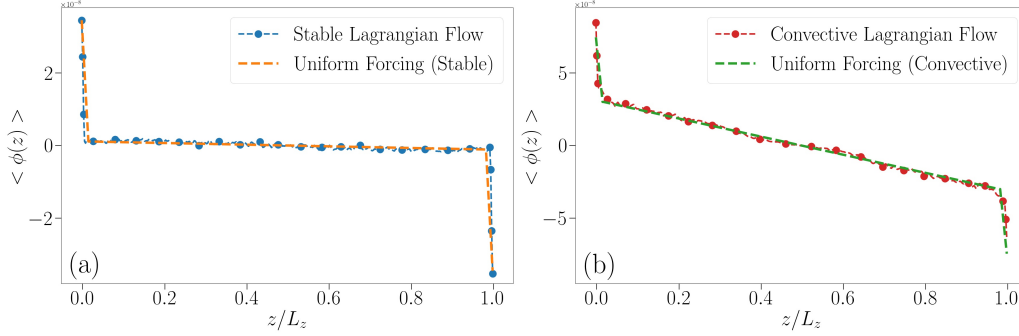


Figure 6.6: The measured value of the average vertical profile of thermal forcing $\Phi = -\alpha(T - T_p)$ for a stable flow (a) and for a convective flow (b) compared to the imposed vertical profile of the thermal forcing.

transfer relative even to the thermal energy injection, while also seeing a weaker vertical temperature gradient across the domain.

6.6.3 Exact Relations

Two exact relations have been derived for the Rayleigh-Bénard convection in Section 3.4.1. The system under consideration here varies from the Rayleigh-Bénard convection in two crucial respects. Firstly, the temperature boundary conditions in the RB convection have walls with fixed temperature while those in the study here have adiabatic walls. Further, the heat-equation contains the additional term Φ . It is easy to hence verify that for the viscous dissipation ϵ ,

$$\epsilon = \beta g(Nu - 1) \frac{\kappa \Delta T_f}{L_z}. \quad (6.29)$$

For the thermal dissipation, we have

$$\epsilon_\theta = \langle \Phi T \rangle_{V,t}, \quad (6.30)$$

as the top and bottom walls are adiabatic with no heat-flux, hence the $\nabla^2 T$ term has no contribution to the dissipation equation.

6.6.4 Comparison with Eulerian imposed thermal forcing

We consider a thermal fluid system with a thermal forcing $\phi(z)$ uniformly applied at all times. The forcing is a close approximation of the forcing Φ measured in the Lagrangian system with the virtual particles in the domain as shown in

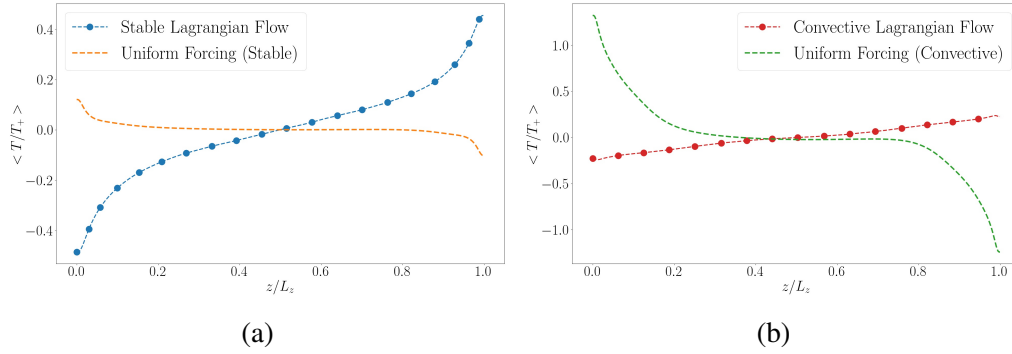


Figure 6.7: (a) The normalised temperature profile for a stable Lagrangian flow (blue) compared with the measured temperature profile of a flow with an imposed profile of thermal forcing. (b) The normalised temperature profile for a convective Lagrangian flow (red) compared with the measured temperature profile of a flow with an imposed profile of thermal forcing

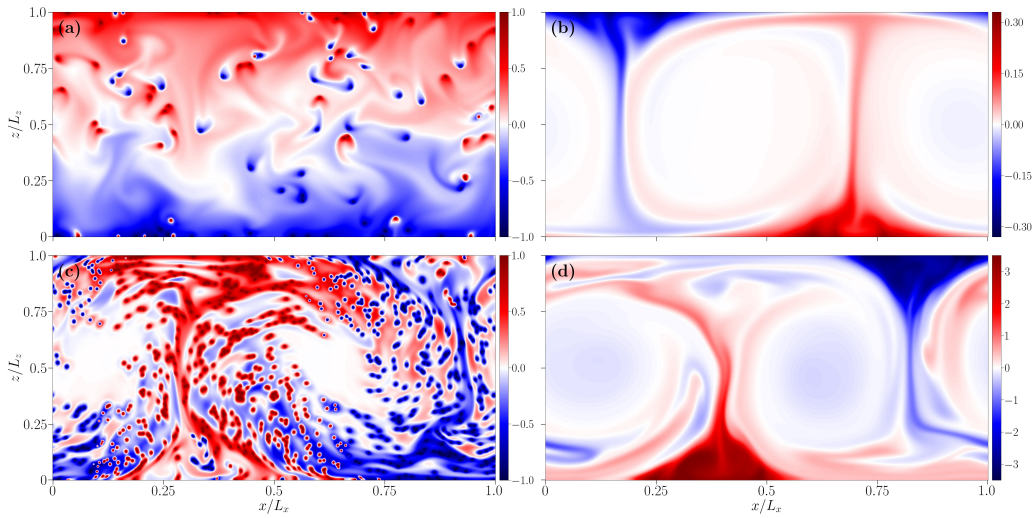


Figure 6.8: Snapshots of the temperature fields (a) a Stable Lagrangian flow, (c) a Convective Lagrangian flow and the two uniformly forced flows to mimic the (b) stable and (d) convective flows. The temperature fields T are divided by the respective T_+ .

Figure 6.6. Defining $Q(z)$, the numerator of the Nusselt number, as the average net heat transfer in the positive z direction at height z given by

$$Q(z) = \left\langle v(\mathbf{r}, t)T(\mathbf{r}, t) - \kappa \frac{\partial T}{\partial z} \Big|_{(\mathbf{r}, t)} \right\rangle_{x, t}, \quad (6.31)$$

where $\langle \cdot \rangle_{x, t}$ indicates the time and spatial averages at a given height z , notice that averaging equation (1.6) over time gives

$$\Phi(z) = \frac{\partial Q}{\partial z}(z) \quad (6.32)$$

The comparison is made for two flows, one Stable flow and one Convective flow. Given identical vertical profiles of thermal forcing (see Figure 6.6), one would expect that the resulting temperature profile and hence the nature of the flows would remain identical. However, as shown in Figure 6.7, the temperature profiles show a dramatic difference, with the Eulerian flows showing an unstable temperature profile similar to the Rayleigh-Bénard Convection. Further, as shown in Figure 6.8, even when the thermal forcing matches the measured value from a Stable configuration, the Eulerian flow with uniform thermal forcing shows a Convective behaviour with clear, well-defined hot and cold plumes and an unstable temperature gradient. Even in the Convective case, the corresponding Eulerian flow is convective. Thus, the presence of the stable temperature gradients, the two clear end-state configurations with very different characteristics with a sharp transition already outlined previously in the text is not merely a result of the net thermal forcing applied on the system but is the result of the particular Lagrangian nature of the virtual thermal tracer particles and the two-way coupling with the fluid. In the uniformly forced case, there never develops Stable configuration so to speak.

6.6.5 Anomalous behaviour for small T_+

We have already noted in previous sections there is weak dependence of the transition of the system on the value of T_+ . In particular, it was observed that for larger T_+ , the transition occurs at a larger N_p and the Stable configurations for larger T_+ have relatively flatter temperature gradients. One would conclude then that for any given N_p , there exists a T_+ small enough such that the system is Convective. However, at very small T_+ , the behaviour of the system begins to diverge from the Stable-Convective binary and attains a third end-state, a Columnar end-state where the temperature profile is still stable ($\partial_z T > 0$) and the system has a weak convective flow with two pairs of counter-rotating vortices and the associated plumes (see snapshot in Figure 6.9(b)). In Figure 6.9(a), we plot the fraction

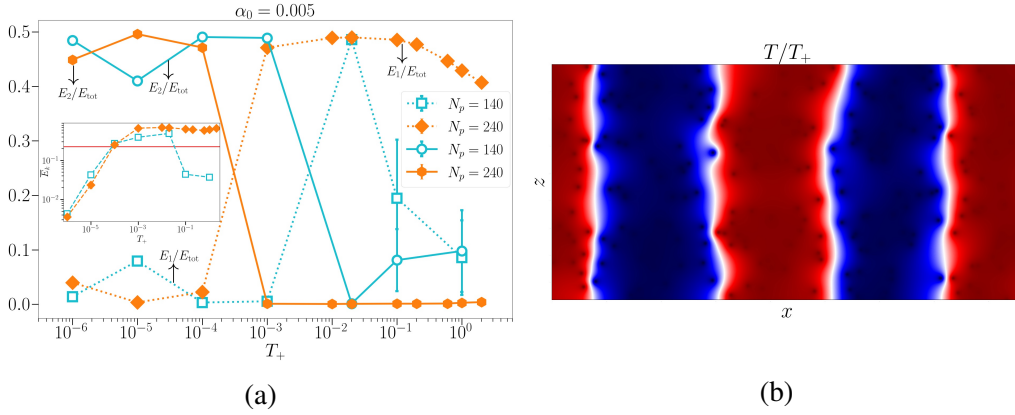


Figure 6.9: (a) The ratio of kinetic energy contained in the first Fourier mode E_1/E_{tot} (solid lines) and E_2/E_{tot} (dashed lines) to the total energy contained in all modes for $N_p = 140$ and $N_p = 240$ plotted against T_+ . Inset shows the averaged normalised TKE \bar{E}_k for the same parameters and the horizontal line represents $\bar{E}_k = E_k^0$. (b) A snapshot of the temperature field for a Columnar flow with $N_p = 240$ and $T_+ = 10^{-5}$.

of energy contained in the first Fourier mode (E_1/E_{tot}) as well as the second Fourier mode (E_2/E_{tot}) to understand the large-scale behaviour of the flow. We can see clearly that for smaller T_+ , the second mode dominates the kinetic energy while the energy contained in the first mode approaches 0. This is the case until a transition T_+ where now the flow turns Convective from Columnar. At larger T_+ for $N_p = 240$ (orange, filled symbols), we see that while E_2/E_{tot} remains small, the value of E_1/E_{tot} shows a decreasing trend. This is because as T_+ is increased, the flow also becomes more turbulent and thus along with the large-scale circulation, smaller scale features begin to appear, thus increasing the energy contained at higher modes as is characteristic of a turbulent flow. For $N_p = 140$ (cyan, empty symbols), the flow is Columnar for $T_+ \lesssim 10^{-3}$ and transitions to convective for $T_+ \sim 0.02$, as evidenced by the values of E_1/E_{tot} and E_2/E_{tot} . However, on increasing T_+ further, the flow again moves to a Stable configuration. This is due to the effect already observed, that for increasing T_+ , the N_p of transition from Stable to Convective is greater. We also see that the Stable configuration is characterised by $E_1 \sim E_2$.

The inset of panel (a) shows the normalised TKE plotted for the two given N_p and varying T_+ . Notice that at small T_+ , when the flow is Columnar, it is characterised by a smaller normalised TKE and kinetic energy smoothly approaches 0 as $T_+ \rightarrow 0$.

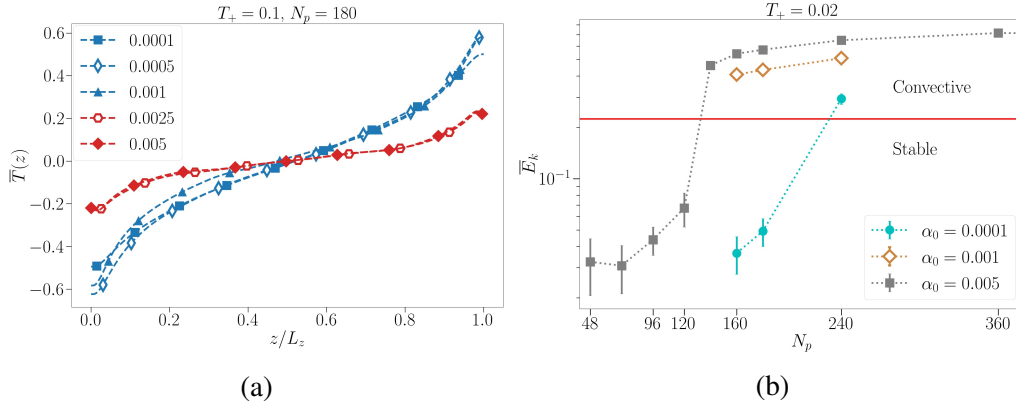


Figure 6.10: (a) Normalised vertical temperature profiles for $T_+ = 0.01$, $N_p = 180$ for different α . The red curves correspond to Convective flows while the blue curves represent the stable flows. (b) Normalised TKE for $T_+ = 0.02$ plotted against N_p for 3 values of α_0 . Horizontal red line represents $E_k^0 = 0.225$.

6.6.6 Effects of varying α_0 and c

It is clear from the above results that an increase in the number of particles N_p strongly pushes the system towards the Convective configuration while increasing T_+ weakly causes the system to tend towards stability. The other ways a phase change from a Stable configuration to a Convective configuration can be triggered is by increasing the fluid-particle coupling strength α_0 or the size of the particle c .

The former effect can be gauged in Figure 6.10. In panel (a), we see the behaviour of the temperature profile for varying α_0 . It has already been seen that the Stable regime is characterised by a strongly stable temperature profile while the Convective regime is characterised by a weakly stable temperature gradient. The temperature profile remains nearly identical for changing values of α_0 except when the flow changes from Stable (blue curves) to Convective (red curves). We also note that the time taken for the flow to relax from the initial unstable configuration (see equation (6.17)) to the eventual stationary state is larger for smaller α_0 . It indicates that for a given temperature scale T_+ and N_p , there exists a temperature difference $\overline{\Delta T}$ for which the flow is stable independent of α_0 . Panel (b) of the same figure where we plot the average normalised TKE \bar{E}_k shows the transition from Stable to Convective for 3 different α_0 . That the increase in TKE corresponds to the transition from Stable to Convective was verified from visualisations of the flow field as well as the strength of the large-scale circulation as already discussed in Section 6.6.2. We see that decreasing α_0 increases the N_p of the transition and still note that the empirical value of E_k^0 for the transition holds.

Increasing c too shows a similar effect, as clear in Figure 6.11 where keeping

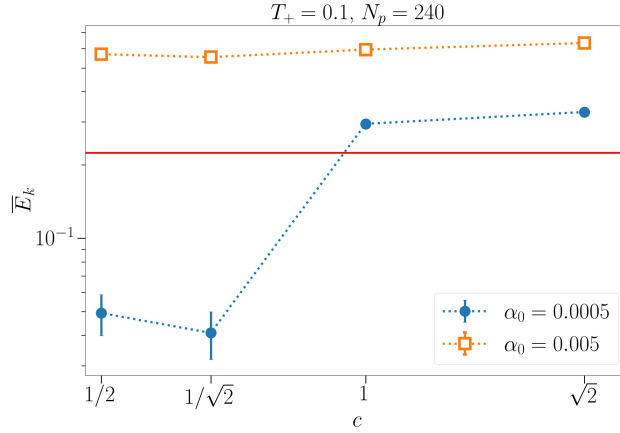


Figure 6.11: Normalised TKE for varying virtual particle size c for two different α_0 .

the other parameters fixed, a transition to Convective configuration is triggered by enlarging the size of the individual virtual particle.

6.7 Conclusions and Discussion

In this study we have performed numerical simulations of an idealized non-isothermal 2D fluid system under the Boussinesq approximation with suspended virtual tracer particles. The particles act as heat sources or sinks depending on the vertical velocity of the tracer via a relaxation term with time-scale $1/\alpha_0$. The particles are coupled to the fluid only thermally and the effect of particles following this specific protocol and the stationary end-state this leads to is studied. Individually, each particle carries heat away from the bottom of the domain towards the top of the domain, thus working to create a thermally more stable system. However, under certain conditions, the cumulative effect of the particles overpowers the tendency towards stability and the result is a system with a large-scale convective flow pattern with increased turbulent kinetic energy, larger heat transfer across the domain, maximum energy in the largest Fourier modes and a weakly stable vertical temperature gradient compared to the more quiescent Stable state. The main parameters of the system are the temperature of the hot, rising particles T_+ , the number of particles N_p , the strength of the thermal coupling between the fluid phase and the particles α_0 and the size of the particle c . Increasing N_p , c and α_0 makes the increasingly convective while increasing weakly T_+ contributes to making the flow more stable.

This Lagrangian protocol is compared with a system with a uniform thermal forcing identical to the measured Lagrangian forcing and it is found that the tem-

perature profiles of the Eulerian system is unstable rather than stable and a convective flow develops even when the forcing is chosen to be identical to a Stable Lagrangian flow for which a convective flow does not develop. Thus, it is the unique non-linear coupling between the particle trajectory and the temperature that leads to the Stable end-state configuration in the Lagrangian case. Further, the behaviour at small T_+ is also explored, where it is found that for very small T_+ , the temperature gradients are too weak to produce a turbulent convective flow and instead a weakly convective flow is seen with characterised by a low turbulent kinetic energy.

The novel temperature protocol chosen for the particle was novel - at first glance while it seems that the particle exclusively aids the formation of convective plumes by enhancing any updrafts that might exist, the protocol also meant that heat is transferred in the positive z direction while the downward moving particles and upward moving particles necessarily balance out each other on average to maintain a neutral temperature for the domain. While the model system might not be exactly physically realisable, it certainly lends a first insight into analogous systems where upward moving particles tend to be hotter and vice-versa. A real-world example would be a cloud droplet moving along with an updraft - the droplet remains uniformly hotter than the surroundings due to condensation of water onto its surface and similarly, falling cloud droplets constantly lose water to the atmosphere thus remaining cooler while moving downward.

The study also opens several further interesting avenues for investigation including but not limited to the formulation of similar simple protocols where the properties of the suspended particles depend on the instantaneous dynamics of the particle itself to attain theoretical or even experimental control and modulation of fluid flows. Further, the study can be extended to include inertial point particles which do not immediately respond to the local fluid velocity as opposed to tracers. Further, the numerical experiments can be performed while taking into consideration the force applied by the particle phase on the fluid, which leads to attenuation of the kinetic energy and can have interesting implications on any large scale convection, if such a convection develops.

Chapter 7

Physics Informed Neural Networks

Summary The chapter contains a brief introduction to Neural Networks, its main components and the main method to train a neural network using data. Next, Physics Informed Neural Networks (PINN) are introduced as a method to solve partial differential equations and recent studies which have successfully used this technique are mentioned. The chapter ends with an outlook on the use of PINNs to tackle problems described earlier in the thesis.

7.1 Introduction

Data assimilation in the form of nudging of the temperature field applied to Rayleigh-Bénard convection has proved to be successful in reconstructing the velocity field for low Rayleigh number flows. However, this data-driven method fared poorly in higher Rayleigh number flows where the degree of turbulence is significant and the small-scale fluctuations of the velocity field are much harder to reconstruct, even given exact data on the temperature everywhere. Mounting experimental and numerical data suggests that Charney's conjecture remains unrealistic and reconstructing missing state variables is an extremely hard, perhaps insurmountable problem.

However, recently a new data driven technique based on neural networks has shown to be successful in inferring velocity and pressure fields of thermal flows with remarkable accuracy given limited data on temperature fields for certain simple flows. In this thesis, we give a brief introduction and account of this technique, using *Physics informed neural networks*.

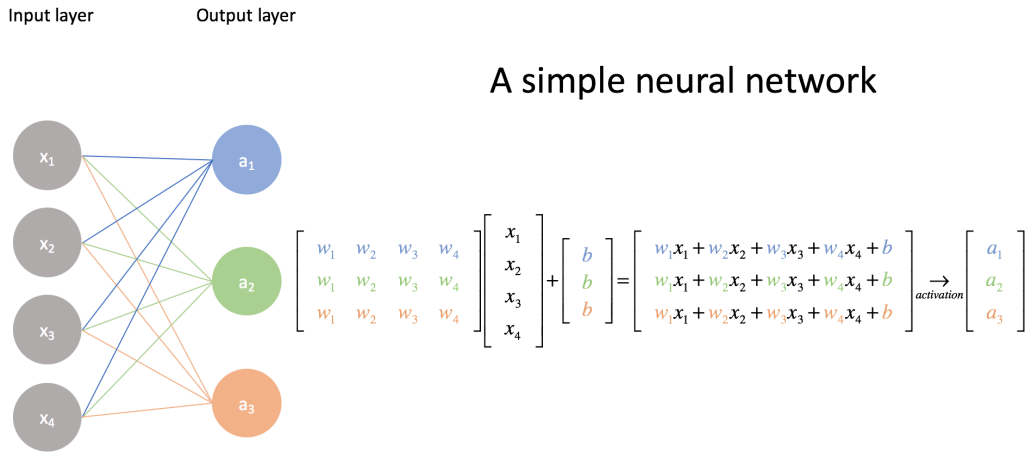


Figure 7.1: The basic structure of a neural network. Image taken from <https://www.jeremyjordan.me/intro-to-neural-networks/>.

7.2 Basics of Neural Networks

An *artificial neural network*, or simply a neural network, is a connected graph of nodes and edges where each node is known as a *neuron* and has a value. Their design is inspired by biological neurons and the neurons are arranged in consecutive layers. The other components of neural networks are the *weights* associated with the edges, while each neural is also associated with a value known as a *bias*. Another crucial component of a neural network is an *activation function*.

The most basic function performed by a neural network is a series of matrix multiplications. For a given set of n neurons $x_1, x_2 \dots x_n$ in a given layer and m neurons $y_1, y_2, \dots y_m$ in a subsequent layer, each node x_i is connected to the m neurons of the next layer by edges with weights $w_{i,1}, w_{i,2} \dots w_{i,m}$. Associated with each of the neurons y_i is a bias b_i , with the value of the layer of neurons $\mathbf{y} = (y_1, y_2, \dots y_m)$ given by

$$\begin{bmatrix} y_1 \\ \vdots \\ \vdots \\ y_n \end{bmatrix} = A \left(\begin{bmatrix} w_{1,1} & w_{1,2} & \dots & w_{1,n} \\ w_{2,1} & w_{2,2} & \dots & w_{2,n} \\ \vdots & \vdots & \ddots & \vdots \\ w_{m,1} & w_{m,2} & \dots & w_{m,n} \end{bmatrix} \begin{bmatrix} x_1 \\ \vdots \\ \vdots \\ x_n \end{bmatrix} + \begin{bmatrix} b_1 \\ \vdots \\ \vdots \\ b_n \end{bmatrix} \right) \quad (7.1)$$

where A is the activation function. In short, for each neuron from a given layer, a set of weights and biases are applied followed by the activation function, while

the output of this operation forms the input for the succeeding layer of the neural network, until the final layer of the network. Neural networks are often made up of several such layers of neurons, each with their associated sets of weights and biases. The first layer of neurons of the entire neural network is known as the input layer. The neural network thus acts as a function of these input variables, with the outputs being the values of the final layer of neurons. The layers of neurons apart from the output and the input layer are often known as *hidden layers* and neural networks with such hidden layers are often called deep neural networks. The matrix multiplication is a purely linear operation - any non-linearity in the resulting neural network function is thus a result of the activation function which acts on the output of the matrix multiplication.

7.2.1 Training a neural network

We have thus far presented the simplest structure of a neural network. Neural networks often include other features such as convolutions, recurrence loops, etc., which perform specialised functions. However, the aim here is to provide only a fundamental introduction to the method of using neural networks.

The most important step of using neural network (NN) based methods is the training step. Given a set of data on some (output) dependent variables as a function of independent (input) variables, the main aim of NN based methods is to *train* the NN using this available data to predict the output from data-sets in the future. This is achieved via a *training* process. Let us consider first the case of a single dependent variable, easily generalisable to the case of finite number of dependent variables. Let the variable y depend on a set of independent variables $\mathbf{x} = (x_1, x_2, \dots, x_3)$ as $y = y(\mathbf{x})$. And let us assume to have measurements of y at several points $y_i = y(\mathbf{x}_i)$. Firstly the network is initialised with some appropriately chosen (usually random) weights and biases. With these weights and biases, \mathbf{x}_i is used as the input to the neural network to generate output z_i . A loss function \mathcal{L} is then constructed as

$$\mathcal{L} = \sum_i \mathcal{L}(y_i, z_i). \quad (7.2)$$

The loss function is the quantity that is sought to be minimised by the training process. Thus, it must represent the deviations of the neural network output from the available data and quantify the error. The loss function must be unbiased and represent the entire data set as well. An example of such a function is simply the L2-norm of the error $|y_i - z_i|^2$.

Once an appropriate loss function has been defined, the next step is the minimisation of this loss, so the neural network represents the data more accurately.

This is achieved via the process of gradient descent, which makes use of the fact that a function decreases fastest in the direction of its negative gradient.

Consider a neural network with k layers, where the j -th layer has n_j elements $a_{1,j}, a_{2,j}, \dots, a_{n_j,j}$ and with weights $w_{a,b}^{(j)}$ going from element a of the j -th layer to element b of the $j + 1$ -th layer. The first layer is the input layer while the k -th layer is the output layer. Thus, each weight $w_{a,b}^{(j)}$ is updated numerically according to the formula

$$w_{a,b}^{(j)} = w_{a,b}^{(j)} - \gamma \frac{d\mathcal{L}}{dw_{a,b}^{(j)}} \quad (7.3)$$

where the derivative of the loss function with respect to the individual weights is calculated according to the chain-rule via a *backward propagation*. γ here is the learning rate and is usually kept fixed. For example, the derivative of the loss with respect to the weights associated with the neurons of the output layer is straightforward to calculate as

$$\frac{d\mathcal{L}}{dw_{a,b}^{(k-1)}}.$$

The term $\frac{d\mathcal{L}}{dw_{a,b}^{(k-2)}}$ is then calculated as

$$\frac{d\mathcal{L}}{dw_{a,b}^{(k-2)}} = \frac{d\mathcal{L}}{dw_{a,b}^{(k-1)}} \frac{dw_{a,b}^{(k-1)}}{dw_{a,b}^{(k-2)}} \quad (7.4)$$

and so on until the derivative of the loss function is calculated with respect to each weight. The derivatives of the loss function are rarely calculated with respect to every single available data point. Instead, certain optimisations are made. The gradient is instead calculated with respect to a *batch* of data. Other methods include *stochastic gradient descent* and *mini-batch gradient descent*.

Thus, the neural network is trained on the data by the optimisation of the weights to minimise the loss function, making the neural network predict the outputs of the input data more and more accurately with respect to the available data over multiple iterations. The data is usually split into a *training set* and a *test set*, wherein the training steps are performed multiple times over the training data set. It is important to ensure that the neural network actually learns the structure of the data and the dependence of the variables on each other rather than merely minimising the loss function by *overcorrection*, where the loss function is minimised very effectively but performs poorly with new data points that the neural network has not been trained on. To ensure that this isn't occurring, the network is not trained on the test set and the loss function is calculated with respect to the

test set at regular intervals in a *validation* step. This is a crucial step and is used as a measure of the neural network’s predictive power.

7.3 Physics Informed Neural Networks

While a neural network is effective at predicting and learning from data, this does not make use of other known details of the data, in particular the constraints of the equations of motion or other dynamical equations of the system being studied do not play a role in the training of the neural network. This is similar to the motivation behind data assimilation techniques.

If the dynamical equations of a system for which data is available is known, given by

$$u_t + \mathcal{N}[u; \lambda] = 0 \tag{7.5}$$

where \mathcal{N} is a general, non-linear operator while λ is the set of known parameters of the system, the loss function is modified to take the equation into consideration. Defining the residual on the equation f as

$$f := u_t + \mathcal{N}[u; \lambda], \tag{7.6}$$

the loss function is modified as

$$\mathcal{L} = \mathcal{L}_{NN} + \mathcal{L}_f \tag{7.7}$$

where the first term \mathcal{L}_{NN} is the usual neural network loss function on the known data while \mathcal{L}_f is the residual of the equation at other appropriately chosen points, known as *collocation points* which are chosen to enforce the dynamical equations. For example,

$$\mathcal{L}_f = \frac{1}{n} \sum_{i=1}^n |f(t_u, x_u)|^2 \tag{7.8}$$

where (t_u, x_u) are the form of the n collocation points. This was first suggested in 1992, [77] and has recently made a comeback. A key innovation that ensures the ease of implementation of this method is the technique of *automatic differentiation* to calculate partial derivatives of the residual with respect to the input variables, similar to the backward propagation employed to calculate the derivative with respect to the weights during gradient descent in the training steps of neural networks. It is defined as a “*Family of techniques that compute derivatives through accumulation of values during code execution to generate numerical derivative evaluations rather than derivative expressions*” [25].

7.4 Applications of PINNs

Physics Informed Neural Networks have recently found application across different types of systems. In [25], PINNs were used to obtain solutions of multiple simple PDE systems, including the 1D-Schrodinger equation with given boundary conditions, the Allen-Cahn equation and even the backward problem of the two-dimensional Navier-Stokes equations wherein given boundary conditions and extremely sparse bulk data, the neural network correctly predicted the parameters of the system. Further, the neural network was also able to reconstruct the pressure field despite not having any pressure data.

Often, velocity measurements are hard to obtain. It is far easier to obtain measurements and visualisation on an advected scalar, such as dyes or biological agents, which are injected or present in the fluid. In another study by Raissi et. al. [26], the ability of physics informed neural networks to learn the hidden states of the system, ie., the scalar velocity of the fluid when only data on the scalar is provided, was shown for several simple systems.

Thus, these neural networks have shown the potential to be a powerful tool to solve PDEs, which could save huge computational resources in the future. Further, the possibility of reconstructing hidden state variables, which has been a recurring theme across this thesis, is also of huge consequence. However, whether such a system can resolve the small scales of a highly turbulent flow given sparse data or further, reconstruct a fluid flow given data on not a passive scalar but an active scalar, is an open topic for future research. As part of this thesis, efforts are also underway to explore some of these possibilities. In particular, whether the nudging experiment using solely temperature measurements can be repeated using PINNs and whether they would be more or less successful than nudging for similar quantities of data and for flows with similar degrees of turbulence. This work is being conducted in collaboration again with Dr. Patricio Clark Di Leoni and Prof. Luca Biferale.

Chapter 8

Conclusions and Discussion

Turbulent thermal flows are an area of active research with several open questions left unanswered and various avenues to explore. Several of the complexities are intrinsic to turbulent fluid flows themselves. The large number of degrees of freedom present in turbulent flows make their temporal and spatial behaviour highly unpredictable. This makes accurately reconstructing or effectively modulating turbulent flows very hard to achieve. When the temperature field is present as an active scalar, it leads to multiple other possible directions of investigation, chiefly regarding the precise role of the temperature field in driving the flow, the correlation between the temperature field and the velocity field and the importance of not only the overall heat input into the system but the precise structure of the input mechanism. In the course of work relating to this thesis, several topics relevant to turbulent thermal flows have been explored in varying detail. The basic features of turbulent fluid flows was understood along with the widely accepted hypotheses of universal similarity of turbulent flows first proposed by Kolmogorov in 1941 regarding the nature of the scaling and small-scale structure of turbulent flows.

The focus in this thesis is on the Rayleigh-Bénard convection, a model thermal flow widely used to study several dynamical features of naturally occurring thermal flows and having an important place in the study of thermal instabilities. The first study detailed in the thesis, on the reconstruction of turbulent Rayleigh-Bénard convection should be seen in context of the difficulty of predicting and reconstructing turbulent flows and the several uncertainties regarding the role played by the temperature field in a turbulent thermal flow. The study adds to the understanding of the way the temperature field drives the velocity field. The flows reconstructed via the technique of nudging are flows which have either very similar or identical temperature fields to the respective reference flows - measuring how much the reconstructed velocity field then varies from the reference velocity fields, both in a global sense and a scale-by-scale sense, helps to clearly and independently ascertain to what degree the dynamics of the velocity field is set

by the temperature field and further, establishes how well correlated the velocity and temperature fields are to each other for varying degrees of turbulence. This investigation also serves to understand the feasibility of the nudging technique for the reconstruction of thermal flows.

Apart from a fundamental knowledge of fluid dynamics and turbulent flows, the study also required an understanding of the fundamentals of data assimilation to understand the context in which nudging arises as a tool for continuous data assimilation and to identify potential applications to other systems, mostly atmospheric flows and problems involving weather forecasting where the use of observational data in conjunction with models is widespread. The study described in this thesis can be considered a first step to understand the feasibility of applying data assimilation techniques using temperature data alone. The Rayleigh-Bénard convection is an ideal testing ground for later application to atmospheric flows given the several dynamic similarities between the two.

Numerically, the chief novelty of the nudging study involved the use of the thermal forcing term for the Lagrangian nudging case, where the application of this heat source-term was done along the trajectory of tracer particles. While this did not involve the creation of any new algorithms, it was the application of an existing algorithm to a problem for the first time, to the best of the author's knowledge. It could be said that the addition of the heat source-term is the common thread that runs throughout the research work conducted as part of this thesis.

While nudging was performed by adding such a heat-source term, where the temperature relaxes to the measured probe temperatures from the reference flow, in the second study, involving the virtual tracer particles, the heat source term forces the temperature to relax towards the particle temperature, with the complete freedom to choose this particle temperature. It can even be said that both studies involve the modulation and modification of a thermal turbulent flow - the first aimed to drive the flow towards a pre-defined flow (the reference flow), thus indirectly setting the source term. In the second study, there is no pre-defined goal towards which the flow must be driven. Thus, it was an investigation into the effects of choosing different forms of this heat source term.

Eventually, the findings reported were for a form of particle temperature which depends on the particle velocity. It is the natural tendency for heat to be transported in the upward direction in the presence of gravity, leading to a stable temperature gradient. Thus, the continuation of the upward heat transport requires continuous injection of heat near the bottom of the fluid to maintain the unstable condition and the upward heat transport continues in the form of the convective flow that is set up. We have seen that when the upward moving particles are set to a hot temperature, this condition is satisfied only beyond a threshold N_p , failing which it is the stable temperature gradient that sets the dynamics of the system. Crucially, we have seen that this dynamic does not depend merely on the

net heat injection at each height. The same on-average injection of heat can lead to extremely different systems, where the uniform, Eulerian approach leads to a convective configuration with an unstable temperature gradient, ie., a more classically convective flow, the Lagrangian approach followed in this study produces a stable temperature gradient and distinct end-states, one quiescent and stable, the other turbulent and convective. This is a unique insight into the redistribution and mixing of heat and temperature stratification, with two flows having identical profiles of thermal forcing, and thus the same net heat transport, but they have very different temperature profiles.

The idea of conditioning the particle feedback on the flow dynamics or the particle dynamics has several potential applications in trying to design novel turbulent convective flows that can be modified in a predictable manner by a simple set of parameters. Ideas from reinforcement and machine learning could also be applied to these particles so as to drive the flow in a desired way.

Lastly, the potential application of Physics Informed Neural Networks (PINNs) to reconstruct the entire Rayleigh-Bénard convection using temperature data represents a novel and exciting possibility to use a cutting-edge tool to understand if Charney's conjecture, which as yet has found no convincing experimental evidence in support, can be revived. The possibility of being able to predict the exact small-scale structure of a turbulent velocity field given the temperature field represents a sort of final frontier in reconstruction of thermal flows, with potential applications in several domains, most specifically in atmospheric flows.

References

- [1] P. A. Davidson, *Turbulence: an introduction for scientists and engineers*, Oxford university press, 2015.
- [2] U. Frisch, *Turbulence: the legacy of A.N. Kolmogorov*, Cambridge University Press, Cambridge, [Eng.] ; New York, 1995.
- [3] J. Boussinesq, *Theorie analytique de la chaleur vol 2* (paris: Gauthier-villars) (1903).
- [4] H. Bénard, *Les tourbillons cellulaires dans une nappe liquide.-méthodes optiques d'observation et d'enregistrement*, *Journal de Physique Théorique et Appliquée* 10 (1) (1901) 254–266.
- [5] L. Rayleigh, *Lix. on convection currents in a horizontal layer of fluid, when the higher temperature is on the under side*, *The London, Edinburgh, and Dublin Philosophical Magazine and Journal of Science* 32 (192) (1916) 529–546.
- [6] S. Chandrasekhar, *Hydrodynamic and hydromagnetic stability*, Courier Corporation, 2013.
- [7] P. G. Drazin, *Introduction to hydrodynamic stability*, Vol. 32, Cambridge university press, 2002.
- [8] E. S. Ching, *Statistics and scaling in turbulent Rayleigh-Benard convection*, Springer, 2014.
- [9] C. Riesinger, *Scalable scientific computing applications for gpu-accelerated heterogeneous systems*, Ph.D. thesis, Technische Universität München (2017).
- [10] T. Krüger, H. Kusumaatmaja, A. Kuzmin, O. Shardt, G. Silva, E. M. Viggien, *The lattice boltzmann method*, Springer International Publishing 10 (978-3) (2017) 4–15.

- [11] R. A. Anthes, Data assimilation and initialization of hurricane prediction models, *Journal of Atmospheric Sciences* 31 (3) (1974) 702–719.
- [12] E. Kalnay, *Atmospheric modeling, data assimilation and predictability*, Cambridge university press, 2003.
- [13] J. E. Hoke, R. A. Anthes, The initialization of numerical models by a dynamic-initialization technique, *Monthly Weather Review* 104 (12) (1976) 1551–1556. doi:10.1175/1520-0493(1976)104<1551:TIONMB>2.0.CO;2.
- [14] S. Lakshmivarahan, J. M. Lewis, Nudging methods: A critical overview, in: *Data Assimilation for Atmospheric, Oceanic and Hydrologic Applications (Vol. II)*, Springer, Berlin, Heidelberg, 2013, pp. 27–57. doi:10.1007/978-3-642-35088-7_2.
URL https://link.springer.com/chapter/10.1007/978-3-642-35088-7_2
- [15] L. Agasthya, P. Clark Di Leoni, L. Biferale, Reconstructing rayleigh–bénard flows out of temperature-only measurements using nudging, *Physics of Fluids* 34 (1) (2022) 015128. doi:10.1063/5.0079625.
- [16] B. K. W. Lahoz, R. Menard, *Data assimilation*, Springer, 2010.
- [17] F. Bouttier, P. Courtier, *Data assimilation concepts and methods march 1999*, Meteorological training course lecture series. ECMWF 718 (2002) 59.
- [18] K. D. Squires, J. K. Eaton, Preferential concentration of particles by turbulence, *Physics of Fluids A: Fluid Dynamics* 3 (5) (1991) 1169–1178.
- [19] M. Cencini, J. Bec, L. Biferale, G. Boffetta, A. Celani, A. Lanotte, S. Musacchio, F. Toschi, Dynamics and statistics of heavy particles in turbulent flows, *Journal of Turbulence* (7) (2006) N36.
- [20] G. Falkovich, A. Fouxon, M. Stepanov, Acceleration of rain initiation by cloud turbulence, *Nature* 419 (6903) (2002) 151–154.
- [21] J. Bec, H. Homann, S. S. Ray, Gravity-driven enhancement of heavy particle clustering in turbulent flow, *Physical review letters* 112 (18) (2014) 184501.
- [22] M. Carbone, A. D. Bragg, M. Iovieno, Multiscale fluid–particle thermal interaction in isotropic turbulence, *Journal of Fluid Mechanics* 881 (2019) 679–721.

- [23] W. S. McCulloch, W. Pitts, A logical calculus of the ideas immanent in nervous activity, *The bulletin of mathematical biophysics* 5 (4) (1943) 115–133.
- [24] O. I. Abiodun, A. Jantan, A. E. Omolara, K. V. Dada, N. A. Mohamed, H. Arshad, State-of-the-art in artificial neural network applications: A survey, *Heliyon* 4 (11) (2018) e00938.
- [25] M. Raissi, P. Perdikaris, G. E. Karniadakis, Physics-informed neural networks: A deep learning framework for solving forward and inverse problems involving nonlinear partial differential equations, *Journal of Computational Physics* 378 (2019) 686–707.
- [26] M. Raissi, A. Yazdani, G. E. Karniadakis, Hidden fluid mechanics: Learning velocity and pressure fields from flow visualizations, *Science* 367 (6481) (2020) 1026–1030.
- [27] A. Marshak, A. Davis, *3D radiative transfer in cloudy atmospheres*, Springer Science & Business Media, 2005.
- [28] O. Reynolds, Xxix. an experimental investigation of the circumstances which determine whether the motion of water shall be direct or sinuous, and of the law of resistance in parallel channels, *Philosophical Transactions of the Royal society of London (174)* (1883) 935–982.
- [29] L. F. Richardson, *Weather prediction by numerical process*, Cambridge university press, 2007.
- [30] A. N. Kolmogorov, The local structure of turbulence in incompressible viscous fluid for very large reynolds numbers, *Cr Acad. Sci. URSS* 30 (1941) 301–305.
- [31] A. N. Kolmogorov, Dissipation of energy in the locally isotropic turbulence, in: *Dokl. Akad. Nauk SSSR A*, Vol. 32, 1941, pp. 16–18.
- [32] K. R. Sreenivasan, On the universality of the kolmogorov constant, *Physics of Fluids* 7 (11) (1995) 2778–2784.
- [33] L. Landau, E. Lifshitz, *Fluid mechanics*, 1959, *Course of theoretical physics* (1959).
- [34] K. Våge, L. Papritz, L. Håvik, M. A. Spall, G. W. K. Moore, Ocean convection linked to the recent ice edge retreat along east greenland, *Nature communications* 9 (1) (2018) 1–8.

- [35] D. L. Hartmann, L. A. Moy, Q. Fu, Tropical convection and the energy balance at the top of the atmosphere, *Journal of Climate* 14 (24) (2001) 4495–4511.
- [36] M. Kronbichler, T. Heister, W. Bangerth, High accuracy mantle convection simulation through modern numerical methods, *Geophysical Journal International* 191 (1) (2012) 12–29.
- [37] A. Brent, V. R. Voller, K. Reid, Enthalpy-porosity technique for modeling convection-diffusion phase change: application to the melting of a pure metal, *Numerical Heat Transfer, Part A Applications* 13 (3) (1988) 297–318.
- [38] A. C. Newell, T. Passot, J. Lega, Order parameter equations for patterns, *Annual review of fluid mechanics* 25 (1) (1993) 399–453.
- [39] G. Ahlers, S. Grossmann, D. Lohse, Heat transfer and large scale dynamics in turbulent rayleigh-bénard convection, *Rev. Mod. Phys.* 81 (2009) 503–537.
- [40] a. X. Chavanne, F. Chilla, B. Castaing, B. Hebral, B. Chabaud, J. Chaussy, Observation of the ultimate regime in rayleigh-bénard convection, *Physical review letters* 79 (19) (1997) 3648.
- [41] X. Zhu, V. Mathai, R. J. Stevens, R. Verzicco, D. Lohse, Transition to the ultimate regime in two-dimensional rayleigh-bénard convection, *Physical review letters* 120 (14) (2018) 144502.
- [42] B. I. Shraiman, E. D. Siggia, Heat transport in high-rayleigh-number convection, *Physical Review A* 42 (6) (1990) 3650.
- [43] E. D. Siggia, High rayleigh number convection, *Annual review of fluid mechanics* 26 (1) (1994) 137–168.
- [44] A. Obukhov, Temperature field structure in a turbulent flow, *Izv. Acad. Nauk SSSR Ser. Geog. Geofiz* 13 (1949) 58–69.
- [45] S. Corrsin, On the spectrum of isotropic temperature fluctuations in an isotropic turbulence, *Journal of Applied Physics* 22 (4) (1951) 469–473.
- [46] R. Bolgiano Jr, Turbulent spectra in a stably stratified atmosphere, *Journal of Geophysical Research* 64 (12) (1959) 2226–2229.
- [47] A. Obukhov, Effect of archimedean forces on the structure of the temperature field in a turbulent flow, in: *Dokl. Akad. Nauk SSSR*, Vol. 125, 1959, pp. 1246–1248.

- [48] D. Lohse, K.-Q. Xia, Small-scale properties of turbulent rayleigh-bénard convection, *Annual Review of Fluid Mechanics* 42 (2010) 335–364.
- [49] T. I. Gombosi, A. Gombosi, *Gaskinetic theory*, no. 9, Cambridge University Press, 1994.
- [50] X. Shan, X.-F. Yuan, H. Chen, Kinetic theory representation of hydrodynamics: a way beyond the navier–stokes equation, *Journal of Fluid Mechanics* 550 (2006) 413–441.
- [51] H. Grad, Note on n-dimensional hermite polynomials, *Communications on Pure and Applied Mathematics* 2 (4) (1949) 325–330.
- [52] P. J. Dellar, Bulk and shear viscosities in lattice boltzmann equations, *Physical Review E* 64 (3) (2001) 031203.
- [53] Z. Guo, C. Zheng, B. Shi, Discrete lattice effects on the forcing term in the lattice boltzmann method, *Phys. Rev. E* 65 (2002) 046308.
- [54] D. Wolf-Gladrow, A lattice boltzmann equation for diffusion, *Journal of statistical physics* 79 (5) (1995) 1023–1032.
- [55] T. Seta, Implicit temperature-correction-based immersed-boundary thermal lattice boltzmann method for the simulation of natural convection, *Phys. Rev. E* 87 (2013) 063304.
- [56] G. P. Cressman, An operational objective analysis system, *Monthly Weather Review* 87 (10) (1959) 367–374.
- [57] A. Azouani, E. Olson, E. S. Titi, Continuous data assimilation using general interpolant observables, *Journal of Nonlinear Science* 24 (2) (2014) 277–304.
- [58] J. Charney, M. Halem, R. Jastrow, Use of incomplete historical data to infer the present state of the atmosphere, *J. Atmos. Sci.* 26 (1969) 1160–1163.
- [59] A. Farhat, E. Lunasin, E. S. Titi, Continuous Data Assimilation for a 2D Bénard Convection System through Horizontal Velocity Measurements Alone, *Journal of Nonlinear Science* 27 (3) (2017) 1065–1087, arXiv: 1602.00042. doi:10.1007/s00332-017-9360-y.
URL <http://arxiv.org/abs/1602.00042>
- [60] A. Farhat, H. Johnston, M. Jolly, E. S. Titi, Assimilation of Nearly Turbulent Rayleigh–Bénard Flow Through Vorticity or Local Circulation Measurements: A Computational Study, *Journal of Scientific Computing* 77 (3)

- (2018) 1519–1533. doi:10.1007/s10915-018-0686-x.
 URL <https://doi.org/10.1007/s10915-018-0686-x>
- [61] M. Ghil, B. Shkoller, V. Yangarber, A Balanced Diagnostic System Compatible with a Barotropic Prognostic Model, *Monthly Weather Review* 105 (10) (1977) 1223–1238, publisher: American Meteorological Society Section: *Monthly Weather Review*. doi: 10.1175/1520-0493(1977)105<1223:ABDSCW>2.0.CO;2.
 URL https://journals.ametsoc.org/view/journals/mwre/105/10/1520-0493_1977_105_1223_abdscw_2_0_co_2.xml
- [62] M. Ghil, M. Halem, R. Atlas, Time-Continuous Assimilation of Remote-Sounding Data and Its Effect on Weather Forecasting, *Monthly Weather Review* 107 (2) (1979) 140–171, publisher: American Meteorological Society Section: *Monthly Weather Review*. doi: 10.1175/1520-0493(1979)107<0140:TCAORS>2.0.CO;2.
 URL https://journals.ametsoc.org/view/journals/mwre/107/2/1520-0493_1979_107_0140_tcaors_2_0_co_2.xml
- [63] C. C. Lalescu, C. Meneveau, G. L. Eyink, Synchronization of chaos in fully developed turbulence, *Physical Review Letters* 110 (8) (2013) 084102. doi:10.1103/PhysRevLett.110.084102.
- [64] P. Clark Di Leoni, A. Mazzino, L. Biferale, Synchronization to Big Data: Nudging the Navier-Stokes Equations for Data Assimilation of Turbulent Flows, *Physical Review X* 10 (1) (2020) 011023, publisher: American Physical Society. doi:10.1103/PhysRevX.10.011023.
 URL <https://link.aps.org/doi/10.1103/PhysRevX.10.011023>
- [65] H.-D. Xi, Y.-B. Zhang, J.-T. Hao, K.-Q. Xia, Higher-order flow modes in turbulent rayleigh-bénard convection, *Journal of Fluid Mechanics* 805 (2016) 31–51.
- [66] P. Clark Di Leoni, A. Mazzino, L. Biferale, Synchronization to big data: Nudging the navier-stokes equations for data assimilation of turbulent flows, *Phys. Rev. X* 10 (2020) 011023. doi:10.1103/PhysRevX.10.011023.
 URL <https://link.aps.org/doi/10.1103/PhysRevX.10.011023>

- [67] M. R. Maxey, J. J. Riley, Equation of motion for a small rigid sphere in a nonuniform flow, *The Physics of Fluids* 26 (4) (1983) 883–889.
- [68] T. Elperin, N. Kleorin, I. Rogachevskii, Turbulent thermal diffusion of small inertial particles, *Physical review letters* 76 (2) (1996) 224.
- [69] D. Bercovici, G. Schubert, G. A. Glatzmaier, Three-dimensional spherical models of convection in the earth’s mantle, *Science* 244 (4907) (1989) 950–955.
- [70] D. Tritton, Internally heated convection in the atmosphere of venus and in the laboratory, *Nature* 257 (5522) (1975) 110–112.
- [71] H. Kim, D. A. Boysen, J. M. Newhouse, B. L. Spatocco, B. Chung, P. J. Burke, D. J. Bradwell, K. Jiang, A. A. Tomaszowska, K. Wang, et al., Liquid metal batteries: past, present, and future, *Chemical reviews* 113 (3) (2013) 2075–2099.
- [72] Q. Wang, D. Lohse, O. Shishkina, Scaling in internally heated convection: a unifying theory, *Geophysical Research Letters* 48 (4) (2021) e2020GL091198.
- [73] H. J. Park, K. O’Keefe, D. H. Richter, Rayleigh-bénard turbulence modified by two-way coupled inertial, nonisothermal particles, *Physical Review Fluids* 3 (3) (2018) 034307.
- [74] R. Zamansky, F. Coletti, M. Massot, A. Mani, Radiation induces turbulence in particle-laden fluids, *Physics of Fluids* 26 (7) (2014) 071701.
- [75] R. Zamansky, F. Coletti, M. Massot, A. Mani, Turbulent thermal convection driven by heated inertial particles, *Journal of Fluid Mechanics* 809 (2016) 390–437.
- [76] Q. Wang, D. Lohse, O. Shishkina, Scaling in internally heated convection: a unifying theory, *Geophysical Research Letters* 48 (4) (2021) e2020GL091198.
- [77] D. C. Psychogios, L. H. Ungar, A hybrid neural network-first principles approach to process modeling, *AIChE Journal* 38 (10) (1992) 1499–1511.